

# **Three-dimensional structure of the glycine-betaine transporter BetP by cryo electron crystallography**

Dissertation

Zur Erlangung des Doktorgrades der Naturwissenschaften

vorgelegt beim Fachbereich Biochemie, Chemie und Pharmazie  
der Johann Wolfgang Goethe Universität in Frankfurt am Main

von

**Ching-Ju Tsai**

aus Taipei, Taiwan

Frankfurt am Main 2008

---

Die Arbeit wurde in der Abteilung Structurbiologie des Max-Planck-Instituts für Biophysik in Frankfurt am Main durchgeführt und vom Fachbereich Biochemie, Chemie und Pharmazie der Johann Wolfgang Goethe Universität als Dissertation angenommen

Dekan:

1. Gutachter: Prof. Dr. Bernd Ludwig
2. Gutachter: Prof. Dr. Werner Kühlbrandt

Datum der Disputation: 08. Dezember, 2008

---

---

# Table of Contents

<b>Abstract</b> .....	<b>6</b>
<b>Zusammenfassung</b> .....	<b>9</b>
<b>Abbreviations</b> .....	<b>14</b>
<b>1. Introduction</b> .....	<b>16</b>
1.1. Membrane permeability .....	16
1.2. Osmotic adaptation in bacteria .....	17
1.2.1. The glycine-betaine transporter BetP .....	19
1.2.2. Interaction between BetP and lipids .....	23
1.3. Structure determination of membrane proteins .....	25
1.3.1. Electron microscopy and electron crystallography .....	27
1.3.2. 2D crystallization .....	29
1.3.3. Data collection and processing .....	34
1.4. Overview of this thesis .....	34
<b>2. Materials and Methods</b> .....	<b>36</b>
2.1. Protein expression and membrane preparation .....	36
2.1.1. Materials and reagents .....	36
2.1.2. Plasmid preparation and transformation .....	36
2.1.3. Culture growth and protein expression .....	37
2.1.4. Membrane preparation .....	37
2.2. Protein purification and quality analysis .....	37
2.2.1. Materials and reagents .....	37
2.2.2. Membrane solubilization .....	38
2.2.3. Protein purification .....	38
2.2.4. SDS polyacrylamide gel electrophoresis .....	38
2.2.5. Western blotting .....	39
2.3. <i>C. glutamicum</i> lipid preparation .....	39
2.3.1. Material .....	39
2.3.2. Culture growth .....	40
2.3.3. Lipid preparation, extraction, and lipid polarization .....	40
2.3.4. Lipid analysis .....	41
2.4. 2D Crystallization .....	42
2.4.1. Materials and reagents .....	42
2.4.2. Incubation .....	42
2.4.3. Detergent removal .....	43
2.5. Electron microscopy .....	43



---

2.5.1.	Data collection of negatively stained samples .....	43
2.5.2.	Cryo data collection .....	44
2.6.	Data Processing .....	45
2.6.1.	Single image processing .....	45
2.6.2.	Tilt geometry refinement.....	46
2.6.3.	Handedness determination.....	46
2.6.4.	Data merging.....	47
2.6.5.	3D map reconstruction .....	47
2.6.6.	Non-crystallographic symmetry of the 3D map .....	48
<b>3.</b>	<b>Results .....</b>	<b>49</b>
3.1.	Characterization of BetPΔC45 .....	49
3.2.	2D Crystallization .....	49
3.2.1.	Detergents, lipids, and temperature .....	49
3.2.2.	Dialysis conditions.....	51
3.3.	2D crystals of BetPΔC45 in <i>E. coli</i> lipids and bovine CL .....	55
3.3.1.	Projection structure from a negatively stained crystal.....	55
3.3.2.	Mirror-symmetric projection structure .....	56
3.3.3.	Deconvolution by expanding the unit cell.....	58
3.3.4.	A very rare case: p22 <sub>1</sub> 2 <sub>1</sub> crystals.....	61
3.4.	2D crystals of BetPΔC45 in <i>C. glutamicum</i> lipids.....	65
3.4.1.	Projection structure of sheet-like crystals.....	66
3.4.2.	Projection structure of tubular crystals.....	68
3.5.	Projection structure of BetPΔC45 in PG 16:0-18:1.....	70
3.6.	Lipid analysis by TLC and mass spectrometry.....	72
3.6.1.	Preliminary analysis by thin-layer chromatography.....	73
3.6.2.	Mass Spectrometric analysis by multiple precursor ion scanning.....	75
3.7.	3D map and NCS averaging.....	79
3.7.1.	Data collection of tilted crystals.....	79
3.7.2.	Handedness determination.....	81
3.7.3.	3D data merging .....	82
3.7.4.	3D map.....	88
<b>4.</b>	<b>Discussion .....</b>	<b>99</b>
4.1.	Evaluation of protein sample quality .....	99
4.2.	2D crystallization .....	100
4.2.1.	Optimization of crystallization conditions.....	100
4.2.2.	Tubular 2D crystals .....	101
4.2.3.	Morphology and resolution .....	102

---

4.3.	Role of different lipids in crystallization .....	102
4.3.1.	Pseudo crystals in <i>E. coli</i> lipids/bovine CL mixture .....	102
4.3.2.	Well-ordered crystals in PG 16:0-18:1 and in <i>C. glutamicum</i> lipids .....	105
4.4.	BetP $\Delta$ C45 and lipids .....	106
4.4.1.	Role of lipids in BetP $\Delta$ C45 crystallization .....	106
4.4.2.	Role of cardiolipin in osmoadaptation .....	108
4.4.3.	Chill activation in 2D crystallization .....	108
4.4.4.	Functional lipids for crystallization .....	109
4.5.	3D structure of BetP $\Delta$ C45 .....	110
4.5.1.	Comparison of BetP $\Delta$ C45 and BetP wild type .....	110
4.5.2.	Asymmetric trimer of BetP $\Delta$ C45 .....	112
4.5.3.	Tentative identification of the cytoplasmic membrane surface .....	114
4.5.4.	Different monomer conformations .....	116
4.5.5.	Oligomeric state and transport function of BetP .....	119
4.6.	Prospects .....	121
4.6.1.	Interaction between BetP and the substrate .....	121
4.6.2.	Function of the N-terminus .....	122
<b>5.</b>	<b>Appendix .....</b>	<b>123</b>
5.1.	Appendix I: Native gel and molecular weight .....	123
5.2.	Appendix II: Merging statistics .....	124
5.3.	Appendix III: The 3D map without modifying the amplitude .....	126
5.4.	Appendix IV: Density maps of monomer 3 with different B factors and $\sigma$ cut-offs applied .....	127
5.5.	Appendix V: projection structure of BetP WT .....	128
5.6.	Appendix VI: Projection maps of BetP WT and BetP $\Delta$ C45 .....	129
<b>6.</b>	<b>References .....</b>	<b>130</b>
<b>7.</b>	<b>Acknowledgement .....</b>	<b>135</b>
<b>8.</b>	<b>Curriculum Vitae .....</b>	<b>139</b>

---

## Abstract

Membranes are known to have low permeability for most ions and hydrophilic molecules. Universally, cells are equipped with transport proteins to exchange these materials which may play a vital role in maintaining cellular function. For example, compatible solutes are often up-taken when soil bacteria encounter hyperosmotic stress; this process prevents bacteria from dehydration via balancing the osmotic strength in and outside the cell. Compatible solutes are neutral, small molecules which can be accumulated up molar range without disrupting cellular metabolism.

The soil bacterium *Corynebacterium glutamicum* has five secondary transporters for compatible solutes, of which four are directly regulated by the osmotic strength across the membrane. The transporter, BetP, performs a high affinity uptake of glycine-betain when encountering hyperosmotic stress. BetP belongs to the betaine/carnitine/choline/transporter (BCCT) family, and is predicted to have twelve transmembrane helices with both termini facing the cytoplasm. The goal of this thesis is to facilitate understanding of BetP function by determining a three dimensional (3D) model of its structure.

Two-dimensional (2D) crystallization of wild-type (WT) BetP has been successfully performed by reconstitution into a mixture of *E. coli* lipids and bovine cardiolipin, and it gave ~ 5  $\mu\text{m}$  wide vesicular crystals which diffract to 7.5  $\text{\AA}$  resolution (Ziegler, Morbach et al. 2004). Diffraction patterns of these crystals however showed unfocused spots, generally due to high mosaicity. Better results were obtained by using the constitutively active mutant BetP $\Delta$ C45 in which the first 45 amino acids of the positively charged C-terminus were removed. BetP $\Delta$ C45 crystals obtained under the same conditions for BetP WT were concluded to be pseudo crystals, based on the inconsistency of symmetry. These crystals had BetP $\Delta$ C45 molecules randomly up/downwards inserted into membrane crystals, and cannot be used for structure determination, even though they diffracted up to 7  $\text{\AA}$ .

The problem of pseudo crystal formation could be solved by changing the lipids used for 2D crystallization to a native lipid extract from *C.*

---

*glutamicum* cells. This change of lipids improved the crystals to well-ordered packing with exclusive p12<sub>1</sub>\_b symmetry. To understand the role of lipids in crystal packing and order, lipids were extracted at different stages during crystallization, and identified by using multiple precursor ion scanning mass spectrometry. The results show that phosphatidyl glycerol (PG) 16:0-18:1 is the most dominant lipid species in *C. glutamicum* membranes, and that BetP has a preference for the fatty acid moieties 16:0-18:1. Crystallization with synthetic PG 16:0-18:1 proved that an excess of this lipid prevents pseudo crystal formation, but these crystals did not reach the quality as previously achieved by using the *C. glutamicum* lipids.

Apart from the effect of lipids in crystallinity, the concentration and type of salts influenced crystal growth and morphology. High salt conditions (>400 mM LiCl or KCl) yielded tubular crystals, whereas low salt conditions (<300 mM LiCl, NaCl or KCl) led to formation of up to 10  $\mu$ m large sheet-like crystals. The intermediate concentration gave a mixture of sheet-like and tubular crystals. In terms of resolution, sheets diffracted better than tubes. The sheet-like crystals used for 3D map reconstruction were obtained from a dialysis buffer containing 200 mM NaCl combined with using *C. glutamicum* lipids.

Electron microscopic images were taken from frozen-hydrated crystals using a helium-cooled JEOL 300 SFF microscope or a liquid nitrogen-cooled FEI Tecnai G<sup>2</sup> microscope at 300 kV, which allowed optimal data collection and minimized radiation damage to the sample. More than 1000 images of tilt angles up to 50° were taken and evaluated using optical diffraction of a laser beam. The best 200 images were processed with the MRC image processing software package, and 79 images from different tilt angles were merged to the final data set used for calculation of a 3D map at a planar resolution of 8 Å.

The structure shows BetP $\Delta$ C45 as a trimer with each monomer consisting of 12 transmembrane  $\alpha$ -helices. Protein termini and loop regions could not be determined due to the limited resolution of the map. Six of the twelve helices line a central cavity forming a potential substrate-binding

---

chamber. Each monomer shows a central cavity in different sizes and shapes. Thus, the constitutively active BetP $\Delta$ C45 thus forms an unusual asymmetric homotrimer. BetP most likely reflects three different conformational states of secondary transporters: the cytoplasmically open (C), the occluded (O), and the periplasmically open (P) states. The C and O states are similar to BetP WT projection structure, while the P state is discrepant and highly flexible due to the shape and size of the central cavity as well as the lowest intensity of the density. The observation of the P state corresponds well to the constitutively active property of BetP $\Delta$ C45. For the high resolution structure of the C and O states are available, this work presents the first structural information of the P state of a secondary transporter.

---

## Zusammenfassung

Eine Grundeigenschaft aller biologischen Lipidmembranen ist ihre niedrige Permeabilität für Ionen und andere hydrophile Moleküle, wie Zucker, Aminosäuren oder DNA. Dies ist überlebenswichtig für alle Zellen, da diese sich so gegen die Umgebung abzugrenzen und eigene Reaktionsräume schaffen können. Für Wasser hingegen sind Zellmembranen durchlässig, weshalb es zur spontanen Osmose kommt wenn unterschiedliche Salzkonzentrationen auf beiden Seiten der Membran vorliegen. In diesem Falle dringt Wasser von der Seite mit niedrigerer Salzkonzentration (hypotonisch) zu der mit höherer Salzkonzentration (hypertonisch), bis ein thermodynamisches Gleichgewicht erreicht ist. Eine innerhalb der Zelle erhöhte Salzkonzentration führt zu einem Anschwellen der Zelle, ist sie außerhalb erhöht, wird der Zelle Wasser entzogen. In beiden Fällen unterliegt die Zelle einem osmotischen Stress, der die zellulären, fein aufeinander abgestimmten biochemischen Reaktionen empfindlich stören kann.

Osmotischer Stress ist ein häufig auftretendes Problem, ist aber besonders relevant für Zellen welche direkt der Umgebung ausgesetzt sind. Bodenbakterien z.B. sind häufig starken Schwankungen der Osmolarität ausgesetzt wenn es in Folge von Überflutungen oder Dürren zu einer Änderung der Salzkonzentrationen und Wasseraktivität in ihrer Umgebung kommt. Zum Ausgleich akkumulieren die Bakterien kompatible Solute, welche die Osmolarität zwischen Umgebung und Zelle ausgleichen und gleichzeitig eine stabilisierende Wirkung auf Enzyme und andere Proteine ausüben. Der In- und Export der kompatiblen Solute geschieht mittels membrangebundenen sekundären Transportern, die vorhandene Konzentrationsgradienten über die Plasmamembran als Energiequelle nutzen. In dem Bodenbakterium *Corynebacterium glutamicum* wurden fünf Transporter für unterschiedliche kompatible Solute beschrieben, von denen vier osmotisch reguliert sind.

Das Thema dieser Arbeit sind die Struktur/Funktionsprinzipien des osmoaktiven Betaintransporters BetP aus *Corynebacterium glutamicum*, der das kompatible Solut Betain unter Ausnutzung eines Natriumgradienten in

---

die Zelle importiert. Gleichzeitig dient BetP auch als Osmolaritäts und Temperatursensor der die Menge an importierten Betain ohne Umwege anpassen kann. BetP gehört zur Proteinfamilie der Betain/Carnitine/Cholin Transporter (BCCT), einer Klasse von Transportern mit 12, auf Basis von Hydrophobizitätsplots der Aminosäuresequenz vorhergesagten Transmembranhelices. Ziel dieser Arbeit war es die dreidimensionale (3D) Struktur von BetP mittels Elektronenkristallographie zu bestimmen, um damit ein besseres Verständnis sowohl von osmoregulatorischen Sekundärtransportern, als auch der BCCT Proteinfamilie zu ermöglichen.

Grundvoraussetzung für eine elektronenkristallographische Strukturauflösung ist eine Anordnung des Proteins in zweidimensional (2D) geordneten Kristallen. Die 2D Kristallisation findet durch Rekonstitution von detergenzsolubilisierten und mittels Affinitäts-Chromatographie aufgereinigtem Protein in Lipide statt. Die Rekonstitution des Proteins in Lipide ist ein Vorteil der Elektronenkristallographie gegenüber anderen Methoden der Strukturaufklärung wie der Röntgenkristallographie, da die Proteine während der Kristallisation wieder aus der potentiell denaturierenden Detergenz- in eine der natürlichen Membran ähnliche Lipidumgebung überführt werden. Dies gilt insbesondere da assoziierte Lipide häufig von besonderer Bedeutung für die Funktion von Membranproteinen sind und Strukturänderungen durch die verwendeten Detergenzien ausgeschlossen werden können. Häufig erlaubt es die Membranamgebung und die nur zweidimensionalen Kristallkontakte auch Strukturänderungen des Proteins direkt im Kristall herbeizuführen und mittels Elektronenkristallographie aufzulösen, wie z.B. bei der Strukturaufklärung des Meta I Zustands des Photorezeptors Rhodopsin oder den pH induzierten Strukturänderungen des Natrium/Protonen Antiporters von *Methanococcus jannaschii*.

Zur Kristallisation wurden der BetP Wildtyp und eine konstitutiv aktive Mutante mit einem um 45 Aminosäuren gekürzten C-Terminus (BetP $\Delta$ C45) in *E. coli* überexprimiert und mittels Streptavidin-Affinitätschromatographie aufgereinigt. Die C-terminal gekürzte Mutante wurde gewählt, da Aktivitätsmessungen eine weitaus geringere Osmosensitivität dieser Mutante

---

zeigten. Des Weiteren ist sie konstitutiv aktiv und transportiert Betain weitestgehend unabhängig von der Osmolarität der Umgebung über die Membran, wodurch sie hervorragend geeignet ist den aktiven Zustand von BetP strukturell zu charakterisieren.

Sowohl der BetP Wildtyp als auch die BetP $\Delta$ C45 Mutante konnten kristallisiert werden und von beiden wurden Projektionsdichtekarten berechnet und miteinander verglichen. Die Entfernung des positiv geladenen C-Terminus in der BetP $\Delta$ C45 Mutante hatte einen starken Effekt auf die Kristallisierung und führte reproduzierbar zur Bildung von besser geordneten Kristallen mit niedrigerer Mosaizität. Die BetP $\Delta$ C45 Mutante wurde daher für die weitere Optimierung und die 3D Strukturaufklärung verwendet.

Neben dem Protein, sind die verwendeten Lipide für die Bildung von geordneten 2D Kristallen von entscheidender Bedeutung. Während der Optimierung der Kristallisationsbedingungen wurde BetP $\Delta$ C45 mittels dreier verschiedener Lipidpreparationen kristallisiert: (i) einer 3:2 (w/w) Mischung aus *E. coli* polaren Lipiden und Rinderherz Cardiolipin, (ii) einem *C. glutamicum* Lipidextrakt und (iii) synthetischen Phosphatidylglycerol (PG) 16:0-18:1.

Zum besseren Verständnis und zur besseren Kontrolle des Lipideinflusses auf das Kristallisationsverhalten wurden Lipidextrakte aus verschiedenen Stadien der Kristallisation hergestellt und die enthaltenen Lipide mittels quantitativer Massenspektrometrie (quantitative multiple-precursor ion scanning mass spectrometry) bestimmt. Die Ergebnisse zeigen die Präferenz von BetP für 16:0-18:1 Fettsäurereste und das eine an diesen Resten reiche Lipidmischung die Bildung von Pseudokristallen verhindert. Verwendung von reinem PG 16:0-18:1 führte jedoch nur zur Bildung von kleinen nicht für die 3D Strukturaufklärung geeigneten Vesikeln mit einem Ordnungsgrad um 12 Å.

Die besten Ergebnisse wurden mit dem *C. glutamicum* Lipidextrakt erzielt. Die mit dieser Lipidmischung geformten Kristalle hatten die Form von großflächig kristallin geordneten Platten, die besonders für die Aufnahme von



---

3D Daten geeignet sind. Wichtiger noch als die vorteilhafte Größe war der höhere Ordnungsgrad, welcher die Datenaufnahme bis zu einer Auflösung von 7-8 Å erlaubte und damit die Identifizierung von Transmembranhelices, den grundsätzlichen Strukturbauusteine von Membranproteinen ermöglicht. Die Kenntnis der Lage und Anordnung der Transmembranhelices ist eine wichtige Voraussetzung für das Verständnis der Funktion eines Proteins und eine wertvolle Referenz für die Faltung des Proteins in einer der Zellmembran ähnlichen Lipidumgebung.

Zur Bestimmung der 3D Struktur von BetP $\Delta$ C45 wurden elektronenkristallographische Aufnahmen von mehr als 200 Kristallen aufgenommen und die zur Strukturaufklärung nötigen Phasen und Amplituden mittels Bildbearbeitung extrahiert. Die 3D Information wurde aus zwischen 0 und 50 Grad gekippten Aufnahmen der 2D Kristalle gewonnen. Alle Daten wurden unter Einhaltung der p12<sub>1</sub>\_b Symmetrie zu einem einheitlichen Datensatz vereinigt, der mit einem mittlerem Phasenresidual von 20.4° eine hohe Qualität aufzeigt. Amplituden und Phasen dieses Datensatzes wurden für die Errechnung einer 3D Dichtekarte des Kristalls verwendet.

Die bestimmte Dichte hat eine planare Auflösung von 8 Å und zeigt BetP als Trimer mit 12 länglichen Dichten pro Monomer, welche den 12 mittels Hydrophobizitätsplot vorhergesagten Transmembranhelices zugeordnet wurden. Interessanterweise ist die Anordnung dieser Dichten unterschiedlich für alle drei Monomere, wie eindeutig mittels Analyse einer Kreuzkorrelations-Dichtekarte zwischen den Monomeren und anhand der möglichen Kristallsymmetrien gezeigt werden konnte. Die Unterschiede dieses äußerst ungewöhnlichen asymmetrischen Homotrimers konzentrieren sich um einen von vier Helices umrahmten Hohlraum mit unterschiedlich großen Eintrittsöffnungen für jedes Monomer. Basierend auf der Anordnung des BetP asymmetrischen Homotrimers und bekannten biochemischen Daten wurde ein Modell erstellt in dem sich die Substratbindungsstellen in dem zentralen Hohlraum befindet und in dem jedes Monomer des asymmetrischen Homotrimers einen unterschiedlichen Aktivierungszustand einnimmt. Die drei Aktivierungszustände wurden als die cytoplasmatisch

---

offene (C), die geschlossene (O) und periplastisch offene (P) Konformation von sekundären Transportern interpretiert. Monomer C zeigt die stärkste Dichte und hat daher die wahrscheinlich höchste Stabilität, gefolgt von Monomer O und Monomer P. Neben der geringsten Dichte zeigt Monomer P auch die größte Abweichung zur Projektionskarte des inaktiven BetP Wildtypes auf, was als weiterer Hinweis für die Zuordnung der einzelnen Konformationen verwendet wurde. Für die C und O Konformationen von Sekundärtransportern sind hochauflösende Röntgenstrukturen bekannt und der Vergleich mit der 3D Struktur von BetP wird interessante Einblicke in deren Funktion ermöglichen. Die vorliegende Arbeit liefert damit die ersten Strukturinformationen für die P Konformation eines Sekundärtransporters und legt damit einen Grundstein für das bessere Verständnis dieser für alle Zellen überlebenswichtigen Klasse von Transportern.

# Abbreviations

2D	Two-dimensional
3D	Three-dimensional
AHT	Anhydrotetracyclin
APC	Amino acids/polyamines/cholines
BCCT	Betaine/carnitine/choline transporter
CL	Cardiolipin
CMC	Critical micelle concentration
CTF	Contrast transfer function
CV	Column volume
DAG	Diacyl glycerol
DDM	Dodecyl maltoside
DM	Decyl maltoside
DPG	Diphosphatidyl glycerol
EM	Electron microscopy
HPLC	High performance liquid chromatography
IQ	IQ 1 indicates a signal more than seven times the background, and IQ 7 indicates a signal equal to background after correction for the background. $IQ = 7 \times [(intensity\ of\ noise) / (intensity\ of\ signal)]$ .
LPR	Lipid-to-protein ration
<i>m/z</i>	Mass over charge
MAD	Multiwavelength anomalous dispersion
MFS	Major facilitator superfamily
MIR	Molecular isomorphous replacement
MPIS	Multiple precursor ion scanning
MPD	2-methyl-2,4-pentanediol
MS	Mass spectrometry
NCS	Non-crystallographic symmetry
NMR	Nuclear magnetic resonance spectroscopy
NSS	Neurotransmitter/sodium symporter
PA	Phosphatidic acid
PC	Phosphatidyl choline
PE	Phosphatidyl ethanolamine
PG	Phosphatidyl glycerol
PI	Phosphatidyl inositol
PIS	Precursor ion spectrum
RT	Room temperature
S/N	Signal-to-noise ration
SAD	Singlewavelength anomalous dispersion
SDS	Sodium dodecylsulfate
SSSS	Sodium/solute symporter superfamily
TLC	Thin-layer chromatography
TM	Transmembrane
WT	Wild-type

---

---

---

# 1. Introduction

## 1.1. Membrane permeability

Membranes are essential for all single living cells. A membrane plays the elemental role of a physical barrier, which disallows most molecules and ions to pass through it. The membrane defines the boundary between cells, and also form compartmentation in the cell, resulting in different organelles such as nucleus, Golgi apparatus, mitochondrion, endoplasmic reticulum, and chloroplast; these cellular compartments are thus allowed to carry out specific functions such as photosynthesis, respiration, protein folding etc.

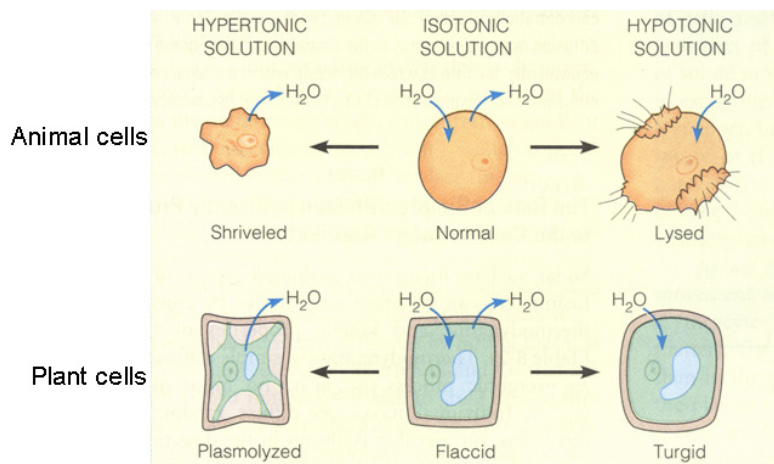
A membrane is formed from phospholipids, which possess a hydrophilic head group and two hydrophobic fatty acid chains. The most common structure of phospholipids in the cell is the bilayer, which has fatty acid chains located in the centre region and head groups exposed to the cytosol or the environment. A physiological lipid bilayer is about 40 Å thick. The protein embedded in the cell membranes control substance exchange. Proteins associated on the membrane surface may locally change the lipid conformation due to the electric charge and/or specific interaction.

Since a membrane separates the cell from its environment, the movement of most substances across a membrane can be understood in terms of transmembrane (TM) concentration gradients, and, for charged solutes, the membrane potential. Transport proteins are essential for exchanging materials, because the membrane is impermeable for most ions such as  $K^+$ ,  $Na^+$  and  $NH_4^+$ , and hydrophilic molecules such as sugars, amino acids and a variety of metabolic intermediates. The cell membrane is however permeable to water molecules, and water movement across a membrane can be described as osmosis. Osmosis occurs spontaneously if the osmolality (or salt concentration) is different on either side of the membrane. Water permeates through the membrane from the hypotonic side to the hypertonic side in order to reach a thermodynamic equilibrium.

---

## 1.2. Osmotic adaptation in bacteria

Osmotic stress is one of the most frequently encountered problems for all kinds of cells. For example, soil bacteria and plants often face dramatic fluctuation of environmental osmolarity due to changes in surrounding solute concentration and water activity caused by floods and droughts. Due to these changes, transmembrane water fluxes take place spontaneously. It further changes the cell volume which can lead to cell death, especially for animal cells which do not have a cell wall (Figure 1). Many cellular properties are changed due to the osmotic stress, such as the cell volume, the turgor pressure membrane strain, the concentration of individual solutes, ionic strength, and crowding of macromolecules. Bacteria have been forced to develop efficient osmotic adaptation against sudden environmental changes. Osmosensors are proteins which directly or indirectly detect the osmotic pressure ( $\Pi$ ). A direct osmosensor would detect water activity, while indirect osmosensors detect the change of cellular properties.



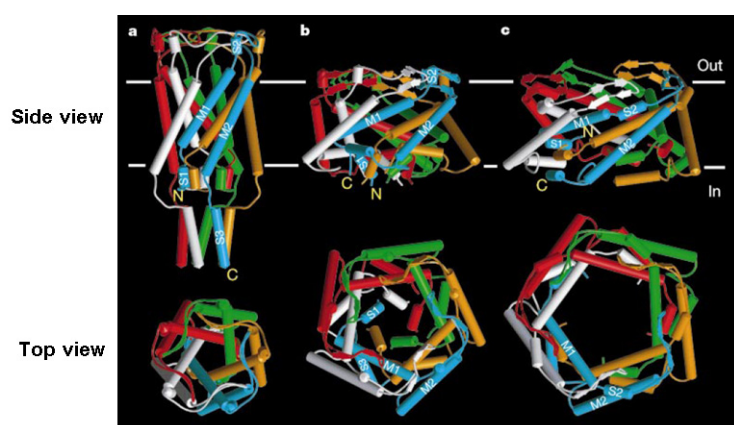
**Figure 1. Response of animal and plant cells to osmotic changes.**

Water influx and efflux through a cell membrane is determined by the environment. In hypertonic conditions, cells lose water; it results in shrivelling of an animal cell and plasmolyzation of a plant cell. On the contrary, water influx occurs to the cells in a hypotonic environment. Cells therefore swell, sometimes even burst. Plant cells are protected by the cell wall, so cell swelling only leads to increase of the turgor pressure.

Hypoosmotic stress happens to bacteria upon sudden immersion in water. It has the following effects: the environmental osmolarity drops, water influx through the cytoplasmic membrane occurs, which brings about cell swelling, and dropping of intracellular solute concentration. Under these

---

conditions, cells are over-hydrated, and cell membrane tension rises. The emergent water exporting valves, so-called mechanosensitive channels, are therefore triggered to excrete water (Figure 2). Mechanosensitive channels are indirect osmosensors. Opening and closing of the channels are controlled by the membrane tension. When cell swelling brings the increase of membrane tension, it leads to the opening of the mechanosensitive channels to excrete water. Thus, cell volume decreases and the cellular osmolarity is recovered to normal conditions.



**Figure 2. Proposed closing and opening mechanisms of the mechanosensitive channel, MscL, from *Mycobacterium tuberculosis* (Sukharev, Betanzos et al. 2001).** The functional MscL of *M. tuberculosis* forms a pentameric arrangement of monomers. Each MscL monomer consists of 136 amino acids forming two transmembrane helices (M1, M2), soluble domains (S1, S2, S3) with the N- and C-termini located in the cytoplasm. The opening and closing are controlled by membrane tension. (a) Close-resting conformation; (b) close-expanded conformation; (c) open conformation.

On the other hand, cells use different mechanisms to cope with hyperosmotic stress. In a hyperosmotic environment, bacteria suffer from dehydration, causing an increase of the intracellular solute concentration and a decrease of cell volume. In order to regain water and keep the cell shape, bacteria employ a strategy by accumulating so-called osmoprotectants to increase the cellular osmolarity. In general, the osmoprotectants are compatible solutes, which are highly soluble and carry no net charge at physiological pH. Several molecules have been found to act as osmoprotectants: disaccharides such as trehalose, trimethylammonium compounds such as glycine-betaine (Figure 3C), tetrahydropyrimidine ectoine, and amino acids like proline. Bacteria can accumulate these molecules up to the molar range without disrupting vital cellular metabolism.

---

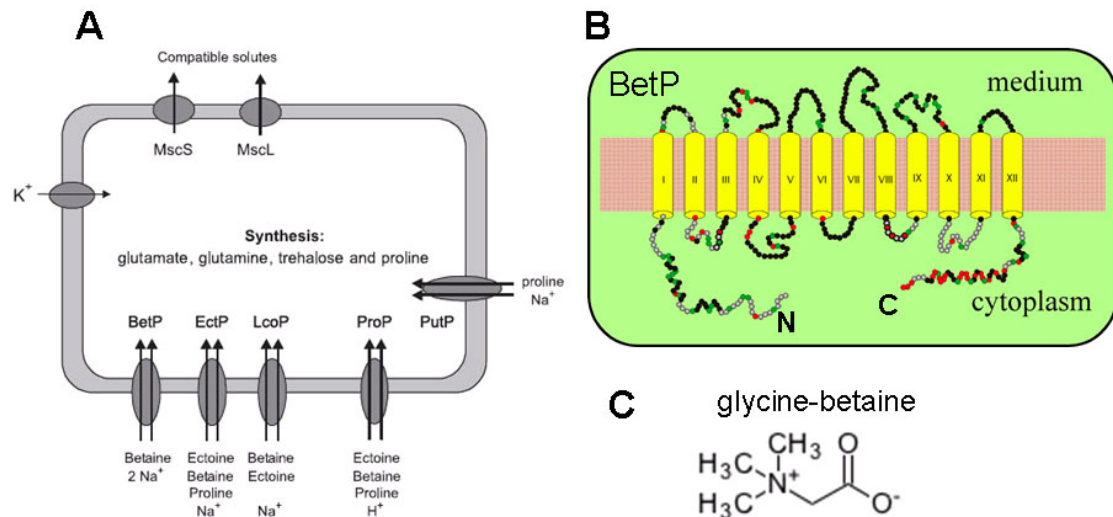
Compatible solutes can be accumulated by transporters importing them from the environment. If this type of molecules is poorly in short supply, then cells regulate solute accumulation by biosynthesis.

Transporters facilitate the movement of molecules passing across the cell membrane for vital needs, such as signal transduction, nutrient supply and toxin elimination. According to the type of driving force, transporters can be divided into two groups: primary and secondary transporters. Primary transporters use a direct energy source, such as ATP, while secondary transporters consume indirect energy, e.g. proton or salt gradients across the cell membrane. Prokaryotic and eukaryotic secondary transporters are further phylogenetically divided into three families: the major facilitator superfamily (MFS), the amino acid/polyamine/choline (APC) family, and the sodium/solute symporter superfamily (SSSS). There is a subfamily belonging in SSSS, named betaine/carnitine/choline transporter (BCCT) family. Their common feature is to transport compatible solutes with a quaternary ammonium group  $[R-N^+(CH_3)_3]$ .

### **1.2.1. The glycine-betaine transporter BetP**

The soil bacterium *Corynebacterium glutamicum* is equipped with five BCCT family transporters: BetP, EctP, LcoP, ProP, and PutP (Figure 3A), and all four of them except PutP are osmoregulated. The glycine-betaine transporter BetP is the best-studied among the five transporters. When reconstituted into proteoliposomes, BetP is activated by an increase of the internal concentration of monovalent cations.  $K^+$ ,  $Rb^+$ , and  $Cs^+$  are found to be more effective in activating BetP than  $Na^+$ ,  $NH_4^+$ , or choline. Therefore BetP is concluded to be a  $K^+$ -specific chemosensor (Rübenhagen, Morbach et al. 2001).





**Figure 3. Transport systems related to osmoregulation in *C. glutamicum*. and topology of BetP**

(A) Four osmoregulated uptake carriers for compatible solutes, namely BetP, EctP, LcoP, and ProP are present in *C. glutamicum*, as well as PutP, which is not osmoregulated. In addition, at least two efflux channels, as well as an osmoregulated  $K^+$  uptake system is found. Apart from uptake, osmotic compensation is also achieved by biosynthesis of compatible solutes.

(Krämer and Morbach 2004)

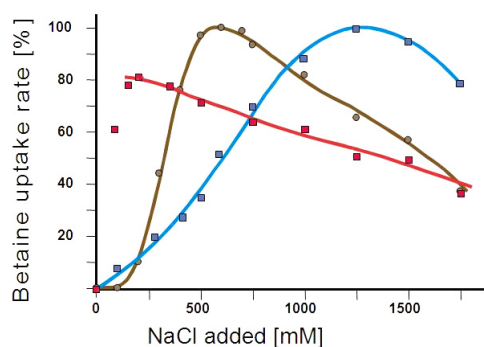
(B) BetP is predicted to have 12 TM helices and two hydrophilic termini facing the cytoplasm. (Peter, Burkovski et al. 1998)

(C) Chemical formula of glycine-betaine, which is a glycine with trimethylation at the ammonium group.

BetP consists of 595 amino acids, which are predicted to arrange into twelve transmembrane helices and two hydrophilic termini with 50-60 amino acids facing the cytoplasm (Figure 3B). The C-terminus is revealed to form an  $\alpha$ -helical structure by CD spectroscopy (Morbach and Krämer 2005). To understand the function of both termini, BetP truncated at either end was studied. The N-terminally truncated BetP is down-regulated, and thereby a higher osmotic pressure is required for activation (Figure 4). A C-terminal truncation (from  $\Delta C23$  to  $\Delta C45$ ) leads to complete deregulation of the protein. These BetP $\Delta C$  variants are permanently active in glycine-betaine uptake and not responsive to osmotic stress. From the amino acid sequencing, the osmoregulator N-terminus carries negative charge. In contrast, the C-terminus however possesses positive charge and interacts with the membrane. The increasing  $K^+$  in cytoplasm activates BetP by altering the conformation of the C-terminus. It further changes the interaction between the C-terminus and the membrane, and probably the conformation of the

---

whole transporter as well.



**Figure 4. Betaine uptake rate of BetP, BetP $\Delta$ N60, and BetP $\Delta$ C23 independent to external NaCl concentration.**

Betaine uptake rate was measured in *C. glutamicum* cell expressing BetP wild-type (brown), BetP $\Delta$ N60 (blue), and BetP $\Delta$ C23 (red) respectively. N-terminal deletion leads BetP to deregulation of osmotic stress, meaning a higher osmolarity is required to activate this mutant. BetP $\Delta$ C23 is not sensitive to osmolarity and transports glycine-betaine at all salt concentration (Peter, Burkovski et al. 1998).

BCCT family members are characterized by a highly conserved region in the transmembrane helix VIII and the following loop (Figure 5) (Farwick, Siewe et al. 1995; Peter, Weil et al. 1998; Morbach and Krämer 2003; Steger, Weinand et al. 2004). The conserved tryptophanes in the helix VIII form the substrate binding pocket. A similar binding pocket is also observed in the periplasmic ligand binding protein ProX from *E. coli*, which shows a density of glycine-betaine localized between three tryptophanes in the X-ray structure (Schiefner, Breed et al. 2004). By comparing the sequences of BetP and other BCCT family members, BetP shows 25 % homology to the carnitine transporter CaiT from *Escherichia coli*, 29 % to EctP, the ectoine/proline/glycine-betaine transporter from *C. glutamicum*, and 37 % homology to LcoP, the ectoine/glycine-betaine transporter (Higgins, Bleasby et al. 1992).

```

BetP      MTTSDPNPKPIVEDAQPEQITATEELAGLLENPTNLEGKLADAEIIIILEGEDTQASLNW
LcoP      MSTNSGNNLPESQESPEEPHYPHDTHPLVPG-----ISVDAQRNKFGLDK
EctP      ----MSSNIAITTEPEGKKNKGLKSDP-----
CaiT      -----MKNEKRKTGIEP-----
          .
          .

BetP      SVIVPALVIVLATVVMVIGFKDSFTNFASSALSAVVDNLGWAFILFGTVFVFFIVVIAAS
LcoP      TVFGVTAALILAFIANGISSPDSVSSVSSTMFSWAMTNFGWLLNFVMLIGIGTMLYIAFS
EctP      FIFSIIVGVFVVIATIALGKARTTFSAIAGWLENLWVMIYIGVSLVFIPLMGI FAS
CaiT      KVEFFPLIIVGILCWLTVRDLDAANVVINAVFSYVTNVGWAFEWYVVMVLFGWFLVFG
          : . . . . . : . . . . . : . . . . . : . . . . . : . . . . .
          : . . . . . : . . . . . : . . . . . : . . . . . : . . . . .

BetP      KFGTIRLGRIDEAPEFRVTSWISMMFAAGMGIGLMFYGTTEPLTFYRN---GVPGHDEH
LcoP      RYGRIKLGTDEDEPEFSRFSWIAMMFGAGIGVGIFFGCPSEPLWHYLSPPPHTVEGSTPE
EctP      RYGRVKLGDDDDPEHTLIWVFCMLFAGVGVAVLMFWGVAEPINHAFNVPMANEESMSEA
CaiT      PYAKKRLG--NEPPEFSTASWIFMMFASCTSAAVLFWG-SIEIYYYISTPPFGLPNSGT
          : . : ** : : * . : * : * . : : * . : : * . : : * . : : * .
          : . : * . : : * . : : * . : : * . : : * . : : * .

BetP      NVGVAMSTMFHWTLHPWAIYAIVGLAIAYSTFRVGRKQLLSS-AFVPLIGEKGAEGLG
LcoP      SLHQALAQSHFWGLSAWGLYALVGGALAYSSYRRGRVTLISS-TFRSLFGEK-TEGIAG
EctP      AIVQAFAYTFYHFGIHMVIMALPGLSLGYFIYKRKLPRLSS-VFSPILG-KHIYSTFG
CaiT      AKELGLAYSLSFWGPELPWATYSFLSVAFAFFVVRKMEVIRPSSSTLVPLVGEKHAKGLFG
          : . . . . . : * . . . . : . . . . . : * . . . . : * . . . .
          : . . . . . : * . . . . : . . . . . : * . . . . : * . . . .

BetP      KLIDILAIATVFGTACSLGLGALQIGAGLSAANIIEDPSDWTIVGIVSVLTLAFIFSAI
LcoP      RLIDMMAIATLFGTAATLGLSAIQVGGVQIISGASEITNNILIAI IAILTIGFIISV
EctP      KLIDVLAIVGTTFGIAVSVGLGVLQINAGMNKLWSTPQVS-WVQLLIIILITAVACISVA
CaiT      TIVLNFYLVALIFAMGTSGLGATPLVTECMQWLFGIP-HTLQLDAI IITCWIILNAICVA
          : * : . . . * . : : * . : : * . : : * . : : * . : : * .
          : * : . . . * . : : * . : : * . : : * . : : * .

BetP      SGVKGKIYLSNANVLAALLAIFVVFVGPVSIINLLPSSIGNYLSNFFQAGRTAMSA
LcoP      SGVSKGIRYLSNLSLTLGLVLFVFTGPTLELLNLIPSSVLEYGSEFLSMAGKSLSWG
EctP      SGLDKGIRKLLSNINIAMAVLMMFFILFTGPTLLLRFLVESFGIYASWMPNLMFWTDSFQ
CaiT      CGLQKGVRIASDVRSYLSFLMLGWVIVSGASFIMNYFTDSVGMMLMYLPRMLFYTDPIA
          . * : * . : * . : : : : : : : : : : : : : : : : : : : :
          : * : * . : * . : : : : : : : : : : : : : : : : : : : :

BetP      DGTAGEWLSWTIFYWAWWISWSPFVGMFLARISGRSIREFILGLVLPAGVSTVWFSI
LcoP      EETI-EFQAGWTAIFYAWWIAWTPFVGMFLARISGRRTLREFALITMAIPSFILILAFIT
EctP      DNPG--WQKWTIFYWAWTICWSPYVGMFLARISGRRTVREFIGGLALPAIFGVVWFSI
CaiT      KGG---FPQGWTFIFYAWWVIYAIQMSIFLARISGRRTVRELCFGMVLGLTASTWILWTV
          . : : * * * * * : : : * * * * * : : : * * * * * : : : * * * * *
          : : : * * * * * : : : * * * * * : : : * * * * * : : : * * * * *

BetP      FGGTAIVFE-QNGESIWDGAAE----EQLFGLLHALPG--GQIMGIAMILGTFFFITS
LcoP      FGGTAITMRENVDGDFGSSSKE----QVLFDMFSNLPL--YSITPFILIFVLAVFFVTS
EctP      FGRAGIEVELSNPGFLTQPTVVEGDVPAALFNVLQEQYPL--TGIVSAFALVIVIFFITS
CaiT      LGSNTLLLIDKNIINI PNLI EQY-VAARIETWAALPLSTATMWGFILCFIATVTLVN
          : * : . . * : : : : : : : : : : : : : : : : : : : :
          : * : . . * : : : : : : : : : : : : : : : : : : : :

BetP      ADSASTVMGTMSQHGQ-LEANKWVTAANGVATAAIGLTLTLLSGGDNALSNLQNVTVI VAT
LcoP      ADSASVVMGTMSQGN-PAPNKLI VVFWGLCMMGI AVVMLLTGGESALTGLQNTILIAI
EctP      IDSAALVNDMFATGAE-NQTPSYRVMNACTIGAVAGSLLIISPSSGIATLQEVVIVIAF
CaiT      ACSYTLAMSTCREVRDGEPPLLVRIGNSILVGIIGIVLLALG---LKPIQTAIAGGC
          * : . . . : . . . : . . . : . . . : . . . : . . . : . . .
          * : . . . : . . . : . . . : . . . : . . . : . . . : . . .

BetP      PFLFVVIGLMPALVKDLSND--VIILEYREQQRFNARL-----ARERR-
LcoP      PFLVLI VMAIFIKDLSTDPAAIRQRYAKAAISNAVVRGLEEHGDDFELSIEPAEEGRG
EctP      PFFLVQFVMMFSLKGMSEDAAAVRRVQTRQWEKTDTPKLEEHSSQPAPGYDDEGNPLF
CaiT      PLFFVNIMVTLSEIKDAKQNWKD-----
          * : : * : : : : : * : . . :
          * : : * : : : : : * : . . :

BetP      -----VHNEHRKRELAAKRRRERKASGAGKRR-----
LcoP      AGATFDSTADHITDWYQRTDE-----EGNDVDYDFTTGKWADGWTPESTE EGEVDAKGD-
EctP      MPALHDEDDGNIVIPGNVIEGDLGVVGDVDDPEEAQEMGSRFKIVEQTRPQSRDEYDI
CaiT      -----

```

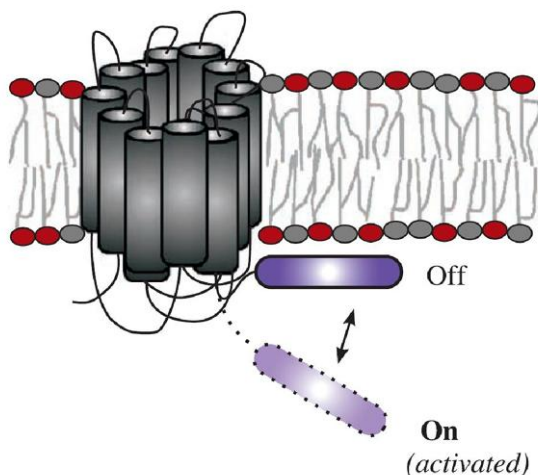
**Figure 5. Sequence alignment of BetP, LcoP, EctP and CaiT.**  
The red boxes represent the predicted transmembrane helices based on the hydrophobicity. (\*) single, fully conserved residue; (:) groups with strong conservation in the chemical features; (.) groups with weak conservation in the chemical features; the chemical features include hydrophobicity, polarity, presence or absence of ionizable groups.

---

### 1.2.2. Interaction between BetP and lipids

How does BetP sense the intracellular osmolarity? How does BetP regulate glycine-betaine uptake from  $K^+$ -sensing? To answer these questions, it is important to understand the relation between BetP and its environment in the lipid bilayer. Based on the reported transport measurements, it is evident that the C-terminus apparently plays a key role in sensing the osmolality. To describe the sensing ability of BetP via the C-terminus, a switch mechanism is therefore proposed in order to elucidate the interaction between the C-terminus, lipids, and the environmental osmolality.

In an osmostress-free condition, the C-terminus of BetP is proposed to attach to the membrane surface because of the charge (negatively charged membrane and positively charged C-terminus). When the cell is dehydrated, the increasing  $K^+$  in the cytosol accelerates the C-terminus of BetP to detach from the cell membrane. This acts as a trigger for BetP to switch from off to on by a conformational change at the C-terminus (Figure 6). This switch mechanism of BetP is regulated by the osmolality and the affinity between the C-terminus and the cell membrane. Due to this switch, BetP regulates the glycine-betaine uptake for the whole cell to adapt to osmotic stress.

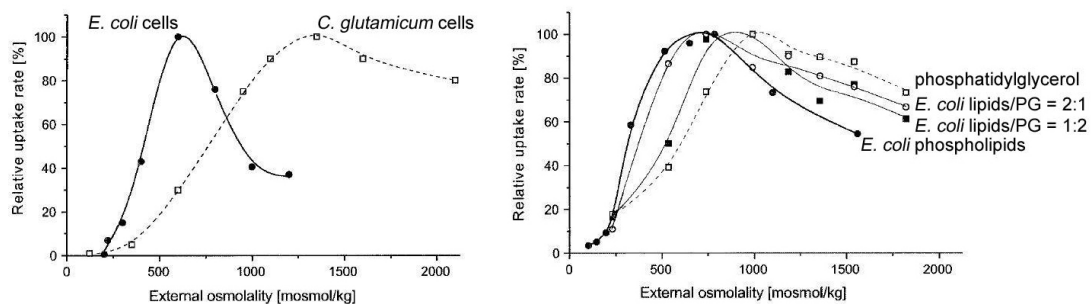


**Figure 6. Proposed switch mechanism of BetP (Poolman, Spitzer et al. 2004).**

The positively charged C-terminus attaches to the membrane surface in the inactive state. When osmotic stress occurs, the increased cellular osmolarity makes the C-terminus detach from the membrane surface. BetP becomes “switched-on” due to the conformational change.

Based on transport mechanism, it looks like that the glycine-betaine uptake rate of BetP depends on the environmental lipid composition. BetP expressed in *C. glutamicum* tolerates higher salt concentrations than that

expressed in *E. coli* (Figure 7, left) (Peter, Burkovski et al. 1996; Rübenhagen, Rönsch et al. 2000). In the *in vitro* systems, BetP reconstituted in the liposomes with different lipid compositions also showed a shift of osmostress in activating BetP (Figure 7, right) (Rübenhagen, Rönsch et al. 2000). Therefore, the composition of the membrane seems to play a major role in activation threshold of BetP.



**Figure 7. Modulation of BetP activity by the lipid composition of intact cells and proteoliposomes (Rübenhagen, Rönsch et al. 2000).**

The osmotic threshold to activate BetP is lipid-dependent.

(Left) In intact cells, BetP needs higher osmotic stress to be fully active in *C. glutamicum* cells than in *E. coli* cells.

(Right) In proteoliposomes prepared with different lipid mixtures, PG facilitates the activation of BetP by higher osmotic stress.

A cell membrane contains different kinds of phospholipids. In *E. coli*, phosphatidyl ethanolamine (PE) is the major lipid class in the cytoplasmic membrane (75 %), followed by phosphatidyl glycerol (PG) (19 %), and cardiolipin (CL, also named diphosphatidyl glycerol (DPG)) (6 %) (Morein, Andersson et al. 1996). However, PG is the main lipid class (87 %) in the cytoplasmic membrane of *C. glutamicum* (Hoischen and Krämer 1990). Lipids from natural sources carry neutral and/or negative charge. Depending on lipid composition, membrane potential varies from organism to organism, which could further influence the activity of proteins associated to or embedded in the membrane.

Due to the charged amino acids, the C-terminus of BetP has stronger attraction with negatively charged PG than with neutrally charged PE. It also explains why *C. glutamicum* needs a higher osmotic stress for BetP in glycine-betaine uptake than *E. coli* and the *in vitro* system shown in Figure 7.

---

### 1.3. Structure determination of membrane proteins

Knowing the structure of a protein is the key to understand how it performs its cellular function. A protein structure gives the spatial location of the atoms, which often describes the catalytic mechanism and the chemical relation to the surroundings. X-ray crystallography, electron microscopy and nuclear magnetic resonance spectroscopy (NMR) have been well-established for protein structure determination. Each method has its own advantages and disadvantages, and the applicability depends on the question addressed and solution behavior of protein.

NMR has been routinely used for small compounds in chemistry. It measures the energy difference between opposite spins in an atom which has an odd sum of neutron and proton, e.g.  $^{13}\text{C}$ ,  $^{14}\text{N}$ , and  $^1\text{H}$ . The energy difference is affected by the spins of neighboring atoms less than 5 Å away, and it plots the relation between atoms in a molecule. Since a protein molecule mainly consists of carbon, nitrogen, oxygen, and hydrogen, it is difficult to assign the spatial correlation of each residue in proteins larger than 20 kDa. The advantage of NMR is that the measurement can be done on a time scale suitable for monitoring dynamics between proteins and substrates. In addition, only a small amount of protein in solution is required for an NMR study; however, high concentration of protein sample (0.1-3 mM) is prerequisite. For membrane proteins, the presence of detergent results in slower tumbling time and hence line broadening. Numerous methods have been developed to overcome this problem and alternatively solid-state NMR can be used (see also **1.3.2.**).

X-ray crystallography was used to solve the very first protein structure (myoglobin). Afterwards it developed into the most widespread method to obtain high resolution information of proteins. The only required sample is a three-dimensional (3D) protein crystal, which is typically grown by the vapor diffusion method. Crystal formation occurs when the protein concentration reaches supersaturation, followed by nucleation. Higher resolution of the crystal can be achieved with better ordered crystals. Principally, X-ray diffraction patterns of a crystal contain the information to determine the



---

coordinates of each ordered atom in the crystal. However, during data collection the information for the phase of each reflection is lost and only the intensity is recorded. This is because no X-ray lens exists and the data collection is not recorded in real space but in Fourier space. Phase information is the most important parameter to determine the structure. Many methods have been developed to regain the phase information, e.g. molecular replacement (MR) from a known homolog structure, multiple isomorphous replacement (MIR) by introducing heavy atoms to calculate the intensity differences between native proteins and protein derivatives with specifically bound heavy atoms, or multi-wavelength anomalous dispersion (MAD) and single-wavelength anomalous dispersion (SAD) for crystals with heavy atoms.

In the past few years, several structures of the secondary transporters with multiple transmembrane helices have been solved by X-ray crystallography (Table 1). These proteins give an overview of the structural frame for transport of ions and/or small molecules. The MFS members, the glycerol-3-phosphate transporter (GlpT) and the lactose permease (LacY), for example, show a high similarity in their structural architecture. On the contrary, the glutamate transporter (Glt<sub>Ph</sub>H7) and the leucine transporter (LeuT<sub>Aa</sub>), both from the neurotransmitter/sodium symporter (NSS) family, are distinct in basic structure and oligomeric state. In general, the TM domain of these transporters is built up of  $\alpha$ -helices with varied tilt angles, but the arrangement of these helices does not follow any specific topology and the oligomeric state is also not decided by the family classification. Therefore, it is difficult to predict the 3D structure of a membrane protein, even though the secondary structure is often well interpreted based on the hydrophobicity of the amino acid sequence. So far, no high-resolution structure of BCCT family has been solved. Several BCCT members have been cloned, expressed, and purified (Peter, Weil et al. 1998). BetP is especially singled out due to its osmoregulated uptake rate and the sensing ability of the osmolality. Meanwhile, the well-established expression and purification of BetP allow massive preparations for structural determination. Moreover, BetP also shows a high stability for detergent-rich conditions and high temperatures. These factors enable BetP a good candidate for structural determination

among the BCCT family members.

<b>Secondary transporter</b>	Glycerol-3-phosphate transporter (GlpT)	Lactose Permease (LacY)	Glutamate transporter (Glt <sub>PH</sub> H7)	Leucine transporter (LeuT <sub>Aa</sub> )	Na <sup>+</sup> /H <sup>+</sup> antiporter (NhaA)	Multidrug efflux transporter (AcrB)
<b>Organism</b>	<i>E. coli</i>	<i>E. coli</i>	<i>P. horikoshii</i>	<i>A. aeolicus</i>	<i>E. coli</i>	<i>E. coli</i>
<b>Family</b>	MFS	MFS	Glutamate transporter Family; NSS Family	NSS Family	Na <sup>+</sup> /H <sup>+</sup> Antiporter (NhaA) Family	Resistant-nodulation-division (RND) Family
<b>Reference</b>	(Huang, Lemieux et al. 2003)	(Abramson, Smirnova et al. 2003)	(Yernool, Boudker et al. 2004)	(Yamashita, Singh et al. 2005)	(Hunte, Screpanti et al. 2005)	(Seeger, Schiefner et al. 2006)
<b>PDB code</b>	1PW4	1PV6	1XFH	2A65	1ZCD	2DHH
<p><b>Table 1. Structures of the secondary transporters with TM 11-13 helices solved by X-ray crystallography; Top view and side view of the X-ray structures of the secondary transporters</b></p>						

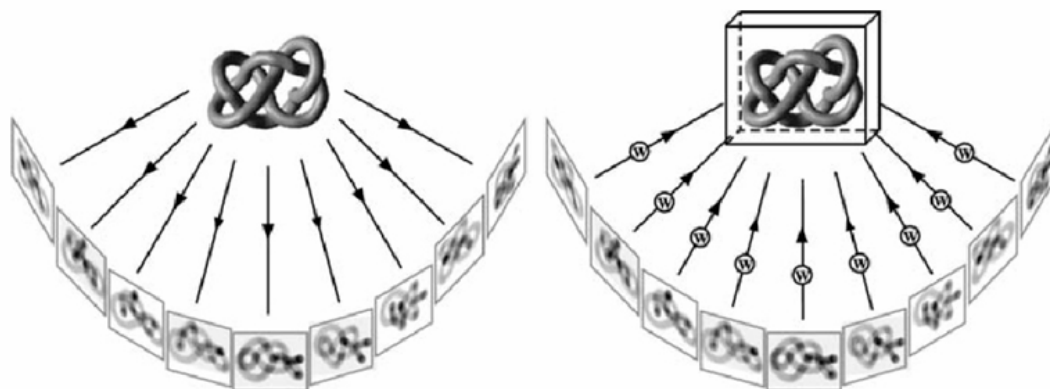
### 1.3.1. Electron microscopy and electron crystallography

Initially, electron microscopy (EM) was more popularly used in the field of material science. Since then design and capability of the electron microscope have improved, allowing to determine the structure of a protein at an atomic resolution by 2D crystals (Kühlbrandt, Wang et al. 1994; Subramaniam and Henderson 2000; Miyazawa, Fujiyoshi et al. 2003), huge protein complexes such as ribosome and chaperone by single particles (Ludtke, Chen et al. 2004; Ranson, Clare et al. 2006), and to visualize structural details of a cellular organelle like mitochondria and chloroplast (Shimoni, Rav-Hon et al. 2005; Gruska, Medalia et al. 2007; Sun, Williams et al. 2007). As in photography, EM data are recorded two-dimensionally on film or on a CCD camera, which only records the structural information in two dimensions. In



---

order to obtain the structural information in the third dimension, the specimens are tilted during data collection. Projections taken from different tilt views of an object are merged to reconstruct a three-dimensional density map (Figure 8).



**Figure 8. 3D reconstruction of an object (Lucic, Forster et al. 2005).**

EM data are collected as projections, which contain the structural information only in two dimensions. In order to obtain the information of the third dimension, projections of the object are collected at different tilt angles and tilt directions (left). 3D map of the object is reconstructed from merging projections with correct tilt geometry (right).

Radiation damage is one of the main limitations in electron microscopy, especially for studying fragile materials like biological samples. Electrons and charged particles interact with matter about 10,000 times stronger than X-ray beams (Fujiyoshi 1998). Inelastic electron scattering can cause chemical bond breakage, ionization, and free radical formation. Radiation damage destroys the structural information especially at high resolution. Cryo-EM was therefore introduced to reduce the effect of radiation damage by maintaining low temperatures during data collection. For example, temperatures of 20 K and 8 K applied can reduce the radiation damage on biological specimens to 1/10 and 1/20 respectively (Fujiyoshi 1998). Nowadays electron microscopes are often equipped with a cryo stage to keep the specimen at liquid nitrogen or liquid helium temperature. Images of untilted well-ordered two-dimensional (2D) crystals kept at liquid nitrogen or liquid helium temperature have often given information in the resolution range of 3-4 Å (Stahlberg, Fotiadis et al. 2001).

Sample preparation for cryo-EM is often performed by rapid freezing in

---

liquid nitrogen (77.5 K) or liquid ethane (95 K). Rapid freezing preserves the specimen in its native physiological state and immobilizes all constituents before severe structural changes occur. The importance of attaining such a low temperature in a rapid process is that the water molecules form amorphous vitreous ice whereas slow freezing causes ice crystal formation. The crystalline ice dehydrates the specimen, which leads to an increase of solute concentration causing structural changes of proteins.

Electron crystallography is especially advantageous for determining the structure of medium-sized membrane proteins for two reasons: (1) 2D crystallization reconstructs a native-like environment for membrane proteins to preserve their physiological conformations (see also **1.3.2.**), and (2) crystallography offers a way to extract the structural information from Fourier space which allows to significantly improve the obtained data during image processing. This is because membrane proteins are normally smaller than 100 kDa, and cannot be visualized easily on micrographs. Computational electron crystallography filters away the noise by boxing the reflections in the Fourier-transformed image in order to obtain a better contrast, and merging several lattices which increases the signal-to-noise ratio (S/N).

The greatest advantage of EM is that it records phase information directly. Unlike X-ray crystallography, EM imaging on 2D crystals is performed in real space, which contains the phase information which lacks in X-ray crystallographic data. To extract the amplitude and phase information, images are processed in real space and in Fourier space. The extracted amplitude and phase data are further used to calculate the structural factors without any bias.

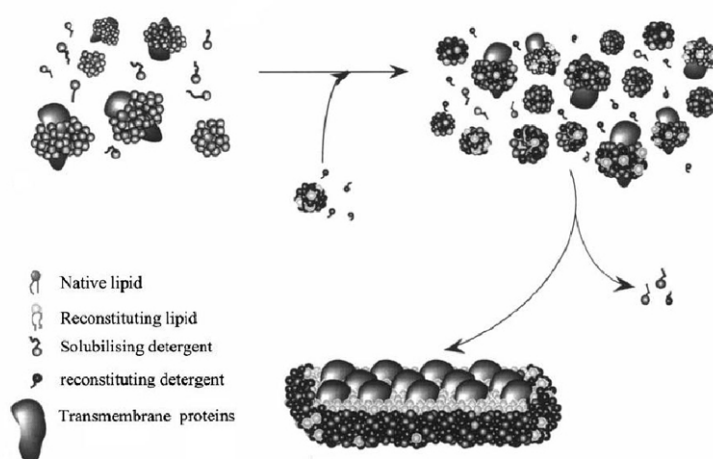
### **1.3.2. 2D crystallization**

Detergent-mediated reconstitution of membrane proteins is a frequently used method to prepare proteoliposomes for functional studies or 2D crystals for structural studies by cryo-EM and atomic force microscopy. Membrane proteins are known for their hydrophobicity. Ideally, overexpressed membrane proteins are incorporated and correctly folded into cell

---

membranes. To extract membrane proteins, detergents are introduced to disintegrate the cell membrane and stabilize proteins in an aqueous environment. Detergents have amphiphilic properties of a hydrophobic polycarbonyl chain and a hydrophilic head group. The membrane components, such as proteins and lipids, are mixed with detergents into a mixture of protein-lipid-detergent micelles. In these micelles, the hydrophobic regions of membrane proteins and lipids are surrounded by the hydrophobic tails of the detergent, while the hydrophilic regions are exposed to the hydrophilic head groups of the detergent and to the aqueous solution.

The behavior of detergent is a critical parameter for protein incorporation and crystallization. A most commonly used detergent in biological laboratories is sodium dodecylsulfate (SDS), which is a harsh detergent denaturing most proteins and thus not suitable for solubilization of membrane proteins. Non-ionic detergents are chosen for extracting proteins from membranes and protein purification. These detergents extract proteins without destroying their tertiary or quaternary structure. Dodecyl-maltoside (DDM), decyl-maltoside (DM) and octyl-glucopyranoside (OG) are the most widely used detergents for 2D crystallization.



**Figure 9. Two-dimensional crystallization by reconstitution (Mosser 2001).**

After protein purification, proteins are stabilized by detergent micelles. Additional lipids are added after they are solubilized in detergent solution. Proteins, lipids and detergents will reach the equilibration, which gives a mixture of protein-lipid-detergent micelles. Detergents are removed by dialysis or hydrophobic absorbance. Proteins are reconstituted into lipid bilayers. If proteins arrange into a regular array, then it is a 2D crystal which is suitable for electron crystallography.

---

After protein purification in the presence of detergents, additional lipids are often mixed with the protein samples to promote the formation of proteoliposomes and 2D crystals. The mixture of proteins, lipids and detergents reaches a dynamic equilibrium of protein-lipid-detergent micelles after being mixed. To reconstitute proteins into lipid bilayers, detergents are removed or diluted to a concentration below the critical micelle concentration (CMC). Below the CMC, detergents often exist as monomers, while monomers and micelles coexist when the detergent concentration is higher than the CMC. Methods such as dialysis, hydrophobic absorbance and dilution are often performed to reduce detergent concentration. Upon detergent removal, lipids then can transit from micelles to bilayers. Protein molecules can be incorporated into lipid bilayers, leading to densely packed proteoliposomes and 2D crystals (Figure 9).

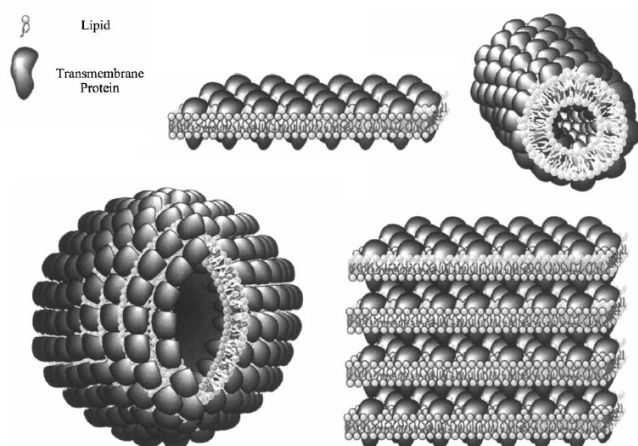
Phospholipids from natural sources or synthetic compounds are routinely used for 2D crystallization. Generally, the lipids favorable for 2D crystal formation depend on the target protein. Although there is no strict rule about choosing suitable lipids for 2D crystallization, the lipid composition of the cytoplasmic membrane of the native organism often offers a hint on suitable lipid species for 2D crystallization. Till date, natural or synthetic phosphatidyl choline (PC), PG, PE, and lipid extracts from cells have been successfully used in 2D crystallization. The charge of a lipid is determined by the head group, and the fluidity of the formed lipid bilayer is mainly determined by the chemical structure of the fatty acid chains. Lipid bilayers are more rigid if they contain more saturated fatty acid chains, while the fatty acid chain kinks introduced by *cis* double bonds increase the fluidity of a lipid bilayer.

Dialysis has been the most frequently used method for detergent removal. It offers a slow rate to remove detergents, whereas hydrophobic absorption removes detergents within a few minutes. A rapid decrease of detergent concentration usually leads to protein aggregates and a smaller size of proteoliposomes (Dolder, Engel et al. 1996). Dialysis is performed by introducing a detergent-free buffer, which mainly contains chemicals stabilizing the protein, such as pH buffer, salt and additives. During

---

crystallization, proteins are incorporated into lipid bilayers during the phase transition of lipids. To obtain well-diffracting 2D crystals, the lipid-to-protein ratio (LPR) is one of the most critical parameters (Schmidt-Krey, Lundqvist et al. 1998; Zhuang, Prive et al. 1999). For 2D crystallization, the LPR should be kept low in order to obtain densely packed lipid bilayers, whereas reconstituted proteoliposomes are obtained by using a high LPR, leading to loosely packed vesicles. On the other hand, a too low LPR also leads to protein aggregation because of insufficient lipids for protein reconstitution. Therefore, an appropriate LPR allows proteins to form densely packed 2D crystals without forming large amounts of protein aggregates.

Beside buffer and lipids, temperature is a critical factor determining whether 2D crystals are forming. Especially formation of the lipid bilayer is a temperature-dependent process because the phase transition temperature from lipid micelles to lipid bilayer depends on specific type of lipids used. Temperature also affects the detergent removal rate and protein stability in detergent micelles. Well-diffracting 2D crystals therefore only are formed at a narrow range of dialysis temperature.



**Figure 10. 2D crystal morphology (Mosser 2001)**  
2D crystals can have different forms: sheet, tubes, vesicles, and multilayers

Another remarkable advantage of 2D crystals is that the protein does not have crystal contacts in all dimensions and thus conformational changes can often be induced without destroying crystal order (Unwin, Miyazawa et al. 2002; Ruprecht, Mielke et al. 2004; Vinothkumar, Smits et al. 2005). In terms of morphology, 2D crystals can be classified based on three shapes: sheet,

tube, and vesicle (Figure 10). Some proteins tend to stack into multilayer crystals, while most of the reported 2D crystals are single-layered crystals. Small vesicles are frequently obtained at the initial screening stage of 2D crystallization, and indicate successful protein reconstitution. Sheet-like and tubular crystals form less readily but tend to have a higher degree of order and are favored for data collection. Table 2 summarizes 2D crystallization conditions used for secondary transporters; Table 3 lists the 2D crystals of membrane proteins which have resulted in atomic models (beyond 4 Å).

Proteins	Detergent used	Lipids	Dialysis buffer	Dialysis period and temperature	Symmetry and resolution	References
EmrE	DM, CHAPS	DMPC	20 mM pH 7.0 Na <sup>+</sup> phosphate, 100 mM NaCl, 2 mM MgCl <sub>2</sub> , 1 mM EDTA, 4 mM DTT, 4 mM 2-mercaptoethanol, 10 mM NaN <sub>3</sub>	10-14 days, 25°C	c222, p222 <sub>1</sub> , p2 (7 Å)	(Tate, Kunji et al. 2001)
MJNha P1	DM, DDM	<i>E. coli</i> lipids	25 mM pH 4 K <sup>+</sup> acetate, 0.2 M NaCl, 5 % glycerol, 5 % MPD	7 days, 37°C	p22 <sub>1</sub> 2 <sub>1</sub> (6 Å)	(Vinothkumar, Smits et al. 2005)
NhaA	DM, DDM	<i>E. coli</i> lipids	25 mM pH 4 K <sup>+</sup> acetate, 0.3 M KCl, 0.1 mM GdCl <sub>3</sub> , 5 % glycerol, 5 % MPD	7 days, 37°C	p22 <sub>1</sub> 2 <sub>1</sub> (4 Å)	(Williams, Geldmacher-Kaufer et al. 1999)
MelB	DDM	<i>E. coli</i> lipids	20 mM pH 6 citric acid, 200 mM NaCl, 5 mM melibiose, 10 % glycerol, 5 mM 2-mercaptoethanol	9-14 days, 21°C	p22 <sub>1</sub> (8 Å)	(Hacksell, Rigaud et al. 2002)
OxIT	OG, Cymal-7	POPC	150 mM K <sup>+</sup> acetate or 50 mM pH 4.5 K <sup>+</sup> citrate, 100 mM potassium oxalate, 6 mM 2-mercaptoethanol, 20 % glycerol	27°C; temperature cycling RT-37°C for 3 days	p22 <sub>1</sub> 2 <sub>1</sub> (6 Å); p22 <sub>1</sub> 2 <sub>1</sub> (3.4 Å)	(Heymann, Hirai et al. 2003)

**Table 2. 2D crystallization conditions for secondary transporters**

Protein	Morphology	Resolution in plane	Reference
Bacteriorhodopsin	Sheet	3.5 Å	(Henderson, Baldwin et al. 1990)
Light harvesting complex from pea	Sheet	3.4 Å	(Kühlbrandt, Wang et al. 1994)
Water channel (aquaporin AQP1) from human	Sheet	4 Å	(Ren, Cheng et al. 2000)
Water channel (aquaporin AQP0) from lens core	Sheet	1.9 Å	(Gonen, Cheng et al. 2005)
C-subunit rings of the F1F0 ATP synthase from <i>Ilyobacter tartaricus</i>	Vesicle	4 Å	(Vonck, von Nidda et al. 2002)
Acetylcholin receptor (ACh) from <i>Tripedo marmorata</i>	Tube	4 Å	(Unwin 2005)

**Table 3. List of 2D crystals which have resulted in atomic models.**

---

### 1.3.3. Data collection and processing

EM imaging of 2D crystals allows determination of the exact size and packing of the unit cell by analysis of the diffraction pattern in the Fourier-transformed image. Amplitudes and phases are further calculated by the following steps: filtering in Fourier space, cross-correlation in Fourier space (diffraction pattern) or real space (raw image), unbending, and correction of the contrast transfer function (CTF). The projection density map is back-Fourier-transformed from amplitudes and phases of reflections. It is possible that a unit cell contains more than one asymmetric unit. Each asymmetric unit must have a spatial relation to its neighboring asymmetric unit. The spatial relation in two dimensions can include rotation perpendicular to the 2D crystals, and/or an in-plane screw symmetry which in the case of 2D crystals is a combination of twofold rotation and translation in the same direction. From the spatial relations between the asymmetric units, crystal symmetry can be calculated and further defined as space groups.

To reconstruct a 3D volume from 2D projections, we need 2D projections of the object viewed from different angles. Tilted data collection is performed by imaging of tilted specimens in the microscope. The tilt geometry is calculated afterwards from the change of the unit cell compared to the untilted unit cell. A 3D data set is obtained from merging 2D projections with correct tilt geometry applied. By applying the symmetry, the signals from different asymmetric units are averaged, which can also enhance the signal-to-noise ratio.

## 1.4. Overview of this thesis

Up to the date, high resolution structure from the members of BCCT family has not yet been determined. Due to the role of BetP in osmoregulation and osmosensing, it became a major target in our lab, and this thesis focuses on the 2D crystallization and 3D map reconstruction of BetP by electron crystallography. Wild-type (WT) BetP has been successfully reconstituted and crystallized with the lipid mixture of *E. coli* polar lipids and bovine cardiolipin (3:2, w/w) (Ziegler, Morbach et al. 2004). However, these crystals were highly mosaic and not suitable for 3D map reconstruction. Different

---

truncated BetP mutants were therefore constructed in order to obtain better crystal quality for structure determination. A C-terminally truncated BetP mutant, BetP $\Delta$ C45 was chosen for 2D crystallization. Lipids used for BetP $\Delta$ C45 crystallization influenced crystal order and packing. Mass spectrometry by multiple precursor ion scanning was used to quantify the lipids present in different stages of the crystallization process. Crystals obtained by using *C. glutamicum* lipids had the best quality in terms of crystal packing and size, and were used for 3D map reconstruction. Using data from a series of tilted images, the three-dimensional structure of BetP $\Delta$ C45 was determined at 8 Å resolution. The structure shows BetP as a trimer with each monomer consisting of a bundle of 12 densities characteristic of membrane-spanning  $\alpha$ -helices. A potential substrate-binding chamber is formed by four helices. The diameter of this central cavity and the orientation of helices are different in each monomer. BetP is thus an asymmetric homotrimer with all three monomers in different conformations.



---

## 2. Materials and Methods

### 2.1. Protein expression and membrane preparation

#### 2.1.1. Materials and reagents

<i>E. coli</i> DH5 $\alpha$ -T1 strain	Competent cell (INVITROGEN)
<i>E. coli</i> BL21 (C43) strain	Competent cell (from John Walker's lab, MRC, UK)
SOC medium	Bacto-tryptone 20 g, Bacto-yeast extract 5 g, NaCl 0.5 g, KCl 0.186 g, glucose 2.4 g, adjusted to pH 7.0 with NaOH, in 1 liter
Luria-Bertani broth (LB broth)	Bacto-tryptone 10 g, Bacto-yeast extract 5 g, NaCl 10 g in 1 liter (pH 7.0)
LB agar plate	
Ampicillin	Antibiotics
Carbenicillin	Antibiotics
AHT	Anhydrotetracyclin
Tris	C <sub>4</sub> H <sub>11</sub> NO <sub>3</sub> 2-amino-hydroxymethylpropane-1,3-diol
Pefabloc	C <sub>8</sub> H <sub>10</sub> NSO <sub>2</sub> F·HCl [4-(2-Aminoethyl)benzenesulfonylfluoride.HCl], protease inhibitor (BIOMOL)
Membrane buffer	50 mM pH 7.5 Tris-HCl, 1 mM pefabloc
Bradford assay reagent	Coomassie dye binding protein assay, protein dye (SIGMA)

#### 2.1.2. Plasmid preparation and transformation

The plasmid of pASK-IBA5 *betP* $\Delta$ C45 was constructed by Dr. D. Schiller in Prof. R. Krämer's laboratory at Insitut für Biochemie, Universität zu Köln (Schiller, Rübenhagen et al. 2004). A *Strep*-tag II was fused to the N-terminus of BetP $\Delta$ C45, giving NH<sub>4</sub><sup>+</sup>-WSHPQFEK-BetP $\Delta$ C45. The competent cells (aliquot of 50  $\mu$ l) were gently thawed on ice, and mixed with the constructed plasmid (~10 ng), followed by incubation for 30 min on ice. For *E. coli* BL21 (C43) strain, heat shock was performed at 37°C for 42 seconds, while *E. coli* DH5 $\alpha$ -T1 cells were heat-shocked at the same temperatire for 20 seconds. Heat-shocked cells were afterwards incubated on ice for 2 min. SOC medium (500  $\mu$ l) was added to *E. coli* BL21 (C43) cells and incubated in a shaker at 37°C for 30 min for cell growth. *E. coli* DH5 $\alpha$ -T1 cells were directly plated after heat-shock. Cells were plated on LB-agarose plates containing 5  $\mu$ g/ml ampicillin or carbenicillin, and incubated overnight at 37°C. Individual colonies were picked for initiating cell culture.

---

### 2.1.3. Culture growth and protein expression

The LB medium used for cell culture and protein expression contained 5 µg/ml ampicillin or carbenicillin, and the cell culture growth was performed at 37°C. Individual colonies were cultivated independently for 16 hours as preculture. The preculture was amplified from 100 ml to two liter and shaken for another 3-4 hours. Cells were induced with 200 µg/l of AHT in the growth medium to allow protein expression for another 3-4 hours. Cells were harvested by centrifugation, resuspended in the membrane buffer, and stored at -20°C.

### 2.1.4. Membrane preparation

The cells were homogenized and passed through a nylon gaze to remove big clumps. Cells were broken by passing through a cell disruptor with a constant pressure of 1.5-2.0 kbar. Unbroken cells and cell debris were removed by centrifugation at 29000 × g for 30 min. Cell membrane was harvested by ultracentrifugation at 235000 × g for 90 min, homogenized in the membrane buffer (50 mM pH 7.5 Tris-HCl, 1 mM pefabloc) to 15-20 mg/ml, and stored at -20°C. Membrane concentration was measured by standard Bradford protein assay.

## 2.2. Protein purification and quality analysis

### 2.2.1. Materials and reagents

Glycerol	C <sub>3</sub> H <sub>8</sub> O <sub>3</sub> propane-1,2,3-triol (MERCK)
Dodecyl maltoside (DDM)	C <sub>24</sub> H <sub>46</sub> O <sub>11</sub> (GLYCON)
<i>Strep</i> -Tactin resin	(IBA)
d-Desthiobiotin	C <sub>10</sub> H <sub>18</sub> N <sub>2</sub> O <sub>3</sub> (SIGMA)
Buffer A	50 mM pH 7.5 Tris-HCl, 200 mM NaCl
Buffer B	50 mM pH 7.5 Tris-HCl, 200 mM NaCl, 10 % glycerol
Washing buffer	50 mM pH 7.5 Tris-HCl, 200 mM NaCl, 10 % glycerol, 0.04 % DDM
Elution buffer	50 mM pH 7.5 Tris-HCl, 200 mM NaCl, 10 % glycerol, 0.04 % DDM, 5 mM desthiobiotin
Sample buffer (4X)	160 mM DTT, 30 % glycerol, 500 mM pH 6.8 Tris, 10 % SDS, 0.4 % bromphenolblue
SDS	Sodium dodecylsulfate
PAGE buffer (5X)	250 mM pH 8.6 Tris-HCl, 500 mM glycine, 50 mM SDS

PVDF membrane	Polyvinylidene fluoride, 0.45 $\mu$ m (MILLIPORE)
Transfer buffer	100 mM pH 8.3 Tris-HCl , 0.2 % SDS, 10 % methanol
PBS buffer	4 mM KH <sub>2</sub> PO <sub>4</sub> , 16 mM NaH <sub>2</sub> PO <sub>4</sub> , 115 mM NaCl
Blocking buffer	3 % bovine serum albumin dissolved in PBS buffer
Antibody I	Unconjugated <i>Strep</i> -tag II monoclonal antibody (IBA), diluted to 200 ng/ml in PBS buffer
Antibody II	Rabbit anti mouse antibodies (SIGMA), diluted 4000 $\times$ with PBS buffer
SIGMA FAST® BCIP/NBT	(5-Bromo-4chloro-3-indolyl phosphate/ Nitro blue tetrazolium) tablet (SIGMA), dissolved in 10 ml water for each tablet

### 2.2.2. Membrane solubilization

Membrane solubilization was performed at 4°C or on ice. The solubilization buffer was prepared to contain pH 7.5 Tris-HCl, glycerol, pefabloc, and DDM. The homogenized membrane solution was added drop by drop to the solubilization buffer stirred to have the final solution containing 5 mg/ml membrane, 50 mM pH 7.5 Tris-HCl, 20 % glycerol, 1 mM pefabloc, and 1.5 % DDM. The solution was under stirring for 30 min. Insoluble part was removed by ultracentrifugation at 235000  $\times$  g for 30 min. The fraction of supernatant was diluted with buffer B to 3 volumes.

### 2.2.3. Protein purification

Protein purification was performed at 4-6°C. The affinity column of 4 ml packed *Strep*-Tactin matrix was equilibrated with > 30 column volume (CV) of buffer A and > 30 CV of buffer B respectively. The diluted membrane solution was loaded to the column and allowed to flow through by gravity. The column was washed with 7 CV of the washing buffer. BetP $\Delta$ C45 was eluted afterwards by washing the column with the elution buffer at a controlled flow rate of 50  $\mu$ l/min.

### 2.2.4. SDS polyacrylamide gel electrophoresis

Protein samples or cell extract were diluted with the sample buffer to 2 volumes, and incubated at room temperature (RT) for 10 min. Samples of interest and protein standard markers were loaded on a 10 % or 12 %

---

polyacrylamide gel. The gel was equilibrated in the PAGE buffer, run at a voltage of 140 V for about 1.5 hour, and stained with Coomassie Brilliant Blue R 250.

### 2.2.5. Western blotting

A PVDF membrane was washed with 100 % methanol and water for 5 min respectively, and equilibrated in the transfer buffer. Four pieces of Whatman paper were soaked in the transfer buffer. The gel was transferred onto a PVDF membrane between four pieces of pre-soaked Whatman papers, and applied with 15 V in a semi-dry blotting system (BIORAD) for 35 min. The PVDF membrane was incubated in the blocking buffer at room temperature for 1 hour or at 4°C for overnight with gentle shaking. After the PVDF membrane was washed three times with PBS buffer for 5 min, it was incubated in Antibody I solution for an hour at room temperature with shaking. After incubation, the membrane was washed with PBS 3 times for 5 min, and transferred to Antibody II solution for incubation at room temperature for 0.75-2 hours under gentle shaking. Membranes were washed as described above. To visualize the bands in the membrane, chromogenic reaction was carried out by incubating the membrane with the SIGMA FAST™ solution in the dark for 10 min at room temperature. The chromogenic reaction was quenched by washing the membrane with water several times. The membrane was air dried and stored in the dark.

## 2.3. *C. glutamicum* lipid preparation

### 2.3.1. Material

<i>Corynebacterium glutamicum</i>	<i>C. glutamicum</i> strain CglΔotsAΔtreSΔtreY which lacks of the peptidoglycan layer
CGXII minimum medium	42 g MOPS (morpholinopropane sulfonic acid) pH 7.0, 20 g (NH <sub>4</sub> ) <sub>2</sub> SO <sub>4</sub> , 5 g urea, 1 g K <sub>2</sub> HPO <sub>4</sub> , 1g KH <sub>2</sub> PO <sub>4</sub> , 40 g sucrose, 10 mg CaCl <sub>2</sub> , 0.25 g MgSO <sub>4</sub> ·7H <sub>2</sub> O, 0.2 mg biotin. 0.03 g 3,4-dihydroxybenzoic acid, 10 mg FeSO <sub>4</sub> ·7H <sub>2</sub> O, 10 mg MnSO <sub>4</sub> ·H <sub>2</sub> O, 1 mg ZnSO <sub>4</sub> ·7H <sub>2</sub> O, 0.2 mg CuSO <sub>4</sub> , 0.02 mg NiCl <sub>2</sub> ·6H <sub>2</sub> O in one liter
Dextran gel	Sephadex G-25 medium (AMERSHAM)
Silicic acid 200 mesh	(SIGMA)

---

### 2.3.2. Culture growth

*C. glutamicum* cells were plated on a LB-agar plate and incubated at 37°C overnight. The cells on the LB agar plate were inoculated to 10 ml of LB medium and cultivated at 37°C with shaking speed of 210 rpm to an optical absorption ( $A_{600}$ ) of 1. This culture was amplified to 100 ml in CGXII minimum medium and cultivated to an  $A_{600}$  of 1 (30°C, 210 rpm). Subsequently, the cells were subcultured in 1 liter of CGXII minimum media and grown to an  $A_{600}$  of 1. Cells in the final culture having an  $A_{600}$  of 1 were harvested by centrifugation, and stored at -20°C.

### 2.3.3. Lipid preparation, extraction, and lipid polarization

Membrane preparation of *C. glutamicum* was performed as described for *E. coli* cells in 2.1.4. Lipid extraction was done by the Folch extraction method (Folch, Lees et al. 1957). *C. glutamicum* cells or membranes were blended with methanol to a concentration of 0.1 g/ml, followed by adding two volumes of chloroform. The mixture was stirred at room temperature for 4 hours. The solution was passed through two pieces of Whatman filter paper (No. 4). The solid residue was washed with 20 ml of chloroform/methanol (2:1) and filtered again. After the filtrates were combined, 0.88 % KCl solution was added to dilute the filtrates 1.25 times. The mixture was transferred to a separation funnel, shaken for 1 min, and allowed to phase separate in the dark at 4°C. After phase separation, the lower organic phase was collected and dried under vacuum by a rotary evaporator. A pinch of Dextran gel (~ 0.2 g) was added to the chloroform-dissolved extract to absorb water, and washed three times with chloroform. In the final washing, the Dextran gel was removed by a sintered glass funnel. After the chloroform was evaporated, the dried extract was quantified by a micro balance. The crude extract was dissolved in chloroform to the desired concentration.

Polar lipids were separated from the crude extract by a silicic acid column. The required amount of silicic acid (1 g silicic acid for 10 mg lipids) was tightly packed and equilibrated with chloroform. The silicic acid column loaded with the crude extract was washed with 10-15 CV chloroform, 10-40 CV acetone, and 5-20 CV methanol respectively. The methanol fraction

---

containing polar lipids was dried in a rotary evaporator, and the dried material was weighted and re-dissolved in chloroform to the desired concentration.

#### **2.3.4. Lipid analysis**

Lipid samples were preliminarily evaluated by thin-layer chromatography (TLC). A TLC plate ( $10 \times 10 \text{ cm}^2$ ) with samples loaded was developed in the running buffer (chloroform: methanol: acetone: acetic acid: water = 50: 10: 20: 10: 5). The lipid patterns on TLC plates were visualized by iodine vapor, and stained permanently by sulfuric acid.

Lipid samples were further analyzed by our collaborator, Dr. Christer S. Ejsing in Dr. Andrej Shevchenko's lab at the Max-Planck Institute of Molecular Cell Biology and Genetics, 01307 Dresden, Germany.

To separate 2D crystals from empty membranes, the dialysate was briefly centrifuged ( $34 \times g$ , 10 sec), and the supernatant removed. The pelleted material was subsequently washed 2 times by resuspension in dialysis buffer followed by brief centrifugation. The three 2D crystal preparations (LPR 0.15) and purified BetP $\Delta$ C45 were subjected to lipid extraction according to Folch (Folch, Lees et al. 1957). 50-100  $\mu\text{l}$  of each sample was mixed with 500  $\mu\text{l}$  of chloroform/methanol (1:1). 125  $\mu\text{l}$  of water was added for phase separation using centrifugation ( $11000 \times g$ , 5min). The organic phase was collected and air-dried. The total lipid extracts were stored in chloroform at  $-20^\circ\text{C}$ . Prior to the analysis, total lipid extracts were diluted to a total lipid concentration of  $\sim 3 \mu\text{M}$  (estimated by the LPR) in methanol containing 2  $\mu\text{M}$  methylamine. A mixture of internal standards was spiked into the samples at the following concentrations: 0.10  $\mu\text{M}$  CL 14:0-14:0-14:0-14:0, 0.15  $\mu\text{M}$  phosphatidic acid (PA) 17:0-17:0, 0.15  $\mu\text{M}$  PE 17:0-17:0, 0.10  $\mu\text{M}$  PG 17:0-17:0, 0.36  $\mu\text{M}$  phosphatidyl inositol (PI) 17:0-17:0 and 0.1  $\mu\text{M}$  diacylglycerol (DAG) 17:0-17:0. Quantitative lipid analysis was performed by multiple precursor ion scanning in negative ion mode as previously described (Ejsing et al. 2006) on a hybrid QSTAR Pulsar i quadrupole time-of-flight mass spectrometer (MDS Sciex, Concord, Canada) equipped with a robotic nanoflow ion source NanoMate HD System (Advion Biosciences, Inc., Ithaca,

NJ). Twenty-one precursor ion spectra were acquired for structure-specific fragment ions produced by collision-induced dissociation of molecular anions of glycerophospholipids. The list of specific fragment ions was compiled from pre-computed m/z of head group derived fragment ions and acyl anions of all plausible fatty acid moieties having a total number of carbon atoms ranging from 10 to 20 with either 0, 1 or 2 double bonds. Automated processing of acquired spectra, identification and quantitation of detected molecular glycerophospholipid species was performed by Lipid Profiler software (MDS Sciex) as previously described (Ejsing et al. 2006).

## 2.4. 2D Crystallization

### 2.4.1. Materials and reagents

Decyl maltoside (DM)	C <sub>22</sub> H <sub>42</sub> O <sub>11</sub> GLYCON
<i>E. coli</i> polar lipids	AVANTI POLAR LIPIDS
Cardiolipin from bovine heart	AVANTI POLAR LIPIDS
1-palmitoyl-2-oleoyl- <i>sn</i> -glycerol-3-[phospho- <i>rac</i> -(1-glycerol)] (PG 16:0-18:1)	AVANTI POLAR LIPIDS
<i>C. glutamicum</i> crude extract or polar lipids	See <b>2.3.</b>
Dialysis chamber	mini slide-A-lyzer, or dialysis cassette 10 KDa molecular weight cut-off (PIERCE, Rockford, IL)

### 2.4.2. Incubation

Protein samples were concentrated by centrifugation with a Centricon concentrator with a 100 kDa molecular weight cut-off if needed. Organic solvent in lipid samples was evaporated with a stream of nitrogen gas. Dried lipids were re-dissolved in 1 % DM and adjusted to 4 mg/ml. Protein-lipid-detergent mixture was prepared from mixing water, detergent, lipids, and protein together respectively, and finally contained 0.15% DM, 2-2.5 mg/ml protein, lipids at LPR of 0.05-0.2. Protein-lipid-detergent mixtures were incubated at 4°C for overnight or at room temperature for 30 min.

Different lipid mixtures were screened:

<b>A.</b>	Mixture of <i>E. coli</i> polar lipids and cardiolipin from bovine heart	<i>E. coli</i> polar lipids 30-100% Bovine cardiolipin 70-0%
<b>B.</b>	<i>C. glutamicum</i> crude extract or polar lipids	100%
<b>C.</b>	Mixture of [ <i>C. glutamicum</i> lipid extract] and [ <i>E. coli</i> polar lipids/bovine cardiolipin, 3:2 (w/w)]	[ <i>C. glutamicum</i> lipid extract] 25-75% [ <i>E. coli</i> polar lipids/bovine cardiolipin, 3:2 (w/w)] 75-25%
<b>D.</b>	PG 16:0-18:1	100%

### 2.4.3. Detergent removal

An aliquot of 50  $\mu$ l protein-lipid-detergent mixture was transferred to a mini Slide-A-lyzer with a molecular weight cut-off of 10 kDa, or 100  $\mu$ l to a dialysis cassette with the same molecular weight cut-off. Dialysis was carried out for 2-4 weeks at temperatures between 4-37°C.

Dialysis buffer conditions screened:

<b>pH buffer</b>	NaOAc, MES, Tris	50 mM, pH 4.0-9.0
<b>Monovalent salt</b>	LiCl, NaCl, KCl	0-1 M
<b>Divalent salt</b>	MgCl <sub>2</sub> , CaCl <sub>2</sub> , CoCl <sub>2</sub> , CuCl <sub>2</sub> , Cd(OAc) <sub>2</sub>	0-100 mM
<b>Additive</b>	2-methyl-2,4-pentanediol (MPD)	0-20%
<b>Additive</b>	Glycerol	0-20%
<b>Bacteriostatic antibiotics</b>	NaN <sub>3</sub>	3 mM
<b>Substrate</b>	Glycine-betaine	0, 5 mM

## 2.5. Electron microscopy

### 2.5.1. Data collection of negatively stained samples

An aliquot of dialysate (3  $\mu$ l) was applied on a carbon-coated Cu grid (400 mesh) for 1 min. The excess solution was removed by the smooth edge of a piece of Whatman paper No. 4. The carbon-coated side of the grid was washed once with 3  $\mu$ l of 1% uranyl acetate, and incubated with another 3  $\mu$ l of 1% uranyl acetate for 1-2 min. The excess uranyl acetate solution was removed by the rough edge of a piece of Whatman No.4 paper. The grid was inserted into an electron microscope (Philips CM12, CM120, or FEI Tecnai G<sup>2</sup> Spirit). The microscopes were equipped with a LaB<sub>6</sub> filament and operated at



---

low-dose mode (10-20 electrons/Å<sup>2</sup>) at an acceleration voltage of 120 kV.

Images were taken on a CCD camera with 2k × 2k or 1k × 1k pixel areas or on Kodak SO-163 films at a magnification of 45000 for the CM12 or CM120 microscope, and of 42000 for the Tecnai G<sup>2</sup> Spirit microscope. Negatives were developed in a Kodak D-19 developer for 12 min, followed by washing with deionized water (1 min) and fixation for 8 min. Images taken on CCD cameras were examined by real-time Fourier calculation, while negatives were evaluated by optical diffraction.

### **2.5.2. Cryo data collection**

Specimens for cryo data collection were prepared by the back-injection method (Wang and Kühlbrandt 1991; Williams, Geldmacher-Kaufer et al. 1999). A 0.5 × 0.5 cm<sup>2</sup> carbon film was cut and floated on 1 ml of the embedding medium (4-10 % trehalose, 4-20 % glucose, or 0.5 % pH 6.5 tannin-NaOH). The mesh side of a copper or molybdenum grid was used to pick up the carbon film. 2 µl of the embedding medium was removed from the carbon-free side of the grid. 1.5 µl of the dialysate was applied on the carbon-free side of the grid and gently mixed with the rest of the embedding medium. The dialysate was allowed to settle for 1 min on the grid, and 1.5 µl of the solution was removed afterwards. The grid was blotted on two pieces of Whatman No. 4 paper on the carbon-free side for 20-120 seconds. The grid was plunged into liquid nitrogen and transferred to a liquid-nitrogen-precooled cartridge for a JEOL 3000 SFF microscope or for a FEI Tecnai G<sup>2</sup> Polara microscope. Tilted data was collected in a JEOL 3000 SFF microscope by tilting specimens using cartridges with different tilt angles (10°, 20°, 30°, and 50°). The JEOL 3000 SFF microscope was equipped with a precooled specimen chamber at 4 K, and the FEI Tecnai G<sup>2</sup> Polara was equipped with a precooled specimen chamber at 93 K. The microscopes were both operated at acceleration voltage of 300 kV. Images were taken on Kodak SO-163 electron emulsion films at a magnification of 45000, 53000, 59000, or 70000 with a flood exposure beam (Polara) or spot scanning (JEOL), corresponding to a total electron dose of 10-20 electron/Å<sup>2</sup>. Negative development procedure was as described in **2.5.1**.

---

## 2.6. Data Processing

Micrographs were evaluated by optical diffraction, and areas of 6000 × 6000 pixels were selected and digitized by a Zeiss SCAI scanner with a scanning pixel size of 7 μm, corresponding to 4.2 cm × 4.2 cm at a resolution of 7 μm per pixel. The scanned image was transformed to MRC format (TIF2MRC). The MRC image processing software package was used for processing a single image and data merging (Crowther, Henderson et al. 1996); the CCP4 program suite was used to create projection maps and the 3D map.

### 2.6.1. Single image processing

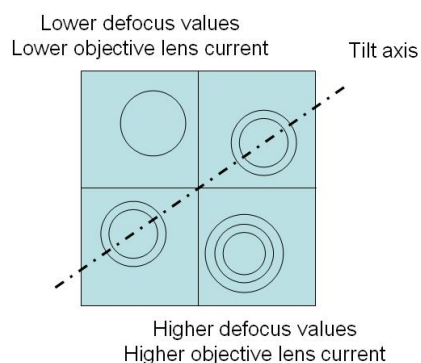
Scanned images were evaluated for diffraction quality in the calculated Fourier transform (TAPEREDGEK, LABEL, and FFTRANS), which was displayed by Ximdisp (Smith 1999). Unit cell parameters were determined by manually selecting the lattice dimensions in the Fourier transform image. To create a reference area, the noise was filtered in Fourier space by masking the diffraction spots, which was further used to calculate the back-Fourier transform into real space (MASKTRANA, FFTRANS). The reference area was boxed out from the filtered images. The position of the reference area was evaluated by the cross-correlation map between the whole image and the chosen reference area (QUADSERCHK). 2-3 passes of unbending were used with a reference area of 1 % of total pixel area for the first pass and 0.25 % for the last pass (CCUNBENDK). The phase and amplitude were printed out for each reflection (MMBOXA). The contrast transfer function was defined by three values: defocus1, defocus2, and astigmatism, which were calculated by CTFFIND. These values were applied to correct the phase (CTFAPPLY) of each reflection. Projection maps derived from the print-out of phases and amplitudes were scaled to a maximum density of 250 and contoured in steps of 17.5 with a negative temperature factor of -200 Å<sup>2</sup> applied (F2MTZ, FFT, EXTEND, NPO). The crystal plane group symmetry was calculated for 0° cryo data from reflections of IQ 1-5 (ALLSPACE) (Valpuesta, Carrascosa et al. 1994).

$$IQ = 7 \times \frac{(\text{intensity of noise})}{(\text{intensity of signal})}$$

---

## 2.6.2. Tilt geometry refinement

The Preliminary tilt geometry was calculated for tilted data (EMTILT). The sign of tilt angle (+/-) was defined to be positive if the tilt  $\alpha^*$  located at the side of lower objective lens current (less underfocus). The tilt geometry was also examined by partitioning the raw image (MRC format) into 2 x 2 squares. The contrast transfer function was calculated for these four squares individually. By comparing defocus1 and defocus2 of these four squares, the sign of tilt angle could be determined. The lower values of defocus1 and defocus2 referred to the side of lower objective lens current (Figure 11). The final tilt geometry was refined one time by using a preliminary 3D data (MTZ format) as a reference (ORIGTILTK).



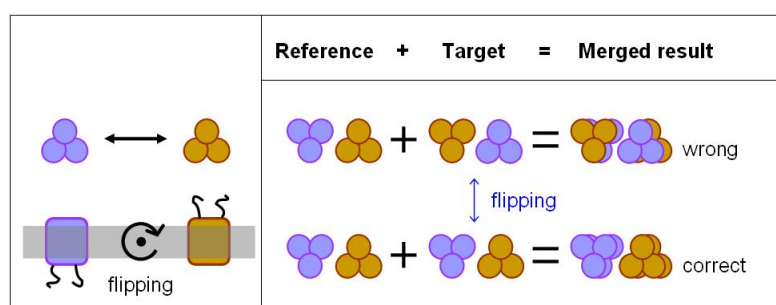
**Figure 11. Defining the tilt direction by calculating CTF values of partitions of the raw image.**

The raw image was cut into four squares each square was calculated for its CTF value individually. The CTF value determines the Thon ring size as the circles represent in this figure.

## 2.6.3. Handedness determination

Due to the symmetry of p12<sub>1</sub>\_b (“b” indicates that the screw axis is along the Y dimension), it was necessary to determine the handedness for each lattice. The best 0° image was chosen as a reference image. Handedness determination was performed by comparing the target image against the reference image (ORIGTILTK) (Figure 12). The phase residual of the target image described the dissimilarity to the reference image. By comparing the phase residual with and without flipping the target image, the handedness could be determined. After the handedness determination and phase origin refinement (see 2.6.4.), 0° images were merged together in order to create a 0° reference data set in APH format. This 0° reference data set was used for handedness determination of the 10° images. Lattices of 0° and 10° were merged together after handedness determination of 10° images. Reference

data sets of 10°, 20°, and 30° were prepared following the same strategy and utilized for handedness determination for 20°, 30°, and 50° images, respectively. During handedness determination for tilted data, approximately correct tilt geometry was applied in order to fit reflections into the  $l^*$  dimension in Fourier space correctly.



**Figure 12. Handedness check during merging**

Because of symmetry  $p12_1_b$ , it was required to examine the handedness of the target image against the reference.

#### 2.6.4. Data merging

After the handedness determination, phase origins of target images were refined and shifted to the same phase origin of the reference image. Phase origin was refined for reflections with IQ 1-4 at lower resolution (12 Å for 0°-30° and 15 Å for > 30°) with symmetry  $p12_1_b$  applied (ORIGTILTK). Reflections of IQ 1-6 were merged up to 8 Å (ORIGTILTK).

To calculate a projection map from the merge data, the phase and amplitude were averaged for each reflection from different images (AVRGAMPHS). The averaged amplitudes and phases were used to plot the projection map, which was scaled to a maximum peak of 250 and contoured by a step of 17.5 with a B factor of  $-250 \text{ \AA}^2$  applied.

#### 2.6.5. 3D map reconstruction

After merging all the images, LATLINPRESCALE was used to correct the amplitudes of the merged 3D data, which were affected by CTF. LATLINPRESCALE also calculated the appropriate weight for each reflection (Agard 1983). The 3D data was evaluated by LATLINEK (Agard 1983), which fits curves for amplitudes and phases for individual reflections by weighting least-square error between structural factors and phases. These curves were

---

lattice lines describing amplitudes and phases along the  $I^*$  dimension ( $1/Z$ ). Improper reflections were removed based on the lattice lines and restrictions from the symmetry, ex.  $(h,k,l) = (0, 2n+1, 0)$ . The modified 3D data was reformatted (PREPMKMTZ) and back-converted from Fourier space to real space (F2MTZ, FFTBIG, and MAPMASK). The 3D map was visualized in the graphics program O (Jones, Zou et al. 1991) and Pymol (DeLano 2002). Protein models were manually created from dummy poly-Ala helices for one monomer in the program O (Jones, Zou et al. 1991). The protein model was rotated and translated to the density of the other two monomers as a starting template. For the other two monomers, their protein models were manually adjusted to fit the map features.

### **2.6.6. Non-crystallographic symmetry of the 3D map**

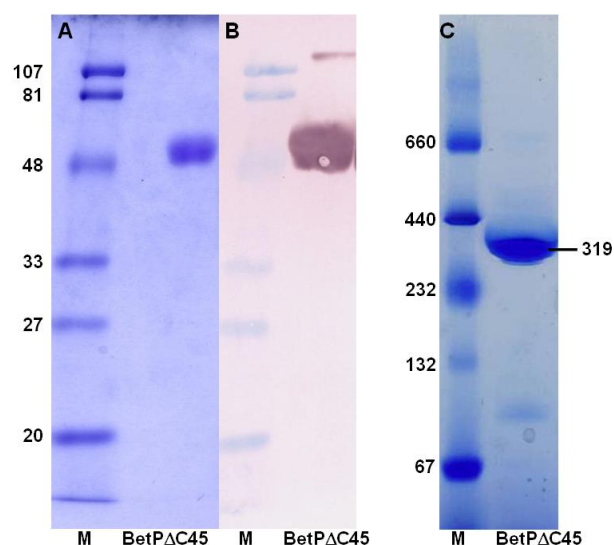
To compare the conformations and spatial relations of the three monomers, the non-crystallographic symmetry (NCS) was calculated. A strategy was designed for NCS calculation: (i) calculate the mass center of each monomer; (ii) mask the density map for each monomer with a reasonable size; (iii) calculate the correlation map between every two monomers; (iv) average the masked densities from every two monomers. The Uppsala Software Factory programs were used for NCS calculation: COMA, MAMA (Kleywegt and Jones 1999), and AVE (Kleywegt and Read 1997) in the RAVE package. The pseudo threefold symmetry operators between every two monomers were calculated by comparing spatial relations of two protein models using the LSQ option in O (lsq\_explicit, lsq\_improve) (Jones, Zou et al. 1991). The mass center was calculated (lx\_moleman) and treated as the center for masking the density of each monomer with a fixed radius of 20 Å (lx\_mama). The masked densities were correlated against each other to fine-tune the relative positions (lx\_imp). The improved matrix was applied to calculate the correlation map from every two monomers (lx\_coma). The averaged map from every two masked monomer densities was prepared using lx\_ave. These correlation maps were visualized at  $\sigma$  cut-off of 0.675.

---

## 3. Results

### 3.1. Characterization of BetP $\Delta$ C45

Protein expression of BetP $\Delta$ C45 typically yielded  $\sim 0.2$  mg of purified BetP $\Delta$ C45 per liter of *E. coli* culture. To extract the protein from the cell membranes, an aqueous solution of the detergent dodecyl maltoside was used. The sequence WSHPQFEK was introduced as the N-terminal tag and facilitates high specificity binding to the strepavidin derivative Strep-Tactin. This allowed one-step purification of detergent-solubilized BetP $\Delta$ C45 with a purity higher than 95 % as indicated by SDS-PAGE and Western blot analysis (Figure 13A, B). The theoretical molecular weight of BetP $\Delta$ C45 is 59.6 kDa for 558 amino acids, including the *Strep*-tag. Blue native gel electrophoresis resulted a band with a molecular weight of  $\sim 319$  kDa (Appendix I, Figure 13C). If the bound detergent is taken into account, this agrees well with the reported trimeric state of the wild type BetP (Ziegler, Morbach et al. 2004).



**Figure 13. DDM-solubilized BetP $\Delta$ C45 after protein purification.**  
(A) SDS-PAGE; (B) Western blot; (C) Native gel.

### 3.2. 2D Crystallization

#### 3.2.1. Detergents, lipids, and temperature

##### Detergents

The purified protein was directly used for 2D crystallization if the protein concentration was  $> 3$  mg/ml, otherwise the protein was concentrated with a

---

concentrator with a molecular weight kDa cut-off 100 kDa. Lipids dissolved in decyl maltoside (DM) resulted in large crystalline areas as compared to CYMAL-7. A standard set-up of pre-dialysis protein-lipid-detergent mixture contained < 0.02% DDM and 0.15% DM. A higher concentration of either detergent led to deterioration of the crystal quality and resulted in lower resolution even when the detergent was removed by dialysis. The dialysis was performed for three weeks at > 30°C to remove most of the detergents.

## Lipids

BetP $\Delta$ C45 was initially reconstituted with an *E. coli* lipid extract into small vesicles (< 0.5  $\mu$ m) by dialysis against a buffer containing 50 mM pH 7.5 Tris, 200 mM NaCl, 5 % glycerol, 5 % MPD, 3 mM NaN<sub>3</sub>, and 4 mM CaCl<sub>2</sub>. These vesicles already showed a weak diffraction pattern in the Fourier-transformed image, but they were too small for data collection (Figure 14 A). Cardiolipin (CL) from bovine heart was found to enlarge the size of crystalline areas when added to the *E. coli* lipid extract for crystallization. A ratio of 3:2 (w/w) of *E. coli* polar lipid extract/bovine CL was optimal and resulted in large sheets and vesicles (10  $\mu$ m). Ratios of 4:1 and 3:7 resulted in formation of small, round vesicles (<1  $\mu$ m) which were not preferred for data collection. Since BetP originates from *C. glutamicum*, lipids extracted from *C. glutamicum* cells were also tried for 2D crystallization. Lipid analysis by TLC and MS indicated that PG 16:0-18:1 is the most dominant lipid species in the *C. glutamicum* lipid extract (see 3.6. for further details). Therefore, synthetic PG 16:0-18:1 was used for crystallization. BetP $\Delta$ C45 was successfully reconstituted into *C. glutamicum* lipids and PG 16:0-18:1 (see 3.2.2.) *C. glutamicum* lipids and the mixture of *E. coli* lipids and bovine cardiolipin (3:2, w/w) both yielded crystals diffracting to 7-8 Å; crystals obtained from synthetic PG 16:0-18:1 showed diffractions to ~12 Å. The projection structures from crystals obtained from these three lipids were described in sections from 3.3 to 3.5. Crystals obtained by using *C. glutamicum* lipids were chosen for 3D map reconstruction (see 3.7.).

## Lipid-to-protein ratio

The amount of added lipids played a mayor role in determining the crystal quality. For 2D crystallization of Betp $\Delta$ C45, a lipid-to-protein ratio

---

(LPR) of 0.15 (w/w) was found to be optimal in obtaining well-diffracting (8 Å) crystals. This optimal LPR was irrelevant of the lipids chosen for crystallization. Without any additional lipids (LPR 0), the protein formed mostly aggregates and very few 2D crystals (< 5%), probably with the lipids co-purified from the *E. coli* cells. These crystals had well-ordered but small lattice areas, judged from the weak, sharp reflections in the Fourier-transformed image. The intensity of reflections reveals the size of the crystalline area, and the sharpness indicates its mosaicity. Adding lipids up to an LPR of 0.15 yielded a minimal amount of protein aggregates. In contrast, an excess of lipids (LPR > 0.18) led to loosely-packed crystals, as indicated by blurred reflections in the Fourier transform.

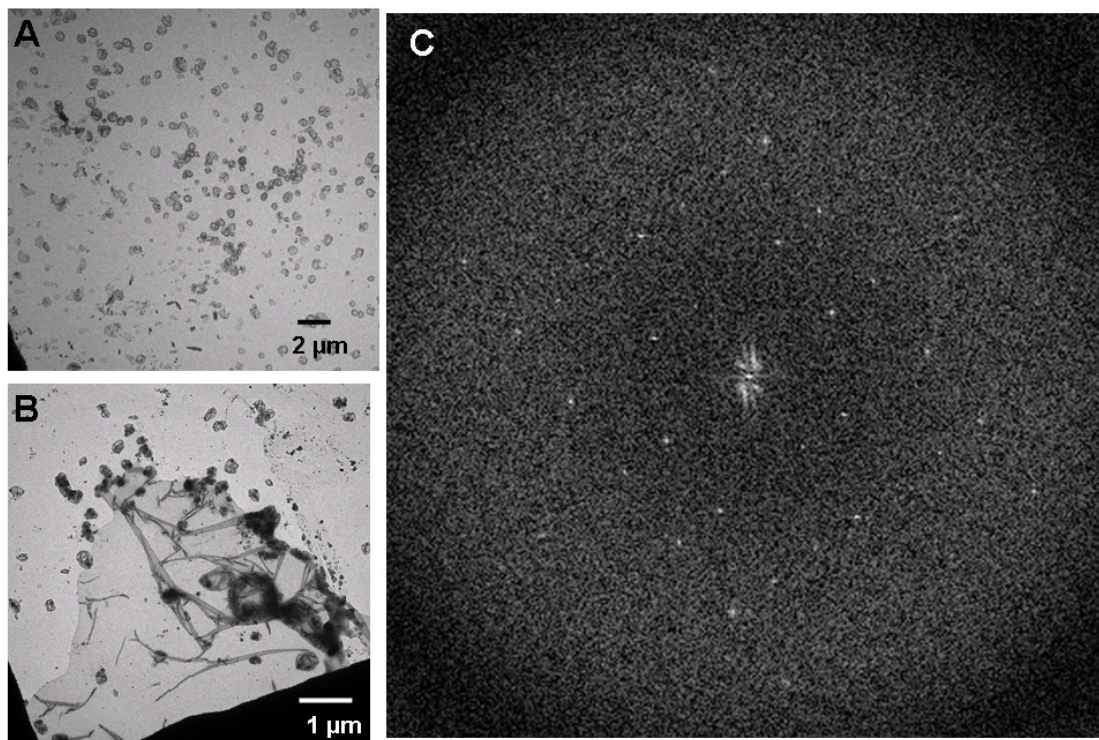
### **Temperature**

Temperature has been reported to be critical for crystallization due to its influence on rate of detergent removal. Using *C. glutamicum* lipids for crystallization restricted the usable temperature range. The pre-dialysis incubation was restricted between 15°C and room temperature; an incubation below 15°C led to protein aggregation during dialysis. The dialysis temperature was restricted to 30°C to allow a successful crystallization, while 25°C and 37°C led to protein aggregation. With the mixture of *E. coli* lipid extract/CL and synthetic PG 16:0-18:1, incubation temperatures between 4°C and room temperature led to successful crystal formation. Crystallization was also tolerant to dialysis temperature over a broad range of 30-37°C using the mixture of *E. coli* lipid extract/bovine CL and 25-30°C for PG 16:0-18:1.

### **3.2.2. Dialysis conditions**

About 250 conditions have been tested for 2D crystallization of BetPΔC45 by varying parameters known to be important for crystallization, including detergent, pH, monovalent salt, additives, divalent salt, temperature, hydrophobic absorption (Biobeads), and lipids. Many dialysis conditions resulted in formation of small BetPΔC45-reconstituted vesicles, which were not favorable for structure determination (Figure 14A). A “good” 2D crystal was evaluated by the size of the crystalline area (Figure 14B) and the diffraction quality, including resolution and reflection sharpness (Figure 14C).





**Figure 14.**

(A) After detergent removal, the protein was often reconstituted into small vesicles. These vesicles were less than 0.5 μm in diameter and not favorable for data collection, even though they showed diffraction in the Fourier-transformed image.

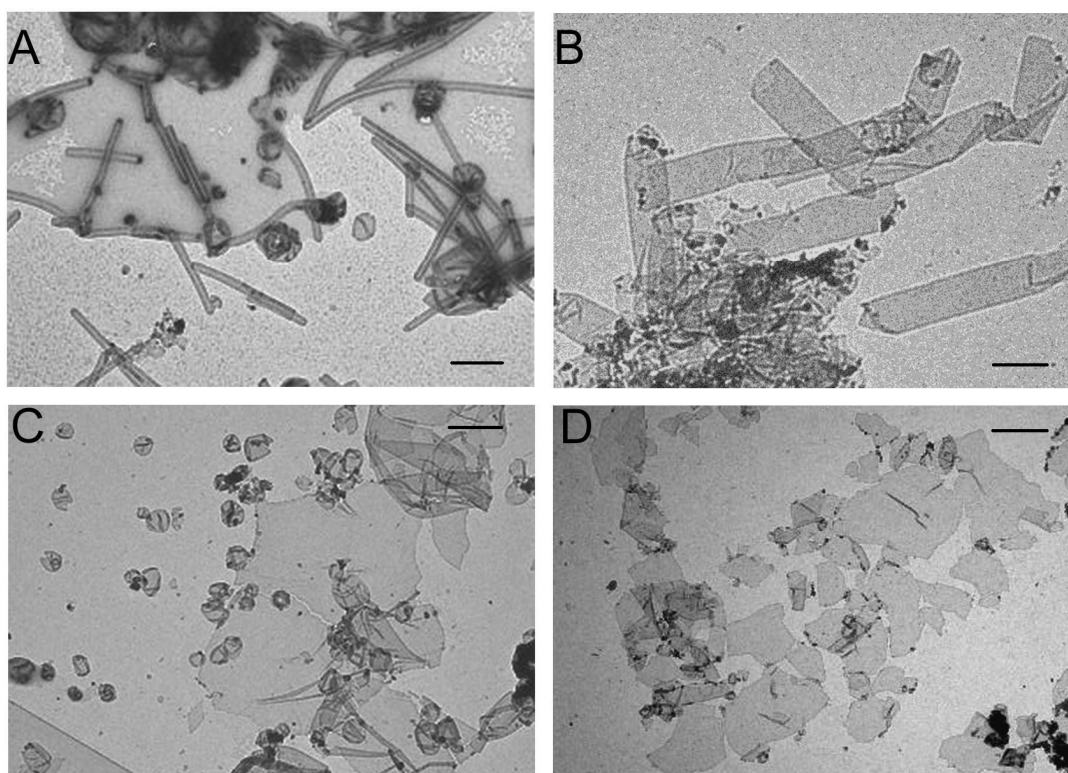
(B) A negatively stained crystal grown under optimized conditions.

(C) A Fourier-transformed image from a negatively stained crystal recorded on a CCD camera.

### **Monovalent salt**

The concentration of LiCl or KCl during dialysis influenced the crystal morphology of BetPΔC45. A dialysis buffer containing > 400 mM LiCl or KCl led to tubular of BetΔC45 crystals. Using the mixture of *E. coli* lipids/bovine CL (3:2, w/w) led to a formation of thinner tubes (~0.1 μm wide) than using *C. glutamicum* lipids (0.8 μm wide) (Figure 15A, B). In contrast to LiCl and KCl, a high concentration of NaCl (up to 1 M) did not facilitate the formation of tubular of BetPΔC45 crystals. Other than tubular crystals, large sheets or vesicular crystals were obtained at low salt conditions (< 300 mM) (Figure 15C, D). At intermediate concentrations of LiCl or KCl between 300 and 500 mM, the dialysate contained a mixture of tubes and sheets. Image processing of these crystals showed well-ordered crystalline areas in the tubes but not in sheets. A summary of the crystal morphology and dialysis conditions is listed below.

Monovalent Salt	Dialysis buffer containing >400 mM LiCl or KCl	Dialysis buffer containing <300 mM LiCl or KCl, or 100-500 mM NaCl
Lipid		
<i>E. coli</i> lipid extract/bovine CL (3:2, w/w)	Thin tubes (0.1 $\mu$ m wide, 2-4 $\mu$ m long)	Large sheets and vesicles up to 10 $\mu$ m
<i>C. glutamicum</i> lipid extract	Tubes (0.8 $\mu$ m wide, 3 $\mu$ m long)	Large sheets up to 5 $\mu$ m
PG 16:0-18:1	Not tested	Large round vesicles up to 3 $\mu$ m



**Figure 15. Overview of BetP $\Delta$ C45 crystals**

The crystals were negatively stained with 1 % uranyl acetate. The scale bar represents 1  $\mu$ m. (A) Tubes formed in the mixture of *E. coli* lipid extract/bovine cardiolipin at a ratio of 3:2 (w/w). (B) Tubes formed in *C. glutamicum* lipid extract. (C) Sheets and vesicles in *E. coli* lipid extract/bovine CL (3:2, w/w). (D) Sheets in *C. glutamicum* lipid extract. (A) and (B) were obtained from a buffer containing 500 mM LiCl. (C) and (D) were obtained from the standard dialysis buffer containing 200 mM NaCl.

#### Divalent salt:

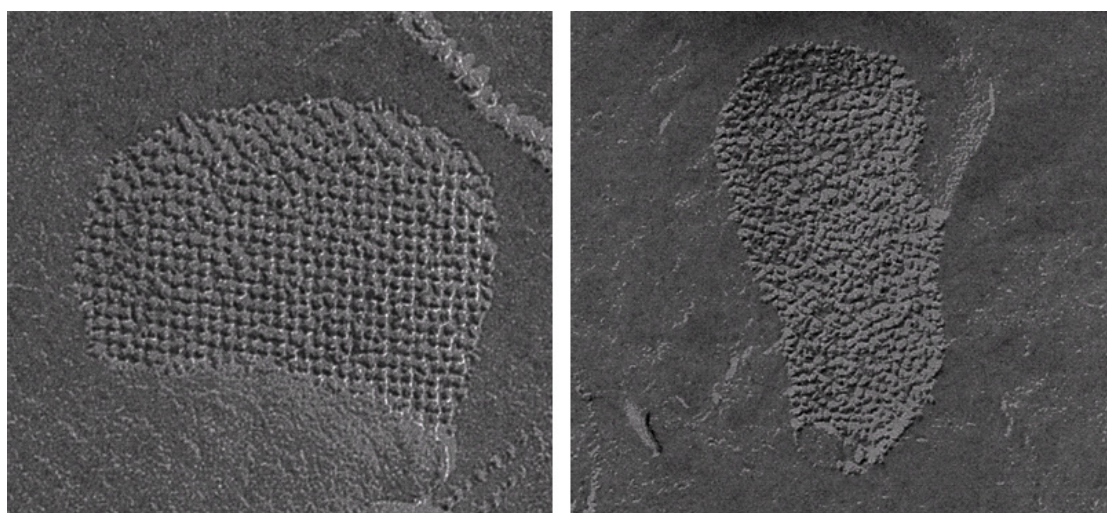
MgCl<sub>2</sub>, CoCl<sub>2</sub>, CuCl<sub>2</sub>, and Cd(OAc)<sub>2</sub> were tested as additives for 2D crystallization. BetP $\Delta$ C45 could be reconstituted into lipid bilayers without any divalent ion. During detergent removal by dialysis, the presence of salts of transition elements like CoCl<sub>2</sub>, CuCl<sub>2</sub> and Cd(OAc)<sub>2</sub> only led to protein aggregation. In contrast, the presence of CaCl<sub>2</sub> or MgCl<sub>2</sub> between 1 and 100

---

mM improved crystal quality as the crystalline areas grew larger (higher S/N during processing) and the crystal order became better (sharper diffraction spots showing lower mosaicity).

### **Substrate:**

Substrates such as glycine and glycine-betaine were found to be deteriorative for 2D crystal formation. BetP $\Delta$ C45 could still be reconstituted into lipid bilayers and form crystalline areas in the presence of 5 mM glycine-betaine. However, the crystal quality was dramatically reduced, as evident from weak, blurry reflections in the Fourier-transformed image. This was supported by freeze-fracture analysis, which showed that BetP $\Delta$ C45 molecules became randomly packed in the membrane in presence of glycine-betaine (Figure 16).



**Figure 16.** Freeze fracture of dialysates formed with and without 5 mM glycine-betaine during dialysis (prepared by F. Joos and Dr. W. Haase).

(Left) The crystal was obtained without glycine-betaine present during dialysis. (Right) The reconstituted proteoliposome obtained from a dialysis buffer containing 5 mM glycine-betaine.

### **pH, glycerol and MPD**

BetP $\Delta$ C45 was reconstituted into lipid bilayers at pH 4.0-9.0. The best-ordered 2D crystals were obtained at pH 7.5. The more the pH was shifted away from pH 7.5, the less-ordered the protein molecules became. An appropriate amount of glycerol and MPD increased the crystal size and enhanced crystal quality. The combination of 5% glycerol and 5% MPD was optimal for BetP $\Delta$ C45 crystallization. If glycerol or MPD was higher than 10 %,

---

the amount of protein aggregates increased, and the protein molecules became less ordered in the crystal membranes.

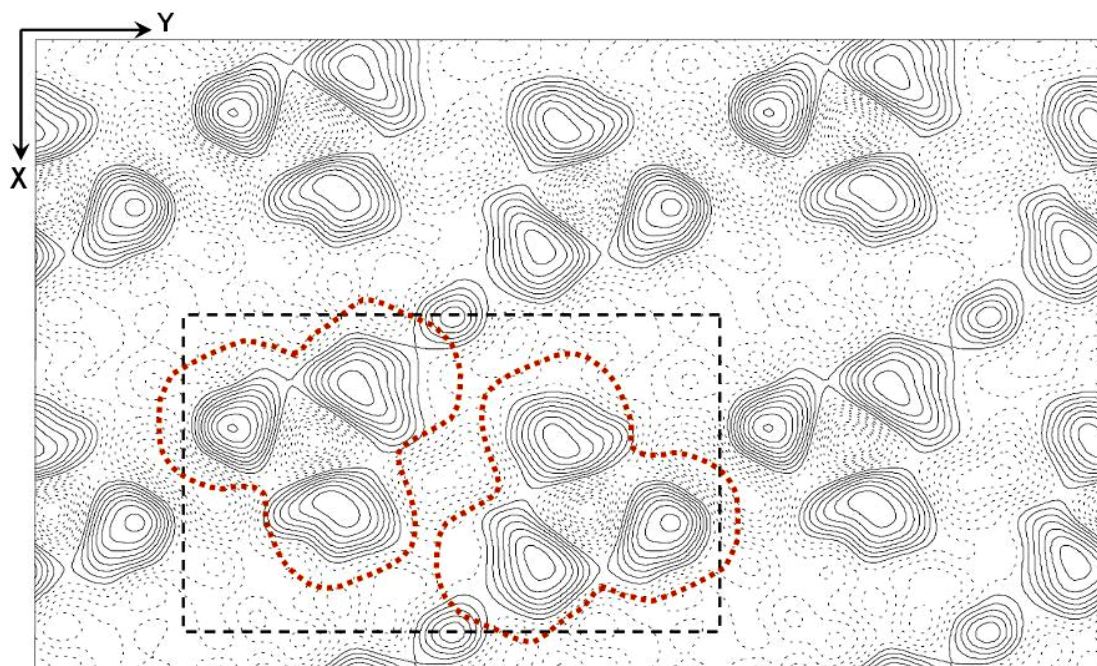
After optimizing all parameters, the dialysis buffer containing 50 mM pH 7.5 Tris-HCl, 200 mM NaCl, 5 % glycerol, 5 % MPD, 3 mM NaN<sub>3</sub>, and 4 mM CaCl<sub>2</sub> yielded the best crystals.

### **3.3. 2D crystals of BetP $\Delta$ C45 in *E. coli* lipids and bovine CL**

#### **3.3.1. Projection structure from a negatively stained crystal**

After detergent removal, the harvested 2D crystals were examined preliminarily by negative staining. A well-ordered crystal stained with 1% uranyl acetate normally showed 3-4 orders of reflections ( $\sim 25$  Å resolution) by optical diffraction. After image processing, the unit cell was determined to be  $a = 92.0(\pm 4)$  Å,  $b = 155.0(\pm 5)$  Å, and  $\gamma = 90.0(\pm 0.5)^\circ$ . In the projection density map, a single unit cell showed two sets of three densities with a hollow in the middle. The projection structure of the wild-type BetP showed that the protein is trimeric (Ziegler, Morbach et al. 2004). The projection map in negative stain thus indicates that BetP $\Delta$ C45 is also a trimer, and the unit cell contains two BetP $\Delta$ C45 trimers.





**Figure 17. Projection structure of a negatively-stained BetPΔC45 2D crystal.** The map was calculated to a resolution of 25 Å after 2 rounds of unbending and CTF correction. The black dashed line marks a single unit cell (88.3 Å × 149.9 Å, 90°). The red dotted lines represent BetPΔC45 trimers. Extra densities may be artifacts from staining.

### 3.3.2. Mirror-symmetric projection structure

Large sheet-like and vesicular crystals obtained from the standard dialysis condition were chosen for data collection (Figure 15C). The Fourier-transformed image showed strong reflections at Miller indices  $(h,k)$   $(\pm 1, \pm 3)$ ,  $(\pm 2, \pm 6)$ ,  $(\pm 3, \pm 3)$ ,  $(\pm 3, \pm 5)$  and  $(\pm 4, \pm 1)$ , which were manually selected to calculate the crystal unit cell with cell dimensions 90.3 Å × 152.0 Å,  $\gamma = 90^\circ$ . After image processing with three times unbending (CCUNBENDK), the IQ plot of the Fourier-transformed image showed reflections to a resolution of 8 Å (Figure 18). The reflections were used for map calculation.

The projection map showed a tight packing of BetPΔC45 molecules in the membrane (Figure 19). The boundary of each trimer was more difficult to define compared to the projection structure of the negatively-stained crystal. It was due to the tight packing of the protein molecules and the appearance of detailed structural features in cryo. Since a dominant intensity appeared in the centric region of the trimer (green dashed line in Figure 19), it was used as a marker to locate a trimer without mixing the monomers from adjacent

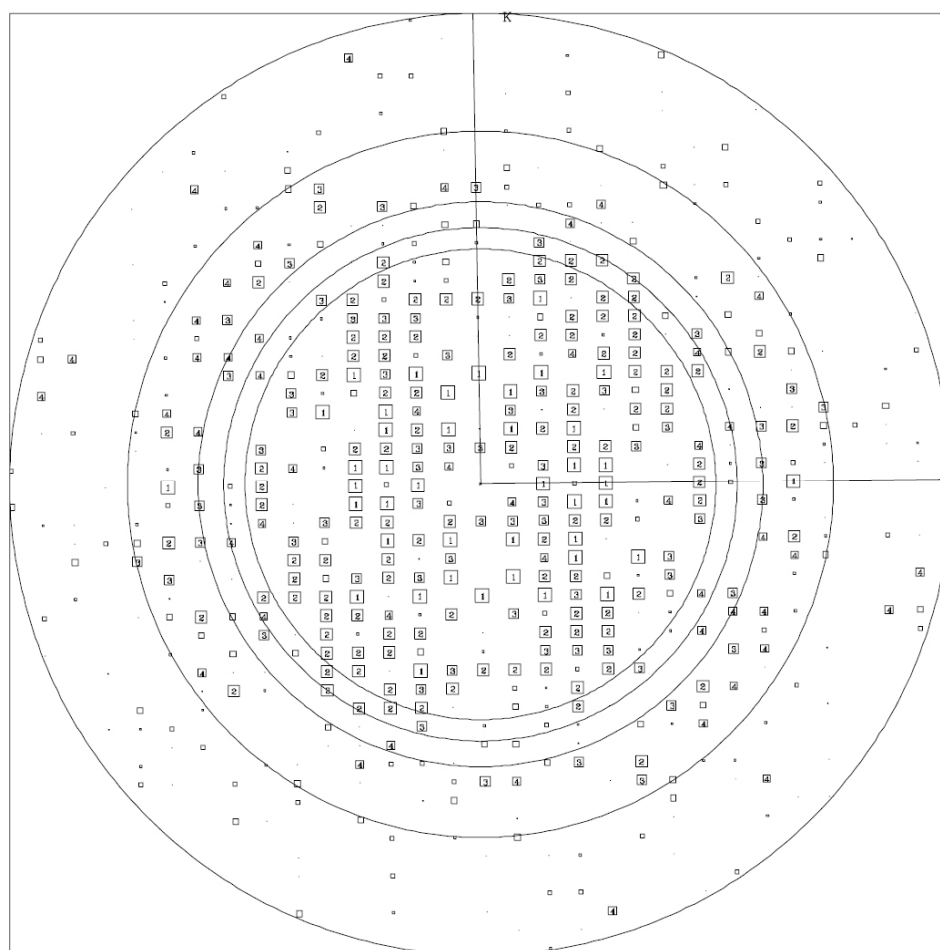
trimers. A mirror-symmetric plane (the XZ plane) was also recognized in the trimer density. To know the spatial relation between the two trimers in a single unit cell, ALLSPACE was used to evaluate the correlation of phases between specific reflections in the Fourier space. The suggested symmetries were p2, p12\_a, p12<sub>1</sub>\_b and p222<sub>1</sub>\_a (Table 4).

Plane group	Phase residual (90° random)	No. of comparison
p1	25.7	304
p2	29.2*	152
p12_b	74.3	102
p12_a	18.3*	103
p12 <sub>1</sub> _b	19.6*	102
p12 <sub>1</sub> _a	78.6	103
p222 <sub>1</sub> _a	23.2*	357
p22 <sub>1</sub> 2 <sub>1</sub>	62.5	357

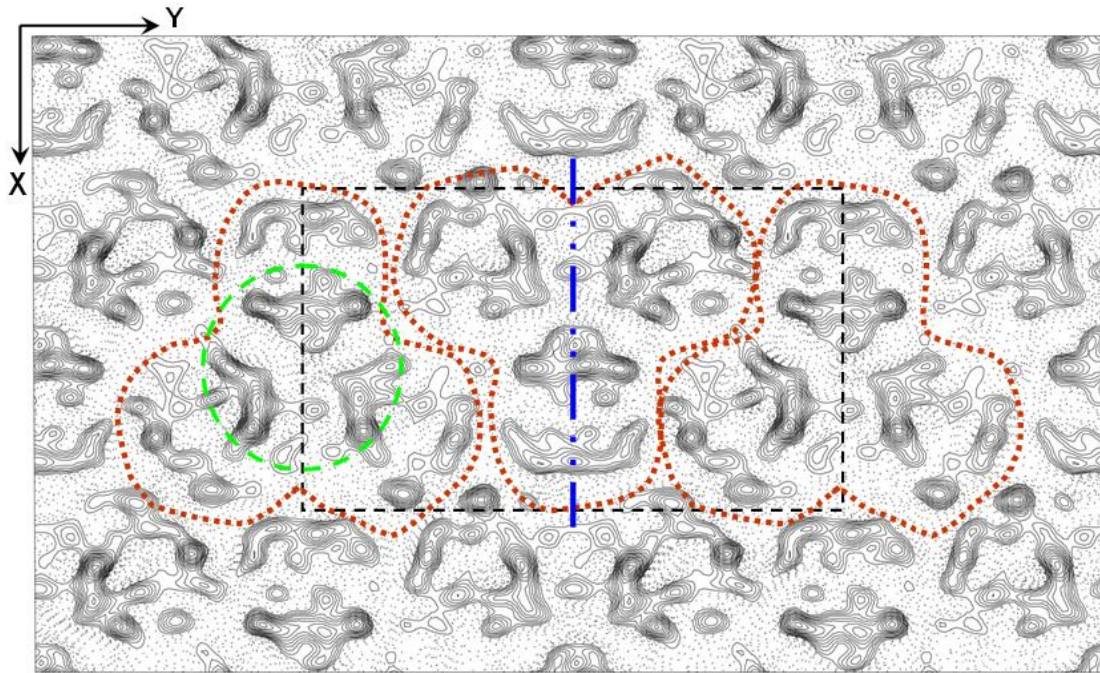
**Table 4. Statistics of plane group symmetry calculated by ALLSPACE**

The image was processed with the unit cell 90.3 Å × 152.0 Å, 90° applied. Reflections of IQ 1-5 up to 8 Å were used for symmetry calculation.

(\*) Acceptable



**Figure 18. IQ plot after 3 unbendings with unit cell 90.3 Å × 152.0 Å, 90° applied**  
The square size represents the spot intensity. The circles show 12, 11, 10, 8, 6 Å resolutions.



**Figure 19. A projection map of a sheet-like crystal in *E. coli* lipid extract/bovine CL (3:2, w/w)**

The projection map was calculated from the amplitudes and phases up to 8 Å. A B factor of  $-200 \text{ \AA}^2$  and p1 symmetry were applied. Dominant features are shown: a single unit cell of  $90.3 \text{ \AA} \times 152.0 \text{ \AA}$ ,  $90^\circ$  (black dashed line), the strong density in the center of a trimer (green dashed line), a single BetP $\Delta$ C45 trimer (red dotted lines), and the mirror plane (the XZ plane) (blue dashed line).

In the case of a rectangular unit cell containing two trimers, the spatial relation between the two molecules can only be described by either p2 or p12<sub>1</sub>\_b, while p222<sub>1</sub>\_a was suitable for four asymmetric units, and p12\_a described two stacking membranes but not the relation between these two adjacent trimers in the crystal plane. Combined with the mirror symmetry in the trimer density, the result from ALLSPACE implied that image processing led to averaging the trimer densities from two trimers facing different sides of the membrane: one “up” and one “down”. To deconvolute the averaged density, it would be necessary to apply an expanded unit cell during image processing.

### 3.3.3. Deconvolution by expanding the unit cell

Different expanded unit cells in either or both directions were applied to deconvolute the averaged density. From the published projection structure of BetP wild type, the crystals were processed with a bigger unit cell ( $a = 180.6$

Å,  $b = 152.0$  Å,  $\gamma = 90^\circ$ ). It led to a single unit cell containing four BetPΔC45 trimers with the plane group symmetry  $p22_12_1$  (Ziegler, Morbach et al. 2004).

Firstly, the unit cell was expanded in the X direction to  $180.6$  Å  $\times$   $152.0$  Å,  $\gamma = 90^\circ$ , even though the reflections of the odd orders ( $h = 2n+1$ ) were not observed in the calculated Fourier-transformed image or in the optical diffraction. After image processing, the averaged intensity of the even orders along  $h$  ( $h = 2n$ ) in the Fourier space was 27-fold stronger than that of the odd orders along  $h$  ( $h = 2n+1$ ), showing that the reflections at  $h = 2n+1$  were absent and contained no information. Thus, no additional significant reflections were extracted by expanding the unit cell (Figure 20). The projection structure after expanding the unit cell showed the same features as described in 3.3.2. (Figure 21). The mirror-symmetric plane did not disappear upon expanding the unit cell. Plane group symmetry calculations by ALLSPACE suggested even more possibilities (Table 5). Consequently, image processing from expanding the unit cell in X dimension did not deconvolute the mirror-symmetric trimer density, and no additional information at  $h = 2n+1$  could be extracted from the Fourier transform.

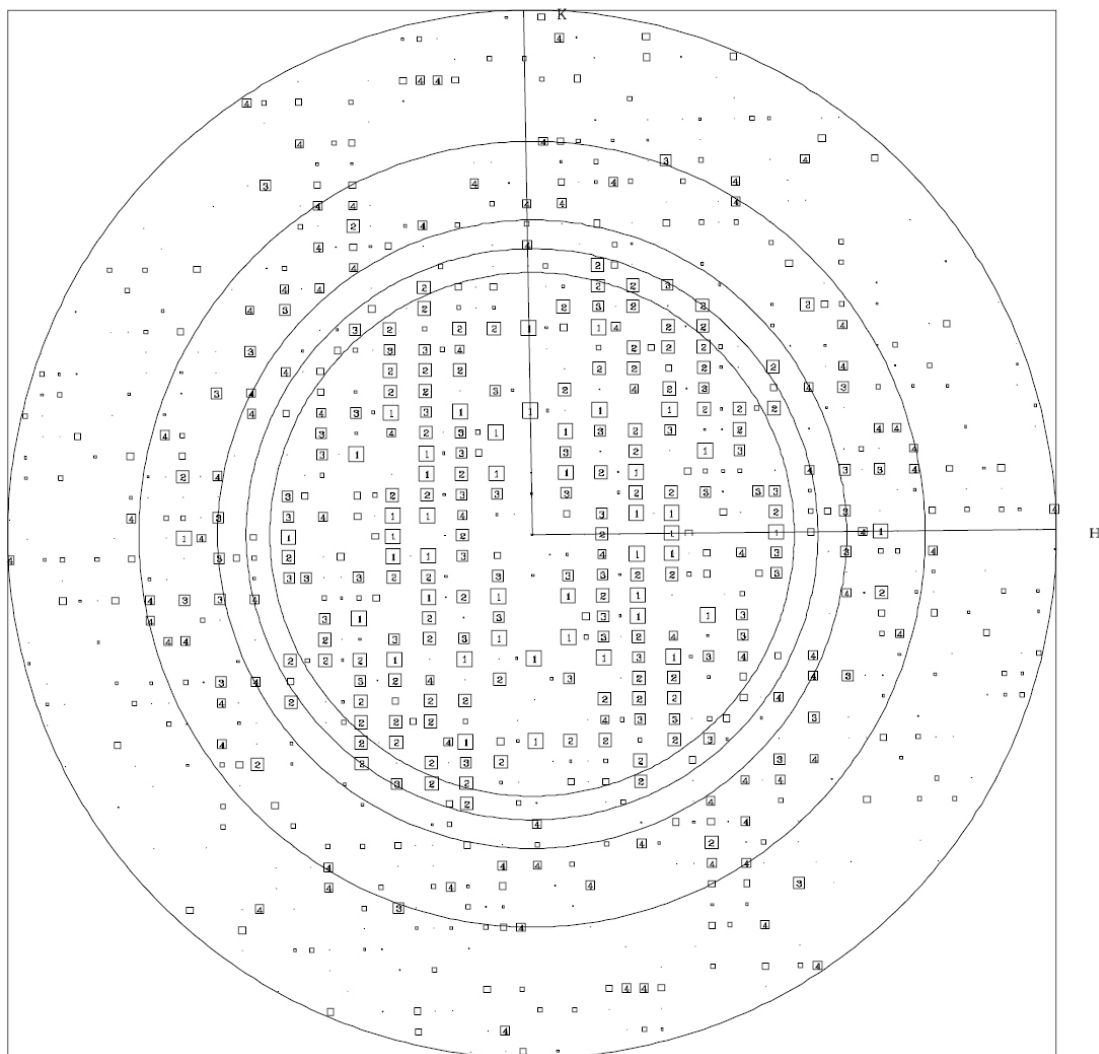
Plane group	Phase residual (90° random)	No. of comparison
p1	28.3	336
p2	35.4*	168
p12_b	75.2	107
p12_a	18.5*	104
p12 <sub>1</sub> _b	22.4*	107
p12 <sub>1</sub> _a	20.0*	104
p222 <sub>1</sub> _a	26.9*	379
p22 <sub>1</sub> 2 <sub>1</sub>	27.5*	379

**Table 5. Statistics of plane group symmetry calculated by ALLSPACE**

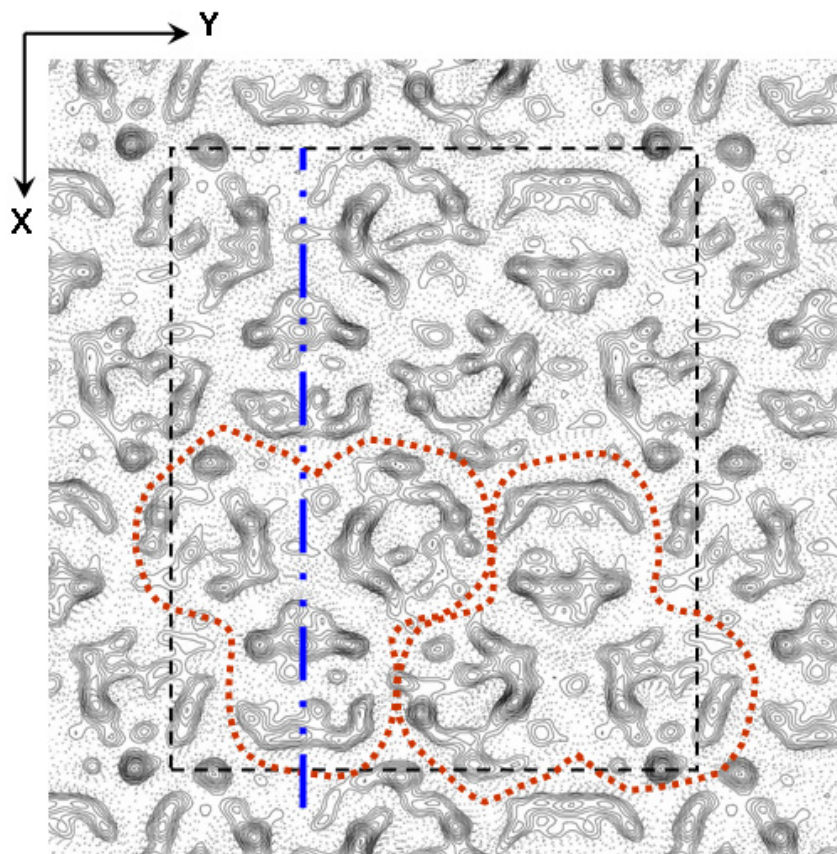
The image was processed with the unit cell  $180.6$  Å  $\times$   $152.0$  Å,  $90^\circ$  applied. Reflections of IQ 1-5 up to  $8$  Å were used for symmetry calculation.

(\*) Acceptable space group suggested based on the statistics.





**Figure 20. IQ plot after 3 unbendings with unit cell  $180.6 \text{ \AA} \times 152.0 \text{ \AA}$ ,  $90^\circ$  applied**  
 A bigger square size represents a stronger spot and its lower IQ value. The circles show the resolutions of 12, 11, 10, 8, 6 Å.



**Figure 21.** A projection map at 8 Å applied with a unit cell of 180.6 Å × 152.0 Å, 90°. A B factor of -200 Å<sup>2</sup> and p1 symmetry were applied. Major features are shown: a single unit cell (black dashed line), marked a BetPΔC45 trimer (red dotted lines), and the mirror plane (blue dashed line)

Image processing with the Y dimension expanded gave a similar result as described above. About 1000 images of these frozen-hydrated BetPΔC45 crystals were collected, and ~100 images among them were processed. Processing of the images except for two (see 3.3.4.) showed similar unit cell dimensions with many recommended plane group symmetries and a mirror-symmetric projection structure. Due to this undeconvolutable situation, a sample preparation with one freeze-thaw cycle (-180°C to 45°C) was applied to dialysates. However, this procedure did not help to rearrange molecular packing in the crystal membrane.

### 3.3.4. A very rare case: p22<sub>1</sub>2<sub>1</sub> crystals

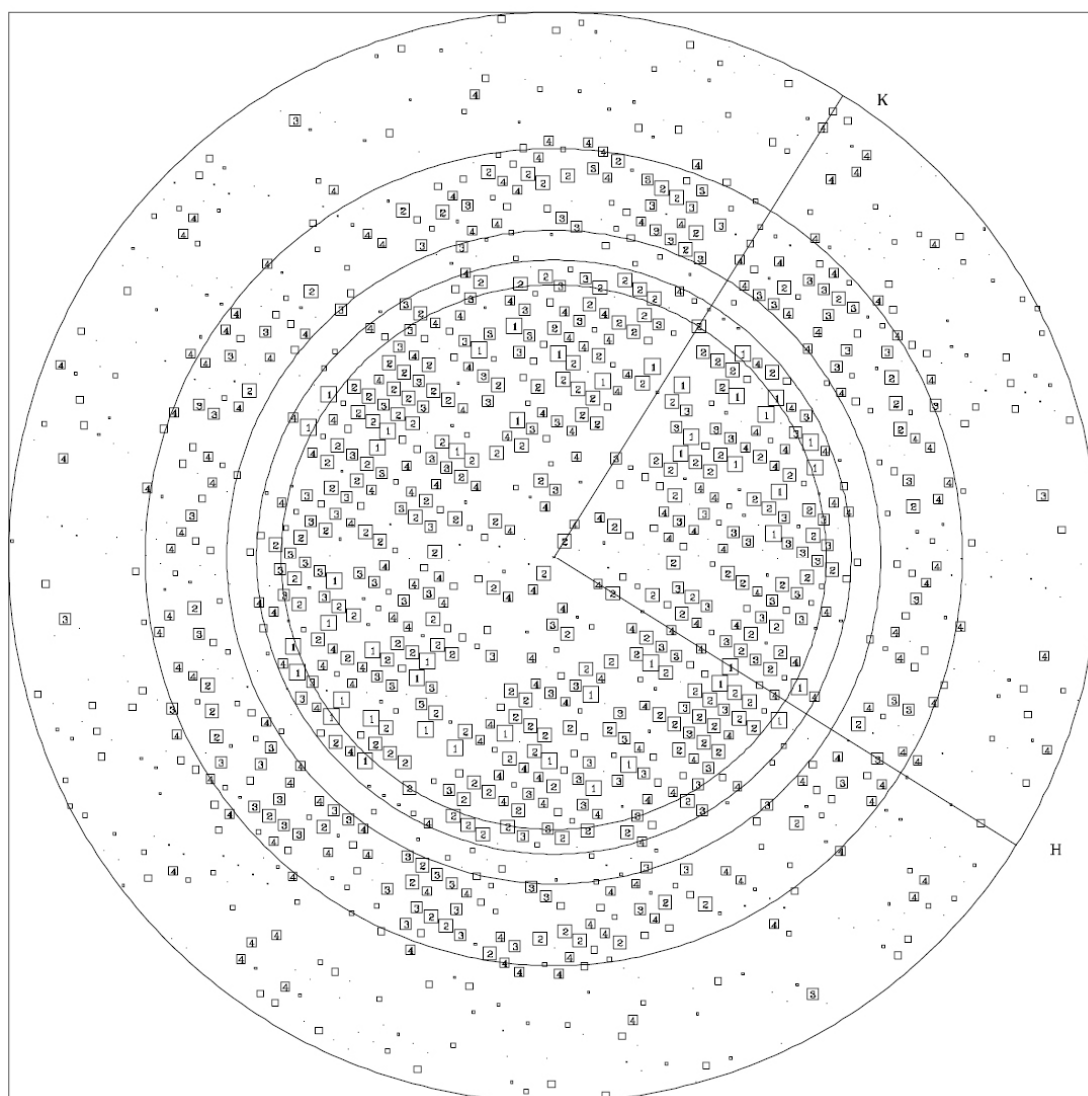
Among these 100 processed images, only two could be classified as p22<sub>1</sub>2<sub>1</sub>. These crystals had slightly larger unit cell dimensions in both X and Y ( $a = 186.3 \pm 2.3$  Å,  $b = 167.5 \pm 0.4$  Å,  $\gamma = 90.0 \pm 0.3^\circ$ ), and diffracted better, with

structural information to 6.5 Å after image processing (Figure 22).

Plane group	Phase residual (90° random)	No. of comparison
p1	28.3	336
p2	35.4*	168
p12_b	75.2	107
p12_a	18.5*	104
p12 <sub>1</sub> _b	22.4*	107
p12 <sub>1</sub> _a	20.0*	104
p222 <sub>1</sub> _a	26.9*	379
p22 <sub>1</sub> 2 <sub>1</sub>	27.5*	379

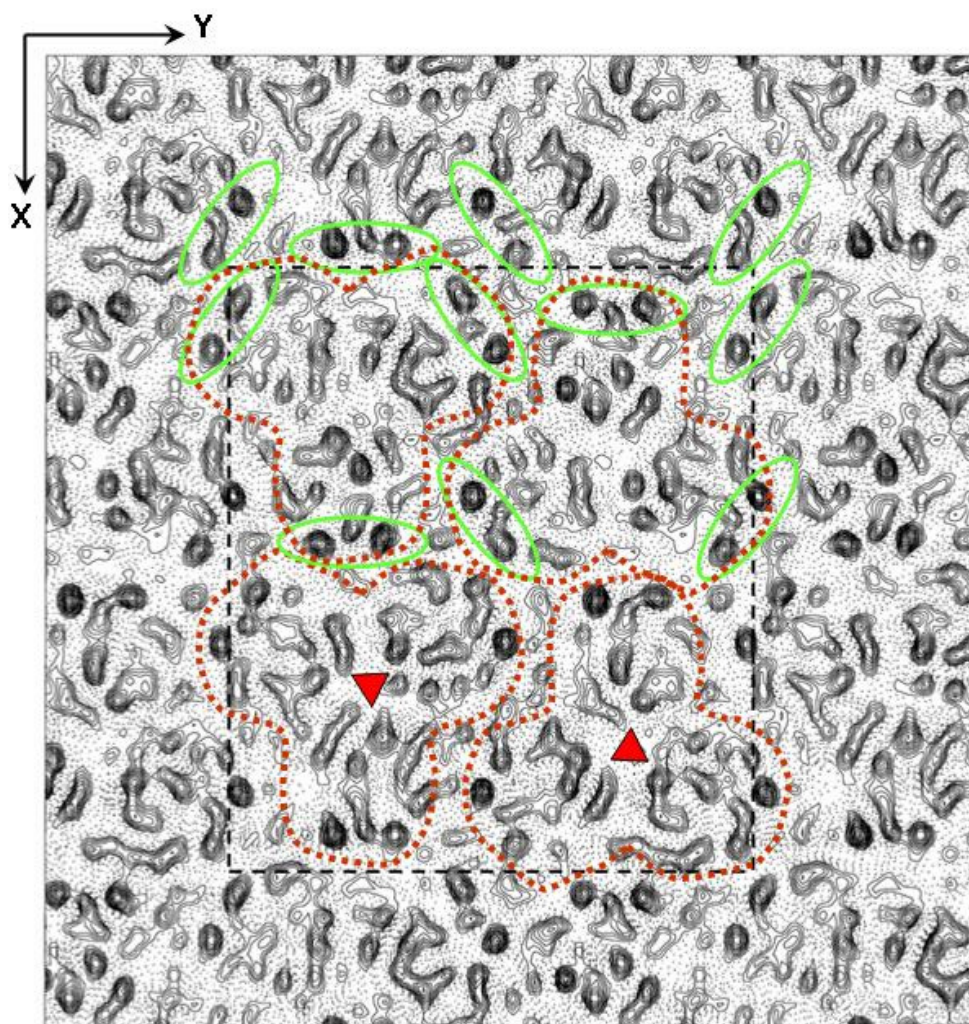
**Table 6. Statistics of plane group symmetry calculated by ALLSPACE**

The image was processed with the unit cell 188.6 Å × 167.8 Å applied. Reflections of IQ 1-5 up to 7 Å were used for symmetry calculation.  
 (\*) Acceptable space group suggested based on the statistics;



**Figure 22. IQ plot after 3 unbendings with unit cell 188.6 Å × 167.8 Å, 90° applied**  
 A bigger square size represents a stronger spot and its lower IQ value. The circles show the resolutions of 12, 11, 10, 8, 6 Å.

The projection structure at 7 Å showed 4 BetPΔC45 trimers in a unit cell (Figure 23). The density on the interface between two adjacent trimers was more intense than the density in the center of a trimer. These strong densities indicated interactions between two adjacent BetPΔC45 trimers, even though the unit cell was slightly bigger than the projection structures described in the previous sections (3.3.2., 3.3.3.). No mirror-symmetry was found in this projection structure, and a pseudo threefold symmetry was recognized in the center of the trimer density. The suggested plane groups were p2, p12<sub>1</sub>\_a, p12<sub>1</sub>\_b, and p22<sub>1</sub>2<sub>1</sub> (Table 6). Since four trimers occupied a single unit cell, only the plane group p22<sub>1</sub>2<sub>1</sub> was suitable, while p2, p12<sub>1</sub>\_a and p12<sub>1</sub>\_b described the spatial relation for two asymmetric units only.



**Figure 23.** A non-symmetrized projection map a p22<sub>1</sub>2<sub>1</sub> crystal at 7 Å. A B factor of -200 Å<sup>2</sup> was applied. Several features are shown: a single unit cell (188.6 Å × 167.8 Å) (black dashed line), BetPΔC45 trimers (red dotted lines), pseudo 3-fold symmetry (red triangles), and strong densities at the interface to adjacent trimers (green lines).

Two crystal lattices were processed and merged, meaning that the phases and amplitudes from the two lattices were averaged for each reflection. With symmetry applied during merging, the correlating reflections were averaged, significantly improving the S/N ratio. In real space, it averaged the densities of all four trimers. To determine the unit cell as accurately as possible, the unit cell dimensions were averaged from both lattices, giving  $a = 186.3 \text{ \AA}$ ,  $b = 167.5 \text{ \AA}$ , and  $\gamma = 90^\circ$ . Merging was evaluated by the phase residuals. The lower the phase residual, the higher the accuracy of the merging procedure. After merging these two lattices, the phase residuals at different resolution shells showed reasonable values up to  $6.5 \text{ \AA}$  (Table 7). A phase residual of  $45^\circ$  shows that the reflection is merged randomly.

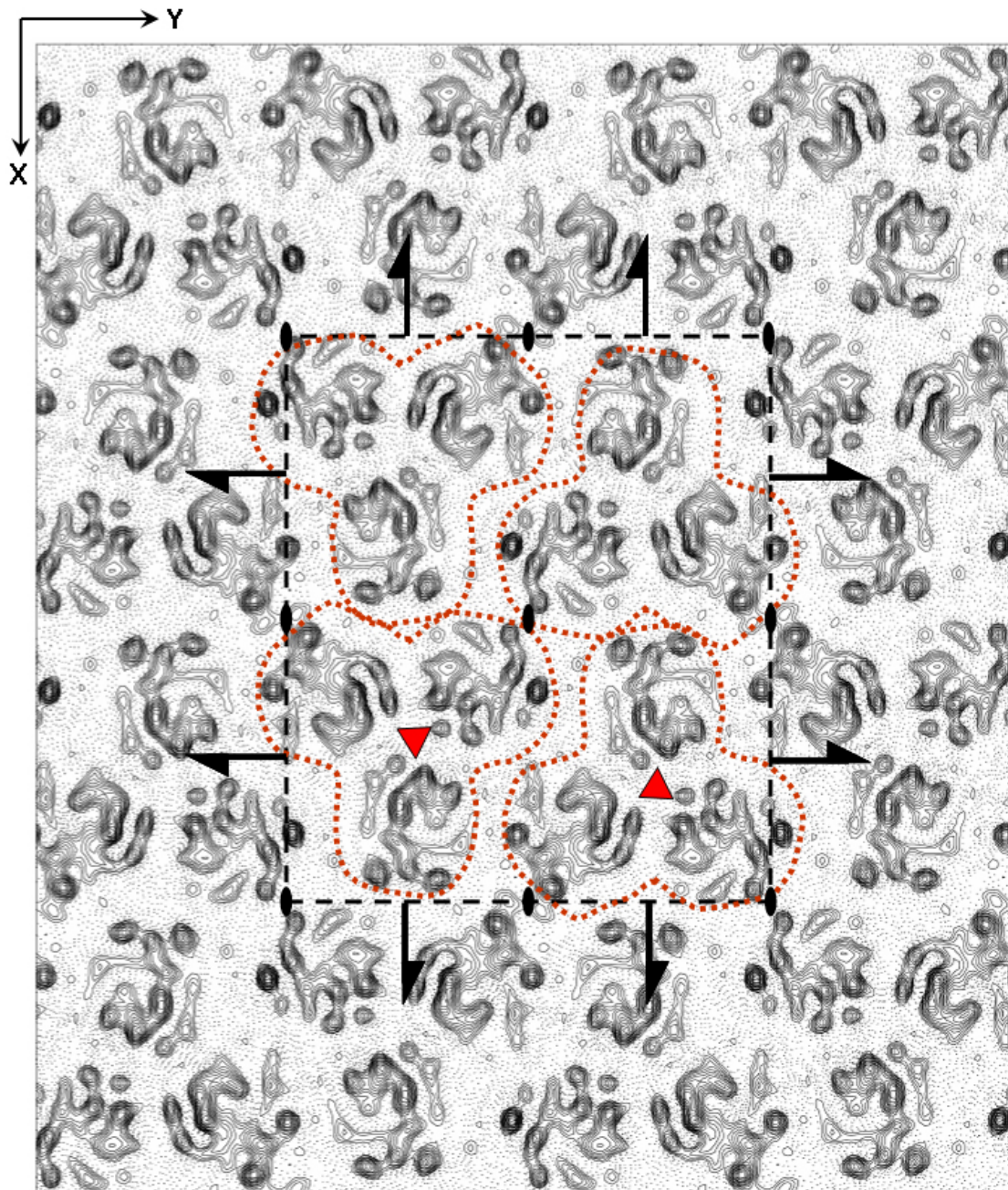
Resolution (Å)	No. of reflections	Averaged phase residual (°)
180 – 20.9	45	21.4
14.6	52	17.2
11.9	52	13.2
10.3	42	20.5
9.2	42	23.9
8.4	47	30.0
7.8	45	22.7
7.3	38	29.3
6.9	27	34.4
6.5	33	40.8

**Table 7. Merging statistics of the phase residuals**

Statistics from merging two lattices with  $p22_12_1$  applied. The averaged phase error at different resolution shells were calculated up to  $6.5 \text{ \AA}$ . The phase error of  $45^\circ$  indicated random.

Compared to the non-symmetrized projection structure from a single lattice, the merged projection structure became clearer and stronger (Figure 24). In the projection map, half of the trimers were “up” and the other half were “down”. An “up” trimer was surrounded by two “down” trimers along the X direction (screw axis X), two “down” along the Y direction (screw axis Y), and four “up” along the diagonals (2-fold axis along Z, which is perpendicular to the membrane).





**Figure 24. A merged, p22,21-symmetrized projection map from two lattices**

A projection map was calculated to 7 Å with a B factor of  $-250 \text{ \AA}^2$  applied. A single unit cell is shown with its symmetry elements: 2-fold axes perpendicular to the membrane (black ovals), screw axes in the plane of the membrane (half arrows), BetPΔC45 trimer density (red dotted lines), and pseudo 3-fold symmetry perpendicular to the membrane (red triangles).

### 3.4. 2D crystals of BetPΔC45 in *C. glutamicum* lipids

The negatively stained sheet-like and tubular crystals in the *C. glutamicum* lipid extract showed the same features as in the projection structure of the crystals in *E. coli* lipid extract/bovine CL: two trimers in a unit

cell (Figure 17). A single unit cell consisted of two BetPΔC45 trimer molecules in the rectangular dimensions of 92.1 (±1.6) Å × 155.2 (±2.3) Å, which was identical to the crystals in *E. coli* lipid extract/bovine CL mixture.

### 3.4.1. Projection structure of sheet-like crystals

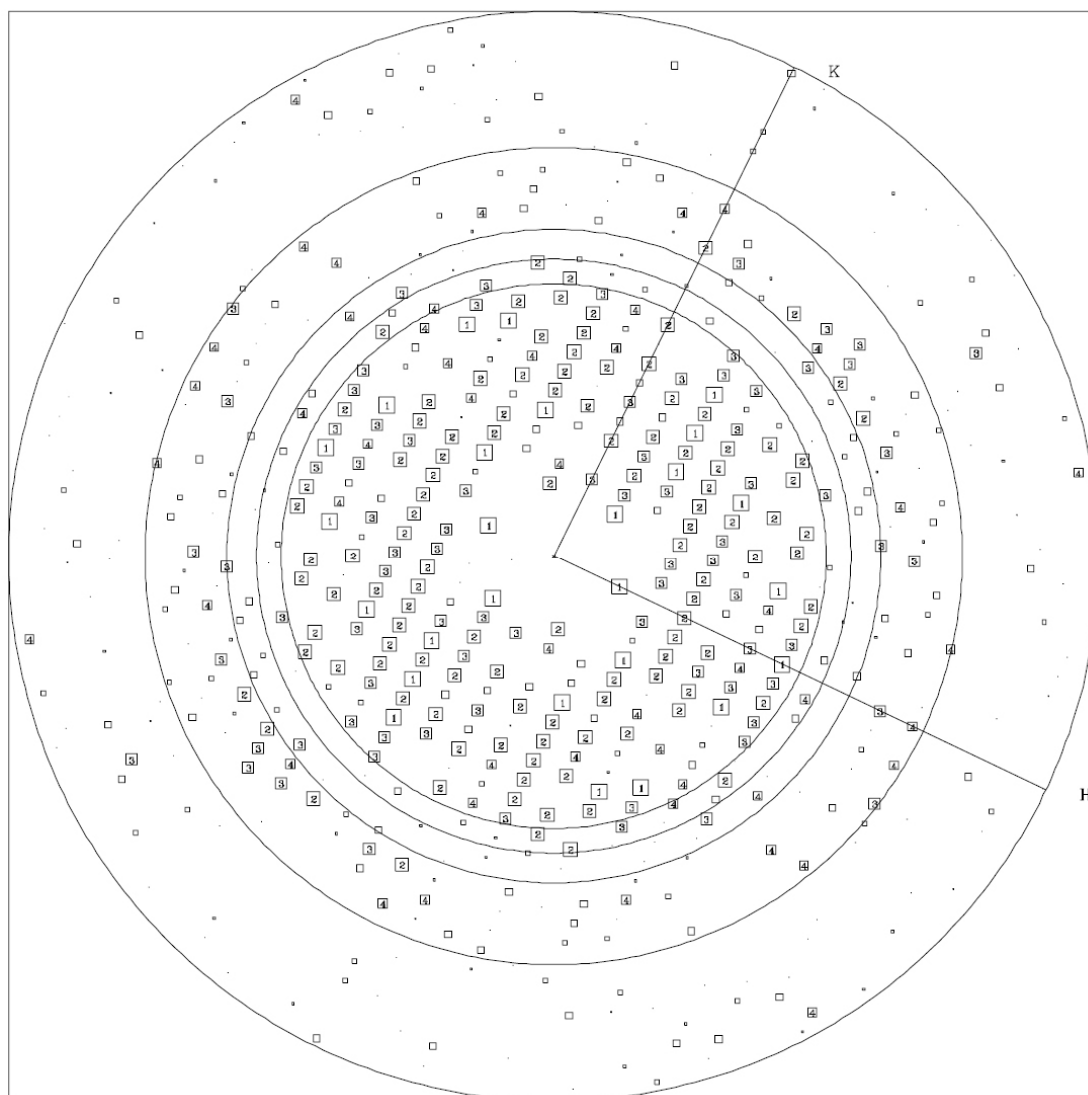
Preparation of frozen-hydrated sheet-like crystals was confined to 10% glucose as embedding medium and low humidity in order to observe diffractions in the Fourier-transformed image. The Fourier-transformed image showed strong reflections at the same Miller indices ( $h,k$ ) ( $\pm 1, \pm 3$ ), ( $\pm 2, \pm 6$ ), ( $\pm 3, \pm 3$ ), ( $\pm 3, \pm 5$ ) and ( $\pm 4, \pm 1$ ) (Figure 25) similar to the crystals in *E. coli* lipids/bovine CL mixture (Figure 18). After three times unbending and CTF correction, the crystals had structural information to 8 Å (Figure 25). The calculation of plane group symmetry by ALLSPACE showed only one possible symmetry p12<sub>1</sub>\_b (Table 8).

Plane group	Phase residual (90° random)	No. of comparison
p1	28.3	326
p2	77.6	163
p12_b	75.5	108
p12_a	73.0	111
p12 <sub>1</sub> _b	25.7*	108
p12 <sub>1</sub> _a	75.2	111
p222 <sub>1</sub> _a	62.5	382
p22 <sub>1</sub> 2 <sub>1</sub>	63.7	382

**Table 8. Statistics of plane group symmetry calculated by ALLSPACE**

The image was processed with the unit cell 90.5 Å × 152.1 Å applied. Reflections of IQ 1-5 up to 8 Å were used for symmetry calculation.

(\*) Acceptable space group suggested based on the statistics

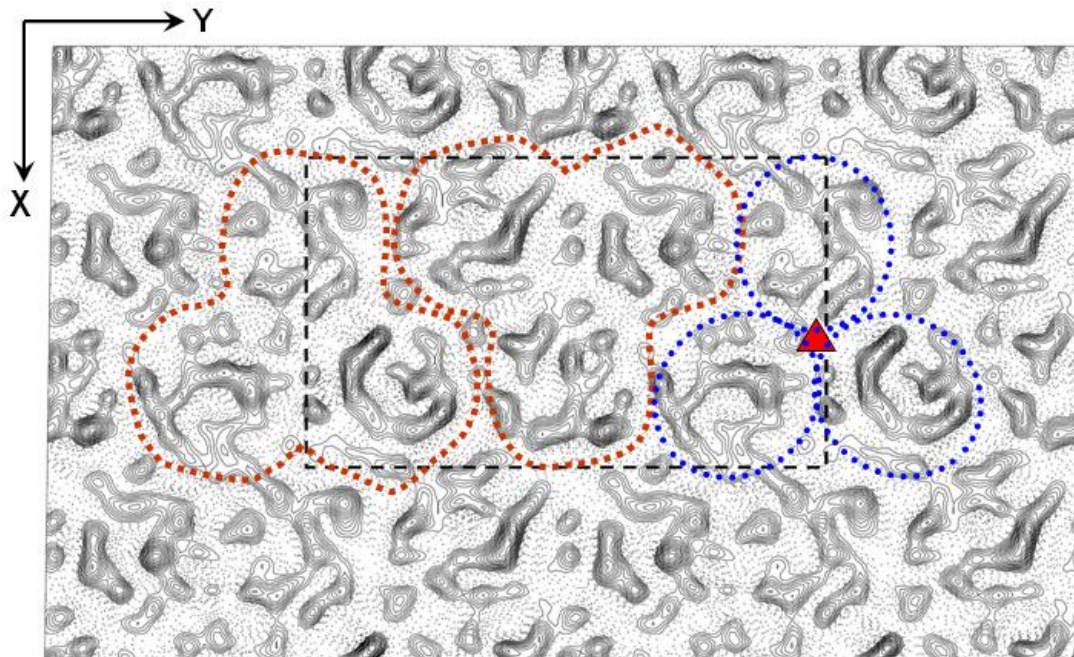


**Figure 25.** IQ plot after 3 unbendings processed with unit cell  $90.5 \text{ \AA} \times 152.1 \text{ \AA}$ ,  $90.8^\circ$  applied.

A bigger square box represents a stronger spot and its lower IQ value. The circles show the resolutions of 12, 11, 10, 8, 6 Å.

The projection density map showed tight packing of BetPΔC45 trimers (Figure 26), which was similar to the projection maps from the crystals in *E. coli* lipids/bovine CL (Figure 19). In this lipid, BetPΔC45 lattices showed  $p12_1_b$  symmetry with a screw axis along the Y direction with one trimer facing up and one down in a single unit cell. Noticeably, the trimer density did not show any mirror symmetry but only pseudo threefold symmetry. This indicates that the projection density was no longer averaged from more than one trimer. Therefore, these crystals did not require any deconvolution.





**Figure 26.** A non-symmetrized projection density map of a sheet crystal in *C. glutamicum* lipids.

The projection maps were calculated to a resolution of 8 Å with a B factor of  $-200 \text{ \AA}^2$  applied. Special features are shown: a single unit cell (black dashed line), BetPΔC45 trimers (red dotted lines), BetPΔC45 monomers (blue dotted ovals), and the center of BetPΔC45 trimer (red triangle).

### 3.4.2. Projection structure of tubular crystals

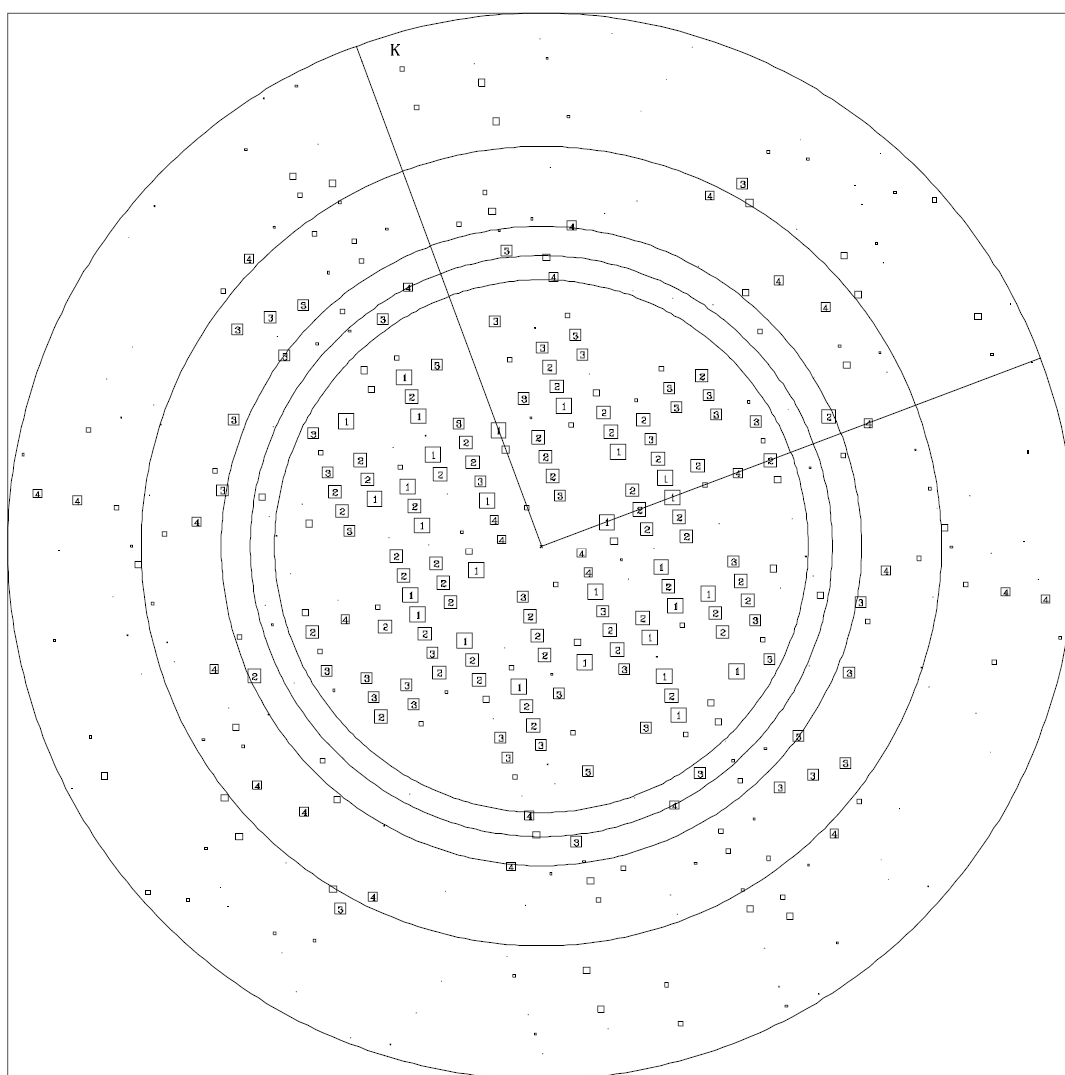
The tubular crystals in *C. glutamicum* lipids were  $\sim 0.8 \mu\text{m}$  wide. Using 5-20% trehalose or glucose as cryoprotectant, no reflections were observed. Successful freezing was achieved by using 0.5 % tannin-NaOH (pH 6.5). As it is common for tubular crystals, two lattices from the two layers of the tube were observed in the Fourier-transformed image. As both lattices had a relative angle of  $85.32(\pm 2.34)^\circ$  to each other, they could be processed individually. However, they showed spots only to 9-12 Å (Figure 27)

Tubular crystals were packed similarly as the sheet-like crystals with a unit cell of  $91.6 \text{ \AA} \times 154.8 \text{ \AA}$ ,  $90^\circ$  and  $p12_1_b$  symmetry (Table 9). In agreement with this, the projection map showed the same packing for tubular and sheet-like crystals (Figure 28). Because of the lower resolution, the structural details were not as clear as in the sheet-like crystals.

Plane group	Phase residual (90° random)	No. of comparison
p1	25.2	172
p2	58.0	86
p12_b	73.8	42
p12_a	33.1'	38
p12 <sub>1</sub> _b	27.8*	42
p12 <sub>1</sub> _a	60.6	38
p222 <sub>1</sub> _a	45.4	166
p22 <sub>1</sub> 2 <sub>1</sub>	61.2	166

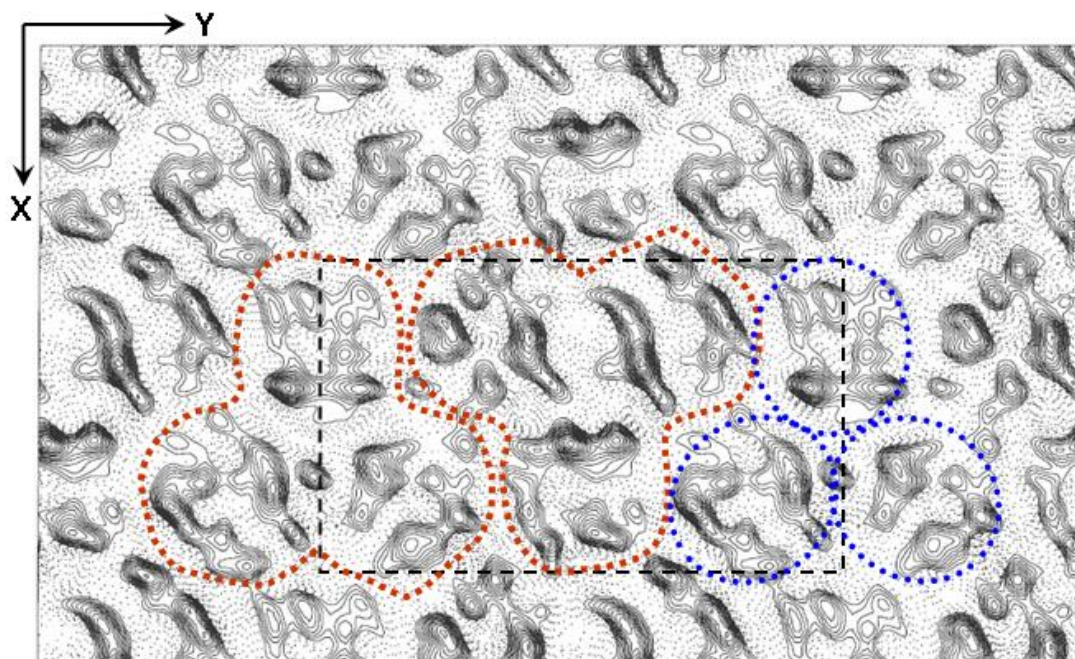
**Table 9. Statistics of plane group symmetry calculated by ALLSPACE**

The image was processed with the unit cell 91.6 Å × 154.8 Å applied. Reflections of IQ 1-5 up to 8 Å were used for symmetry calculation. Space group suggested based on the statistics:  
 (!) Should be considered;  
 (\*) Possible.



**Figure 27. IQ plot after 3 unbendings**

A bigger square size represents a stronger spot and its lower IQ value. The circles show the resolutions of 12, 11, 10, 8, 6 Å.



**Figure 28.** A non-symmetrized projection density map of a tubular crystal in *C. glutamicum* lipids.

The projection map was calculated to a resolution of 9 Å after three times unbending and CTF correction with a B factor of  $-200 \text{ \AA}^2$  applied. Features are shown: a single unit cell (black dashed line), BetPΔC45 trimers (red dotted lines), and BetPΔC45 monomers (blue dotted ovals).

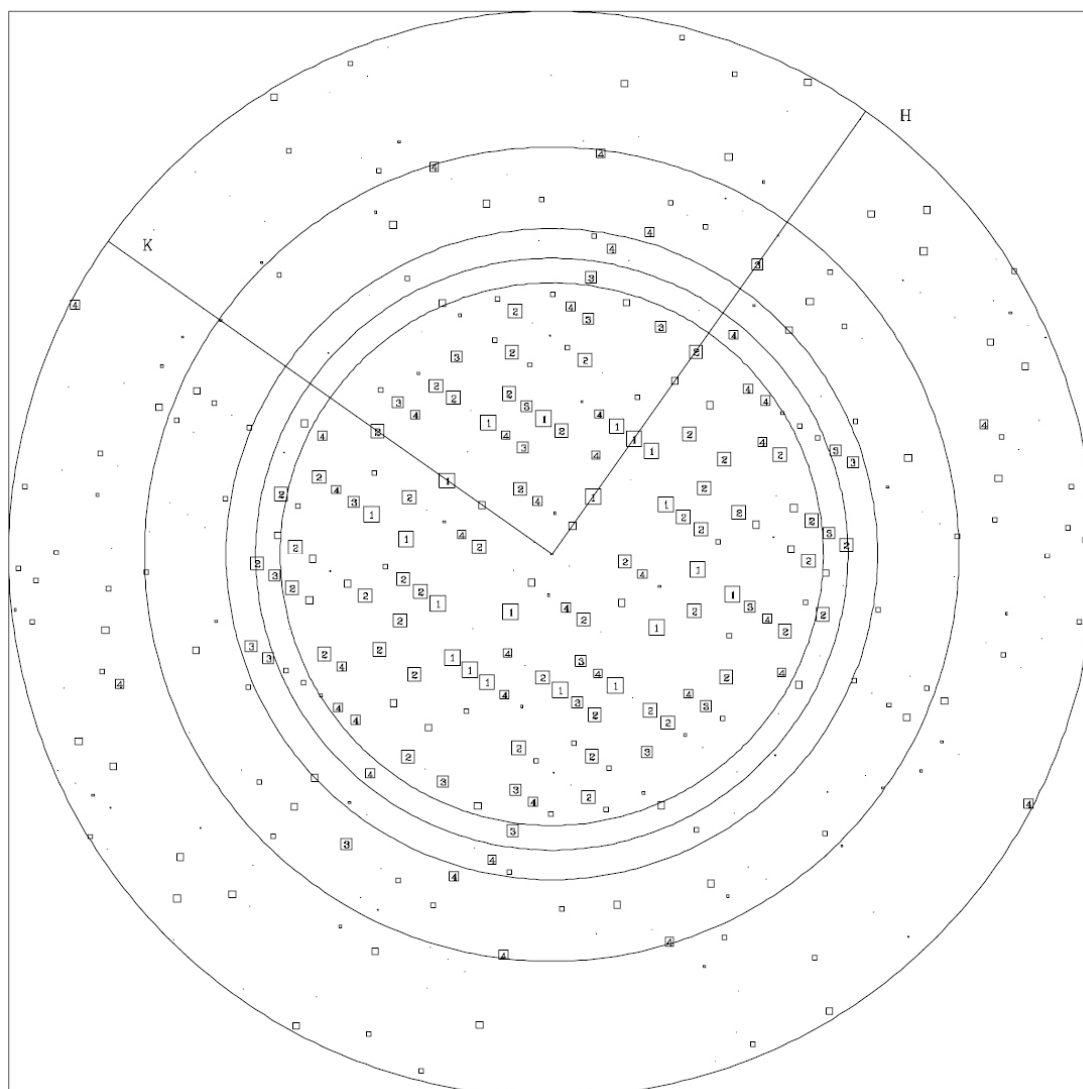
### 3.5. Projection structure of BetPΔC45 in PG 16:0-18:1

BetPΔC45 crystals grown in synthetic PG 16:0-18:1 predominantly formed sheets and large vesicles up to 3 μm with standard dialysis buffer. Cryo embedding of the crystals with 10% glucose resulted in good preservation of crystals as observed by contrasty diffractions in the Fourier-transformed image. The strongest reflections appeared at the same positions similar to the crystals grown in *C. glutamicum* lipids and in *E. coli* lipids/CL, but these reflections were less sharp and intense (Figure 29). It implies that protein molecules in these crystals were less ordered, resulting in loss of resolution.

Plane group	Phase residual (90° random)	No. of comparison
p1	28.9	160
p2	54.3'	80
p12_b	68.0	36
p12_a	36.1'	33
p12 <sub>1</sub> _b	31.9*	36
p12 <sub>1</sub> _a	57.0	33
p222 <sub>1</sub> _a	45.4'	149
p22 <sub>1</sub> 2 <sub>1</sub>	62.3	149

**Table 10. Statistics of plane group symmetry calculated by ALLSPACE**

The image was processed with the unit cell 91.6 Å × 152.7 Å applied. Reflections of IQ 1-5 up to 8 Å were used for symmetry calculation.  
 (\*) Acceptable space group suggested based on the statistics  
 (!) Should be considered;  
 (') Possible.

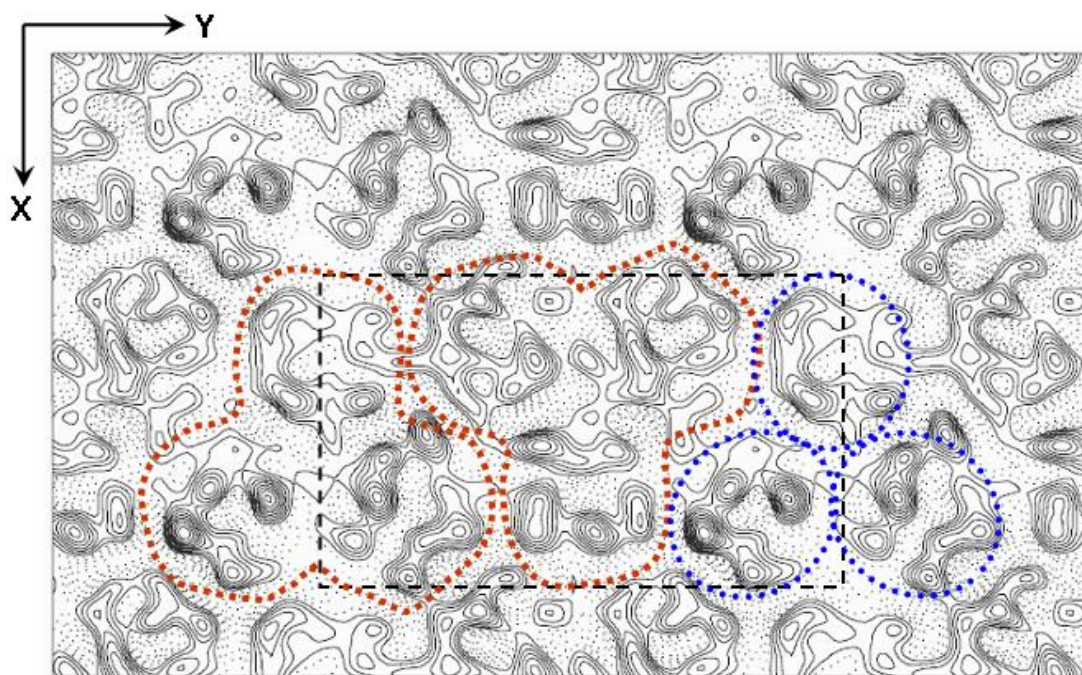


**Figure 29. IQ plot after 3 unbendings**

A bigger square size represents a stronger spot. The circles show the resolutions of 12, 11, 10, 8, 6 Å.



The result from ALLSPACE showed a highest possibility in  $p12_1_b$ , followed by  $p12_a$ ,  $p222_1_a$ , and  $p2$  respectively (Table 10). Symmetries  $p2$ ,  $p12_a$  and  $p222_1_a$  all showed high but still acceptable phase residuals, which were in between of the very good values from the crystals in *E. coli* lipids/CL and the unacceptable values from the crystals in *C. glutamicum*. It implies that in the synthetic PG BetP $\Delta$ C45 tended to form  $p12_1_b$  crystals without mirror symmetry. Like the other crystals, the projection density map showed a single unit cell consisting of two BetP $\Delta$ C45 trimers with a unit cell dimensions of similar lengths ( $91.7 \text{ \AA} \times 152.7 \text{ \AA}$ ,  $90^\circ$ ) (Figure 30). The trimer density was well recognized, even though the projection structure showed a less contrasty density because of weaker data.



**Figure 30.** A non-symmetrized projection maps of a vesicular crystal in PG 16:0-18:1. The projection map was calculated to a resolution of  $12 \text{ \AA}$  with a B factor of  $-200$  applied. Crystalline features are shown: a single unit cell (black dashed line), BetP $\Delta$ C45 trimers (red dotted line), and BetP $\Delta$ C45 monomers (blue dotted ovals).

### 3.6. Lipid analysis by TLC and mass spectrometry

The three types of crystals grown in different lipids showed distinguishable packing of protein molecules; lipids therefore had a clear effect on crystal packing. The question we asked was which lipids were needed and how much of them. We tried to answer this by analyzing the lipid

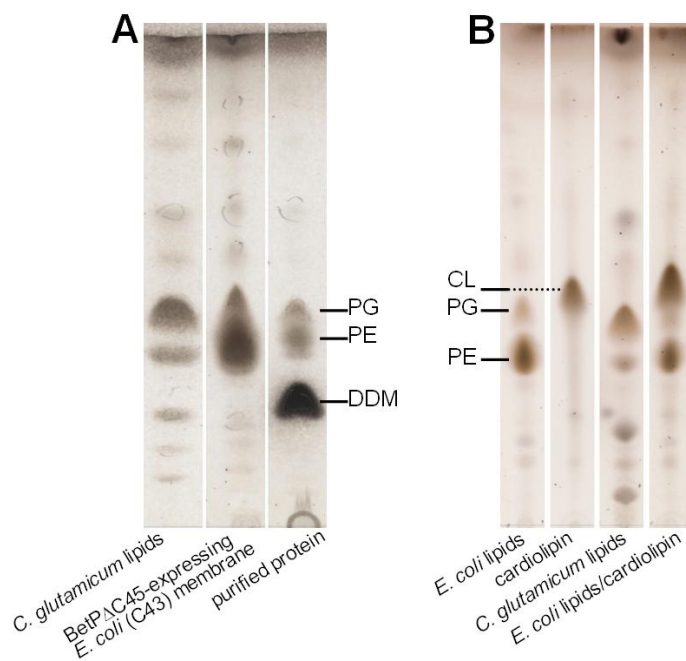
---

composition in the initial lipid extract, the purified protein and a lipid extract from the 2D crystals.

Detecting and quantifying each lipid species from a limited amount of specimen is however not a trivial task. NMR, MS and high performance liquid chromatography (HPLC) are suitable methods to determine lipid species and quantity. However, NMR generally requires a rather pure sample, while MS could only detect lipid species but can not be used for quantitation. HPLC could quantify and determine each lipid class but not lipid species, and furthermore would need a large amount of sample (>10 mg). The method meeting all our criteria was mass spectrometry by multiple precursor ion scanning (MPIS) (see 3.6.2.). This powerful high-throughput oriented mass spectrometric tool allows sensitive, molecular-specific characterization and quantitative analysis of individual phospholipid species directly from total lipid extracts (Ekroos, Chernushevich et al. 2002; Ekroos, Ejsing et al. 2003; Ejsing, Duchoslav et al. 2006). We applied this method to analyze the lipids at different stages in order to understand the relation between protein molecules and lipids during 2D crystal formation.

### **3.6.1. Preliminary analysis by thin-layer chromatography**

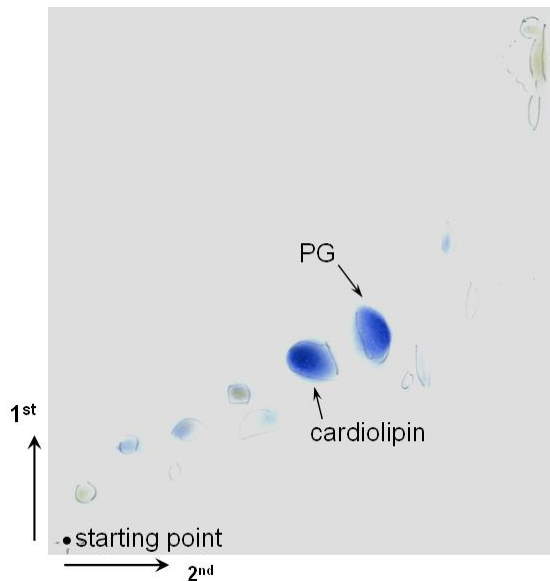
Lipids prepared by chloroform/methanol extraction were preliminarily evaluated by TLC. Lipid extractions from BetPΔC45-expressing *E. coli* membranes and the DDM-solubilized, purified protein showed the same components as commercial *E. coli* polar lipids (Figure 31). *E. coli* cell membranes consist of 75% PE and 19% PG (Morein, Andersson et al. 1996). The bands of PG, PE, and DDM were clearly visualized by heating after H<sub>2</sub>SO<sub>4</sub> oxidation, while the other weak bands could not be assigned. In comparison, *C. glutamicum* lipids appeared to be more complex and showed seven minor bands (Figure 31).



**Figure 31. Silica gel TLC of *C. glutamicum* lipids, BetPΔC45-associated lipids, *E. coli* lipids and bovine cardiolipin.**

The extracted samples were loaded on TLC plate and developed with  $\text{CHCl}_3$ : acetone: methanol: acetic acid: water (50:20:10:10:5, v/v). Lipids were visualized by heating after  $\text{H}_2\text{SO}_4$  oxidation. (A) From left: *C. glutamicum* total lipid extract, BetPΔC45-expressing *E. coli* membranes (BL21 (C43)), and DDM-solubilized, purified BetPΔC45. (B) From left: commercially available *E. coli* polar lipids, bovine cardiolipin, *C. glutamicum* lipid extract, and a mixture of *E. coli* polar lipids/bovine cardiolipin (3:2, w/w).

Two reagents were used to detect specific chemical groups: ninhydrin and molybdenum blue reagent. Ninhydrin visualizes compounds with primary or secondary amines in deep blue or purple, and is used to detect PE. Molybdenum blue reagent visualizes phospholipids in blue. *C. glutamicum* does not synthesize PE (Hoischen and Krämer 1990) and correspondingly ninhydrin staining did not visualize any signal on the TLC plate (data not shown). Two-dimensional TLC was used to achieve higher resolution of lipids. For *C. glutamicum* lipids, two dominant spots were observed by 2D TLC when stained with molybdenum blue reagent (Figure 32). These two strong signals were assigned to PG and cardiolipin by MS analysis by MPIS (see 3.6.2). Lipids in 2D crystals, however, were not analyzed by TLC because this method demands a large amount of lipids to be detected.



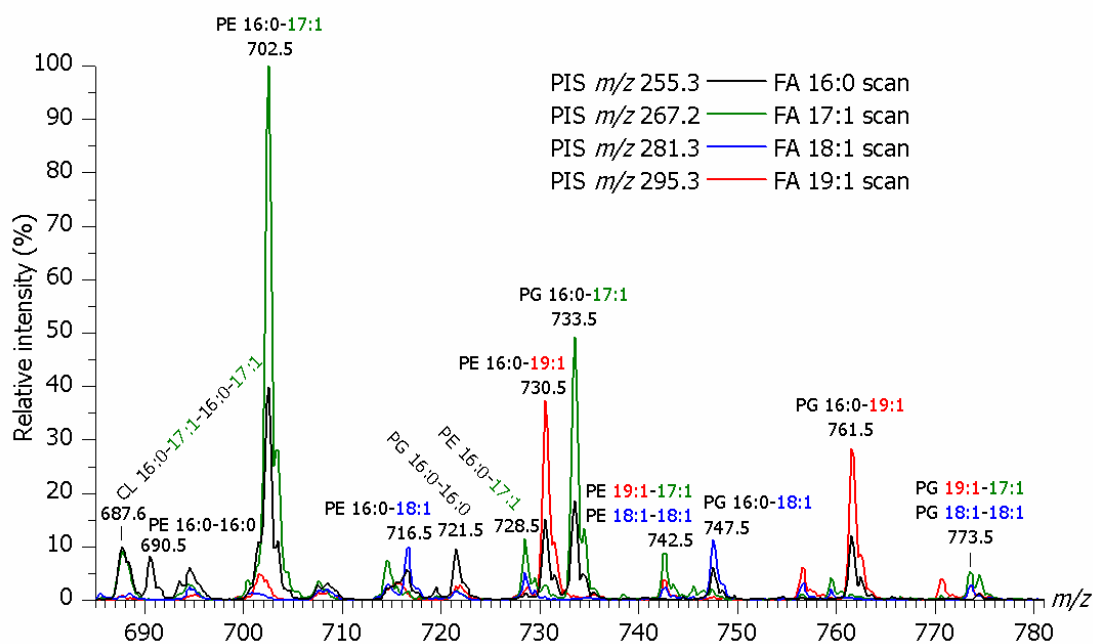
**Figure 32. Two-dimensional silica gel TLC of *C. glutamicum* lipid extract**

In the first dimension, lipids were resolved by a  $\text{CHCl}_3$ : methanol: water (60:25:4, v/v) mixture. The second dimension was developed with  $\text{CHCl}_3$ : acetone: methanol: acetic acid: water (50:20:10:10:5, v/v) was used for the second dimension. The TLC plate was sprayed with molybdenum blue to visualize phospholipids.

### 3.6.2. Mass Spectrometric analysis by multiple precursor ion scanning

MS analysis by multiple precursor ion scanning detects individual glycerophospholipid species based on the molecular-specific release of fatty acid moieties as acyl anions upon fragmentation. The spectral profile of the total lipid extract from purified BetP $\Delta$ C45 is shown in Figure 33. For example, fragmentation (i.e. collision-induced dissociation) of PE 16:0-17:1 with  $m/z$  702.5 promotes the release of the constituent FA 16:0 and FA 17:1 as acyl anions with  $m/z$  255.23 and  $m/z$  267.23 (Figure 33). Similarly, other lipid species are resolved by their unique mass ( $m/z$ ) and concomitant release of specific fatty acid fragment ions (Ekroos, Chernushevich et al. 2002; Ejsing, Duchoslav et al. 2006). Absolute quantitation of glycerophospholipid species was readily achieved by spiking total lipid extracts with the unique lipid standards: PA 17:0-17:0, PE 17:0-17:0, PG 17:0-17:0, DAG 17:0-17:0, PI 17:0-17:0 and CL 14:0-14:0-14:0-14:0 (Ejsing, Duchoslav et al. 2006).





**Figure 33. Lipid profile of a total lipid extract of purified BetPΔC45 expressed in *E. coli* membranes.**

Lipid profile of a total lipid extract of purified BetPΔC45 expressed in *E. coli*. The total lipid extract was analyzed by multiple precursor ion scanning analysis as described in Materials and Methods. The overlay of precursor ion scans for FA 16:0 (black line, precursor ion spectra (PIS)  $m/z$  255.2), FA 17:1 (green line, PIS  $m/z$  267.2), FA 18:1 (red line, PIS  $m/z$  281.3) and FA 19:1 (red line, PIS  $m/z$  295.3) shows detected lipid species annotated by their FA moieties. For presentation clarity, only 4 precursor ion spectra out of the 21 acquired are shown. The quantitation of identified lipid species was achieved by spiking the total lipid extracts with known amounts of synthetic glycerophospholipid standards (one for each lipid class), having FA 17:0 moieties (for PA, PE, PG, PI and DAG) and FA 14:0 moieties (for CL) (data not shown)

### Lipid composition of the purified protein

The result of the purified BetPΔC45 lipid extract analysis showed that PE and PG species comprise 80 mol% and 17 mol%, respectively, of the total lipid content (Table 11). Only minor amounts of PA and CL species were detected. The main lipid species extracted from purified BetPΔC45 were PE 16:0-17:1 (35 mol%), PE 16:0-19:1 (13 mol%), PE 14:0-16:0 (7 mol%), PE 17:1-18:1 (4 mol%), as well as PG 16:0-17:1 (7 mol%) and PG 16:0-19:1 (4 mol%) (Table 11, Figure 34). Only a minor amount of the species CL 16:0-17:1-16:0-17:1 was identified (2 mol%). This result shows that the composition of the lipid species associated with purified BetPΔC45 is very similar to the lipid composition of the *E. coli* membrane.

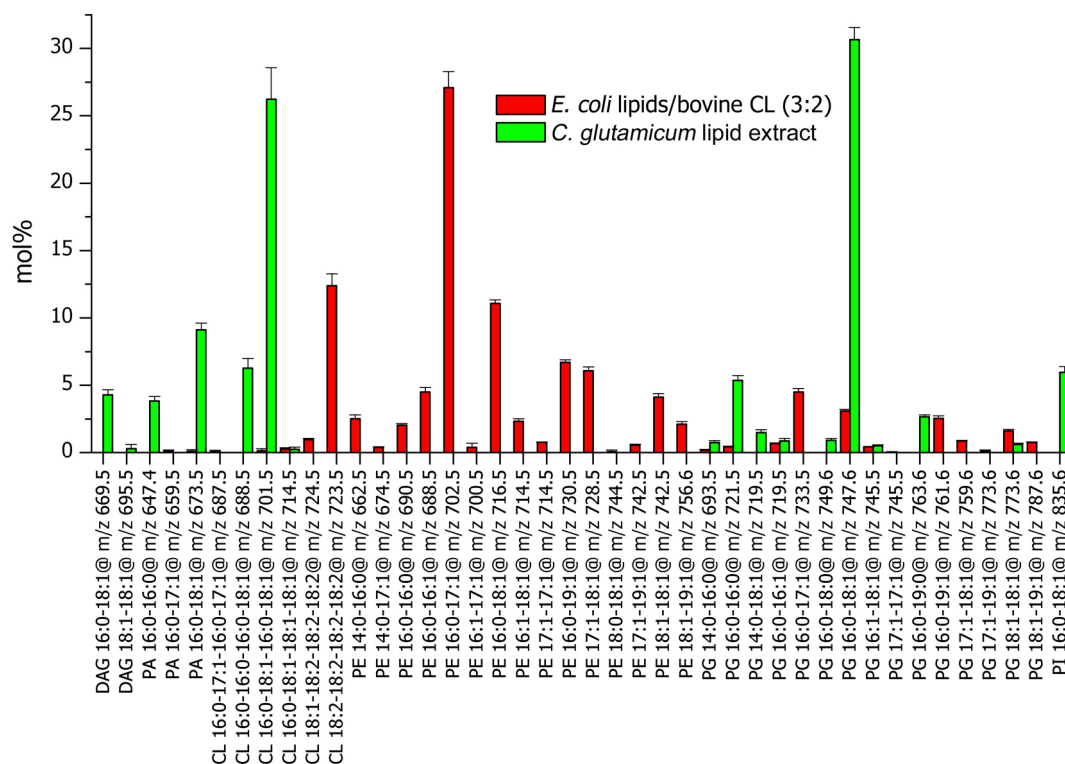
Samples	DAG (mol%)	PA (mol%)	CL (mol%)	PE (mol%)	PG (mol%)	PI (mol%)
Lipid extracts from purified protein	Negligible	1.0 ± 0.2	2.3 ± 0.4	79.6 ± 0.5	17.1 ± 0.5	Nil
<i>E. coli</i> lipids/bovine CL (3:2)	Nil	0.2 ± 0.1	13.8 ± 0.5	70.7 ± 0.9	15.2 ± 0.4	Nil
<i>C. glutamicum</i> extract	4.5 ± 0.3	12.9 ± 0.4	32.8 ± 1.5	Nil	43.8 ± 0.6	6.0 ± 0.2
Crystals in <i>E. coli</i> lipids /bovine CL (3:2)	5.6 ± 0.4	3.3 ± 0.3	4.2 ± 0.1	65.6 ± 1.1	21.3 ± 0.4	Nil
Crystals in <i>C. glutamicum</i> extract	8.5 ± 2.5	3.5 ± 0.9	9.3 ± 1.3	43.0 ± 2.8	35.7 ± 1.5	Negligible
Crystals in PG 16:0-18:1	2.0 ± 0.3	0.14 ± 0.07	0.94 ± 0.08	51.7 ± 3.5	45.2 ± 3.4	Nil

**Table 11. Lipid class composition of purified BetPAC45, lipid samples for crystallization, and BetPAC45 crystals.**

Chloroform/methanol-extracted samples before (purified protein, additional lipids for crystallization) and after crystallization (2D crystals) were analyzed by mass spectrometry with multiple precursor ion scattering. Quantities of DAG, PA, CL, PE, PG and PI are compared in mol%.

### Lipid composition of the lipids used for 2D crystallization

In order to better evaluate the crystallization behavior, lipid samples added for crystallization (the mixture of *E. coli* polar lipid extract/CL and the *C. glutamicum* lipid extract) and lipid extracts from the three crystal types were analyzed by the same MS approach by MPIS. The lipid analysis of the *E. coli* polar lipid extract/CL (3:2) mixture showed that PE 16:0-17:1 was the predominant lipid species (27 mol%) together with PE 16:0-18:1 (11 mol%), PE 16:0-19:1 (7 mol%) and PE 17:1-18:1 (6 mol%) (Figure 34). The additional bovine CL (CL 18:2-18:2-18:2-18:2) comprised 13 mol%. The amount of CL 16:0-17:1-16:0-17:1 was negligible (< 0.1 mol%). The major lipid species in *C. glutamicum* lipid extract were PG 16:0-18:1 (31 mol%), CL 16:0-18:1-16:0-18:1 (26 mol%), PA 16:0-18:1 (9 mol%), PI 16:0-18:1 (6 mol%), and CL 16:0-16:0-16:0-18:1 (6 mol%) (Figure 34). The quantity of each lipid class is shown in Table 11.

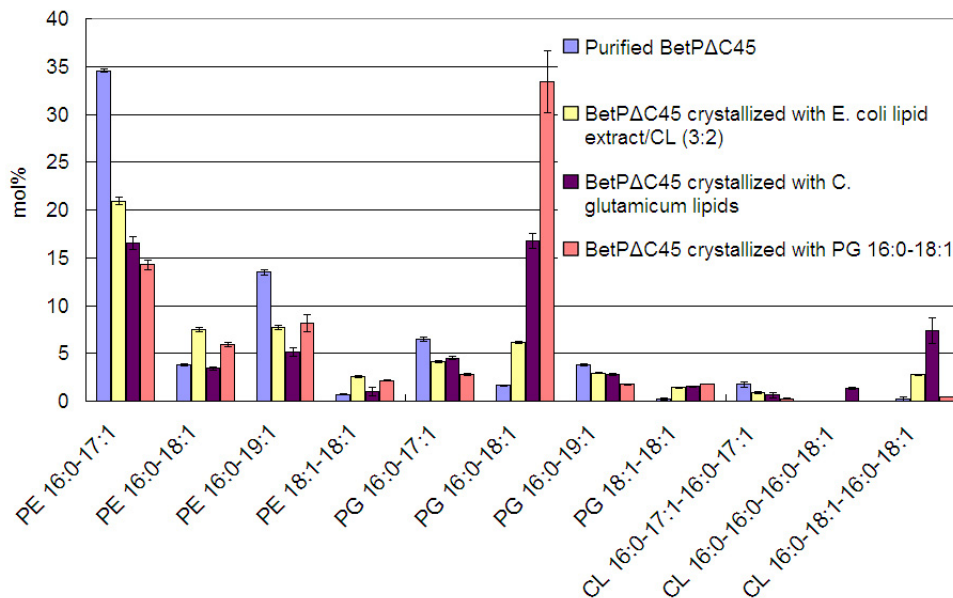


**Figure 34. Quantitation of identified individual lipid species and spectral profiles obtained by lipid class-specific PIS and lipid species-specific MPIS on the mixture of *E. coli* polar lipid extract and bovine cardiolipin (3:2, w/w) and the *C. glutamicum* lipid extract used for 2D crystallization.**

PIS at  $m/z$  702.50 and 732.90 were identified as PE 16:0-17:1 and CL 18:2-18:2-18:2-18:2 for the mixture of *E. coli* lipid extract/bovine CL. The first two dominant peaks (PIS  $m/z$  at 701.50 and 747.50) were identified as CL 16:0-18:1-16:0-18:1 and PG 16:0-18:1 for the *C. glutamicum* lipid extract.

### Lipid composition of the crystals

The lipid composition of 2D crystals formed in the presence of the mixture of *E. coli* lipid extract/bovine CL, the *C. glutamicum* lipid extract, or synthetic PG 16:0-18:1 showed that PE species were the major constituents of the BetP crystals with 65 mol%, 43 mol% and 52 mol% respectively (Table 11). Other detected lipid species were PG (21 %, 36%, 45%), CL (4 %, 9%, 1%), and PA (3%, 4%, <1%). Figure 35 shows the amounts of the major lipid species detected in the various BetP crystals and in the purified protein. The main species detected were PG 16:0-18:1, PE 16:0-17:1, PE 16:0-19:1 and CL 16:0-18:1-16:0-18:1. Bovine CL (18:2-18:2-18:2-18:2) was surprisingly not found in *E. coli* lipids/bovine CL.



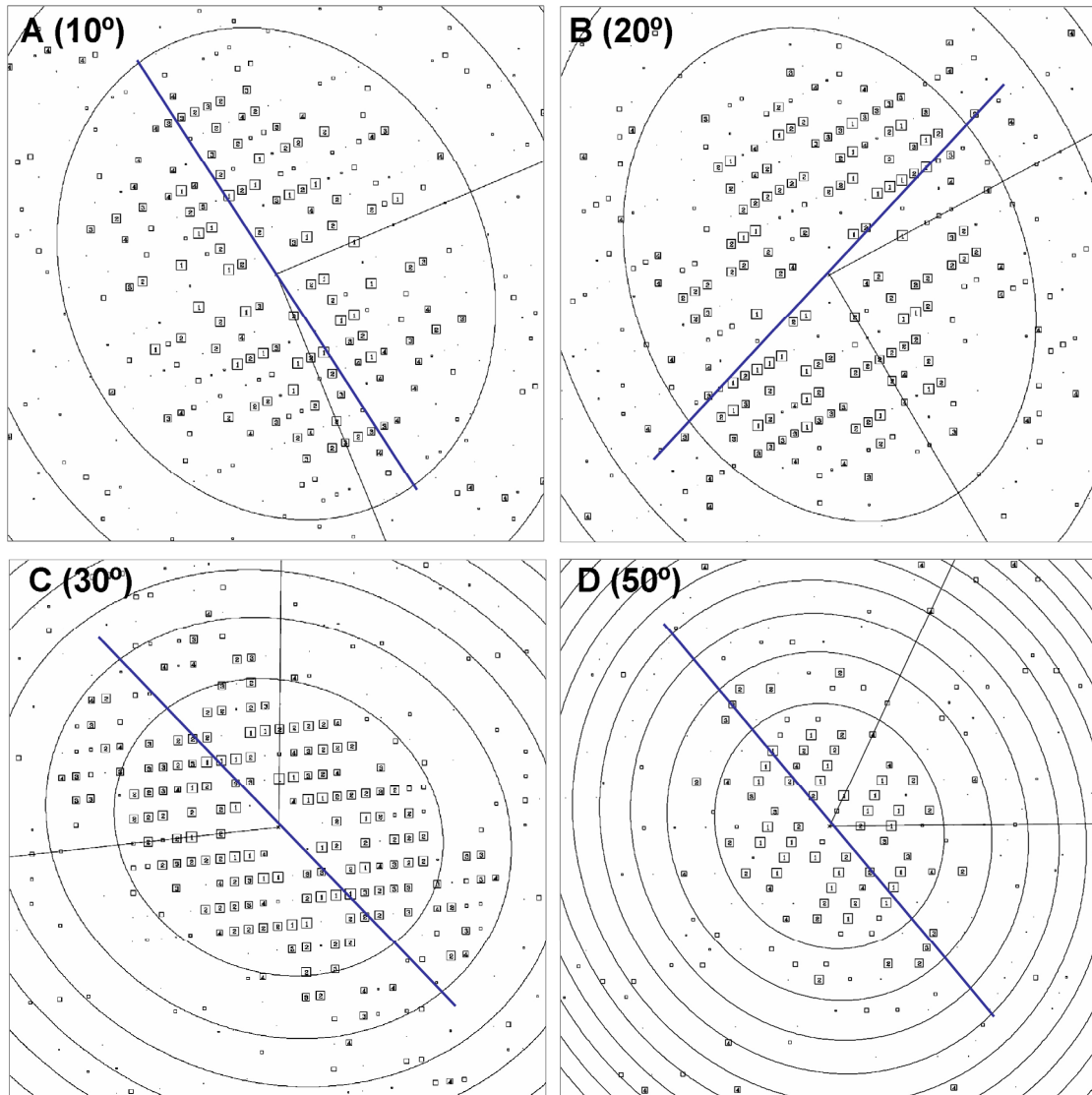
**Figure 35.** Comparison of the major PE, PG and CL species detected in the total lipid extracts of purified BetPΔC45 expressed in *E. coli*, 2D crystals using the mixture of *E. coli* lipid extract/bovine CL (3:2), synthetic PG 16:0-18:1, and the *C. glutamicum* lipid extract.

### 3.7. 3D map and NCS averaging

BetPΔC45 sheet-like crystals grown with the *C. glutamicum* lipid extract showed a well-ordered packing in p12<sub>1</sub>\_b symmetry, and were chosen for 3D map reconstruction.

#### 3.7.1. Data collection of tilted crystals

The data collected from the untilted crystals showed the information only in the XY plane. To gain the structural information in the third dimension, specimens were tilted for data collection. However, data collected from tilted crystals is generally anisotropic, showing a poorer resolution in the direction perpendicular to the tilt axis compared to that along the tilt axis. This is due to lack of flatness of the specimen.



**Figure 36. Tilted data blue line shows the tilt axis**

IQ plots of single images collected from specimens at tilt angle: (A) 10° (image 5613); (B) 20° (image 2389); (C) 30° (image 3301); (D) 50° (image 4066). The IQ value increases as the square size decreases. The edge of the IQ plot is 8 Å. Black circles represent the nodes of the calculated contrast transfer function (CTFFIND). Blue lines show the tilt axis of the image, determined by the program EMTILT.

A lack of flatness can be described as molecules in 2D crystals are upshifted or downshifted from the crystal membrane along the Z direction. Specimens lacking flatness usually rendered ignorable effects in losing high resolution information when they are not tilted; it is because that it only records the information of the XY plane in the crystals. In contrast, as the specimens are tilted, information along the Z direction is also recorded, and molecules shifted from the crystal membrane can thus be recognized. This situation causes a loss of sharpness in reflection spots and a decrease in S/N.

---

If the signal-to-noise ratio decreases to 1, then the signal can no longer be recognized. As observed, data collected from low-angle tilted specimens (10-30°) showed similar resolution along the tilt axis compared to the 0°-tilted data, while the resolution perpendicular to the tilt axis became worse (Figure 36). At a high tilt angle of 50°, information at high resolution was reduced in all dimensions.

### **3.7.2. Handedness determination**

During handedness determination, the phase residuals of 0° images showed a clear difference between “flipping” and “not flipping” the image merged against the 0° reference image 2072 (Table 12). For data collected from tilted crystals, this difference between “flipped” and “unflipped” became smaller due to fewer comparisons in Fourier space. The discrimination of the handedness was encoded in the structural information higher than 12 Å; this is because the handedness can only be recognized by detailed features, i.e. the arrangement of helices, which is revealed only at resolution above 10 Å. At a resolution of 15 Å, monomers with and without flipping look so similar as the difference was insufficient to distinguish the handedness. However, the structural information at higher resolution (8-12 Å) was gradually weakened as the tilt angle increased. Therefore, the difference between flipped and unflipped lattices became less significant due to loss of high resolution data (Table 12).

Image	Tilt angle	Reference	Phase residual without flipping (°)	Phase residual with flipping (°)	resolution
2081	0	2072.aph	26.114 (46)	55.318 (54)	7 Å
2082	0	2072.aph	52.039 (54)	24.308 (73)	7 Å
2073	0	2072.aph	48.244 (56)	23.043 (57)	7 Å
2095	0	2072.aph	46.299 (61)	25.721 (59)	7 Å
1194	0	2072.aph	42.637 (49)	27.637 (54)	7 Å
5611	10	merged 0°	29.153 (47)	46.967 (50)	7 Å
5613	10	merged 0°	34.755 (37)	50.042 (40)	7 Å
2397	20	merged 10°	48.407 (82)	30.310 (82)	8 Å
2389	20	merged 10°	58.422 (43)	31.067 (65)	8 Å
2391	20	merged 10°	42.430 (92)	29.362 (65)	8 Å
2405	20	merged 10°	48.192 (41)	29.942 (56)	8 Å
3301	30	merged 20°	48.503 (79)	33.239 (72)	8 Å
3820	30	merged 20°	49.639 (50)	20.776 (51)	8 Å
3853	30	merged 20°	41.077 (38)	27.885 (38)	8 Å
2669	30	merged 20°	46.046 (35)	36.985 (45)	8 Å
4065	50	merged 30°	31.563 (28)	26.610 (27)	12 Å
4066	50	merged 30°	20.395 (27)	29.585 (25)	12 Å
4689	50	merged 30°	29.997 (22)	46.186 (23)	12 Å
4696	50	merged 30°	42.122 (19)	25.565 (19)	12 Å
4105	50	merged 30°	42.447 (12)	16.686 (11)	12 Å
4678	50	merged 30°	22.290 (27)	30.401 (25)	12 Å

**Table 12. Handedness determined by comparing the phase residuals with and without flipping the target image.**

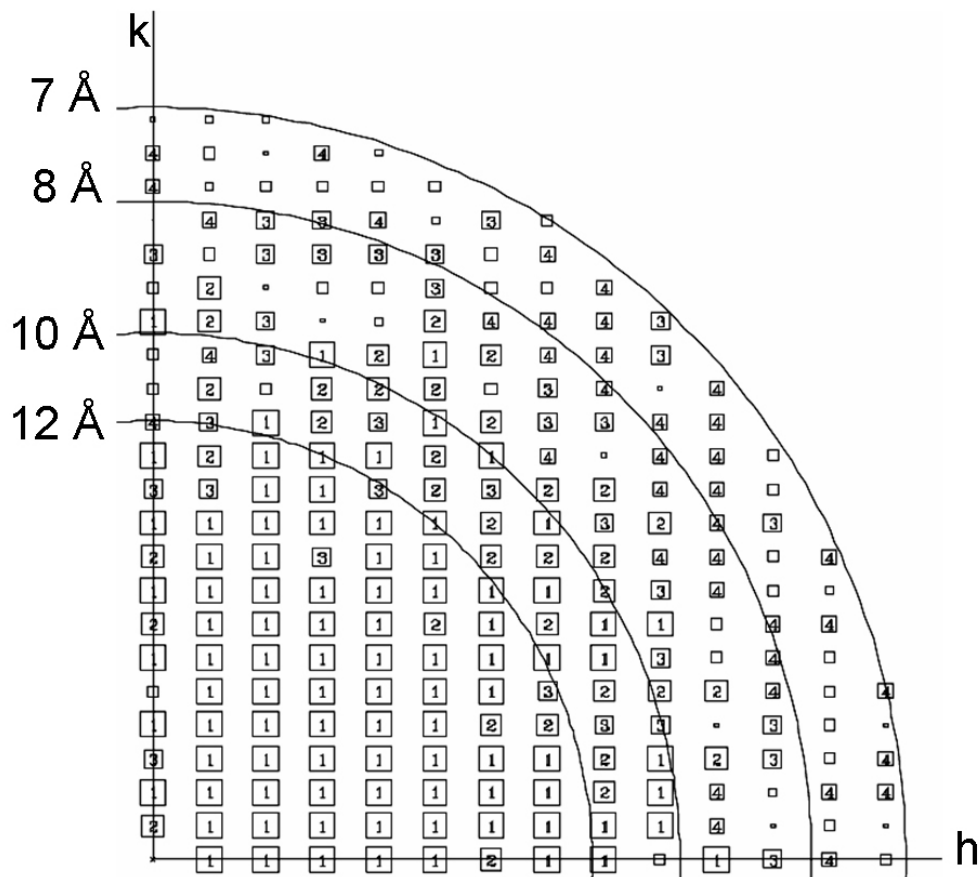
Different references were applied to determine the handedness of the target image. It was calculated from reflections of IQ 1-5 ORIGITLTK to different resolution, depending on the resolution of the target image. Numbers in parentheses showed how many reflections were used for comparison.

### 3.7.3. 3D data merging

The phase origin was refined by ORIGITLTK with p12<sub>1\_b</sub> applied before merging, and it resulted in a phase residual for each image as listed in Appendix II. The final tilt geometry was refined one time by using a preliminary 3D data set as a reference, and the final tilt angle for each image is listed in Appendix II. The final data set was merged from 79 images (19 × 0°, 4 × 10°, 22 × 20°, 17 × 30°, 17 × 50°).

For a highly averaged projection map, the merged reflections in Fourier space were projected to  $(h, k, 0)$  and plotted to 7 Å (Figure 37). The merged phase residuals in different resolution shells showed that the data was properly merged because the phase error was well below 45° (Table 13); a

phase error of 45° at p12<sub>1</sub>\_b indicates that the lattices were merged randomly.



**Figure 37. IQ plot in the  $hk$  plane of the 3D merged data set**  
Numbers in the squares represent the IQ value.

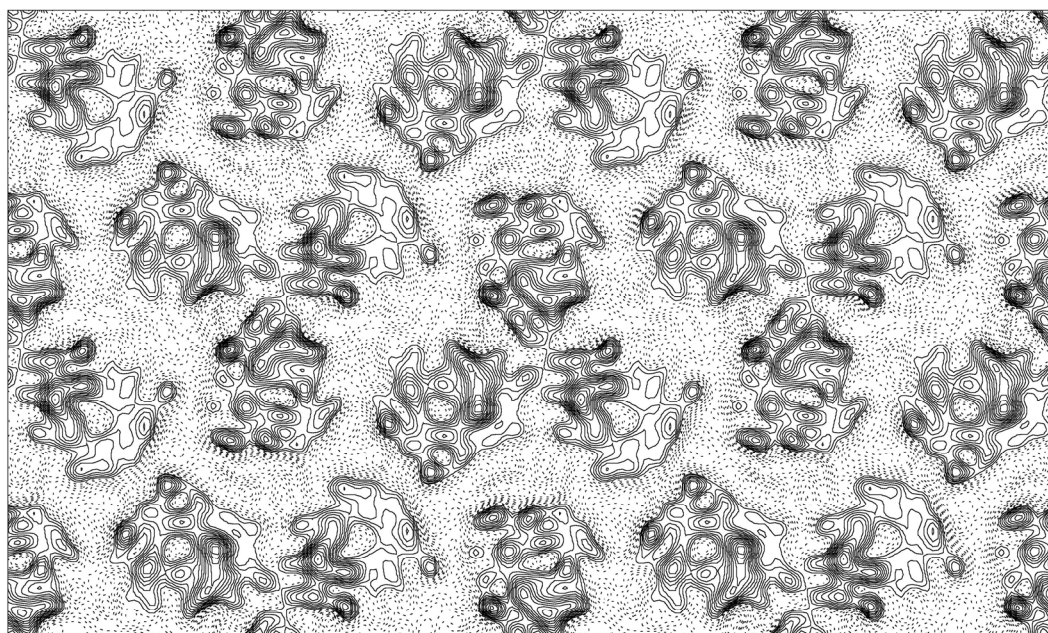
Resolution (Å)	No. of reflections	Averaged phase error (°)
180 – 20.9	32	8.0
14.7	30	5.3
12.0	28	9.5
10.4	27	16.0
9.3	29	16.2
8.5	28	32.8
7.9	26	26.9
7.4	30	33.3
6.9	22	36.0

**Table 13. Phase error in different resolution shells after merging**



---

The size of the unit cell was determined by averaging the unit cells of nineteen  $0^\circ$  images, resulting in  $92.1 \text{ \AA} \times 155.2 \text{ \AA}$ . The unit cell dimension perpendicular to the crystal membrane was arbitrarily set to  $150 \text{ \AA}$ , i.e. about 3 times the expected thickness of the membrane crystals. The projection map of the merged data set showed the same features as in the reference image (Figure 38). The crystallographic details of the merged 3D data set are listed in Table 14.



**Figure 38. Projection density map at 8 Å calculated from the merged 3D data set.**

The unit cell dimensions are  $92.1 \text{ \AA} \times 155.1 \text{ \AA} \times 150 \text{ \AA}$ ,  $90^\circ$ ,  $90^\circ$ ,  $90^\circ$ . The map was calculated from the merged 3D data set with the symmetry  $p12_1b$  applied, scaled to a maximum density of 250 and contoured in steps of 17.5. An isotropic temperature factor ( $B = -250 \text{ \AA}^2$ ) was applied to compensate for the resolution dependent degradation of image amplitudes.

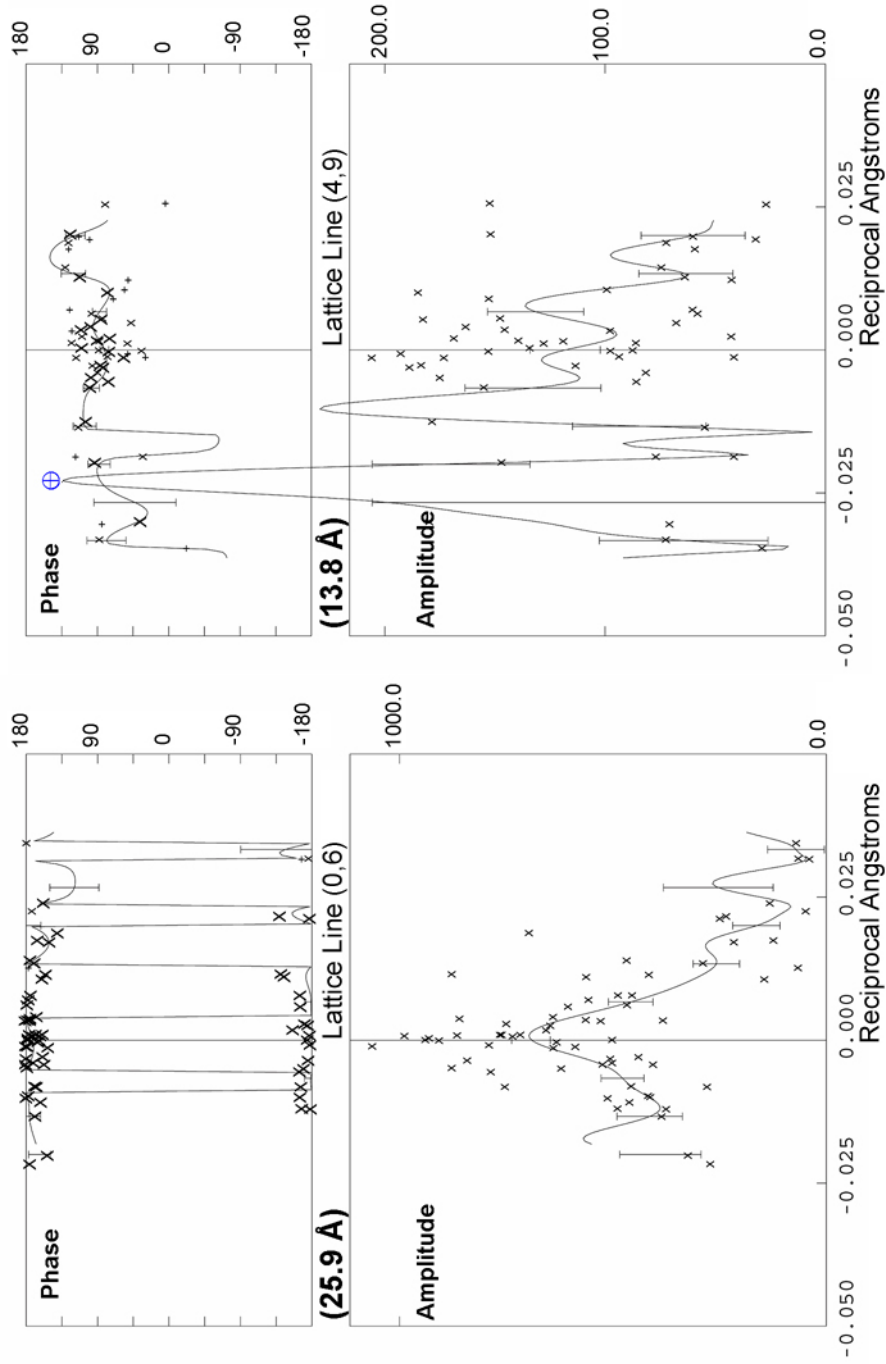
The merged data was evaluated by LATLINEK, which uses the observed reflections to draw the trend lines for amplitudes and phases (Figure 39). Curves were fitted to the plotted data and sampled at  $\Delta Z = (1/150) \text{ \AA}^{-1}$ . In Figure 39, the reflection (0, 6) shows a trend line for phases which locates around  $180^\circ$  (in phases,  $180^\circ$  is equivalent to  $-180^\circ$ ). The fitted curve for the amplitudes showed the strongest signal at  $0 \text{ \AA}^{-1}$  while the amplitudes decreases as the reciprocal  $\text{\AA}$  shifted away from  $0 \text{ \AA}^{-1}$ . LATLINEK also created a simulated data set based on these trend lines for phases and

---

amplitudes, and this data set can afterwards be used to display the 3D map.

Amplitude refers to how much a molecule scatters the wave. The initial 3D map showed strong noises outside the membrane, which was supposed to be empty (Appendix III). These noises came from the over-weighted strength of the signals. The symbol “ $\oplus$ ” in the amplitude plot of reflection (4, 9) refers to the simulated signal which is obviously out of scale (Figure 39). This situation was frequently observed in the reflections which had weaker averaged amplitudes, higher resolution than 15 Å, and were away from 0 reciprocal Å. To suppress the noises, these out-of-scale amplitudes were manually modified to fit into the amplitude scale, which was no larger than the amplitude at 0 Å<sup>-1</sup> or the scale bar. The phases remained the same because phase is the key information to determine a structure. After modification of the amplitudes, most of the noises were removed and the 3D map became clearer (Figure 40A).

Another parameter that required being fine-tuned was the tilt geometry. The merged 3D data set was used as the reference file (MTZ format) to adjust the tilt geometry (tilt angle and tile axis) for each lattice. This step was to fit the phases and amplitudes of each lattice into the reference by adjusting the tilt geometry. The result was evaluated by the phase residual. Only the tilt geometry resulting in a lower phase residual was applied to create the next 3D data set, which resulted in the final 3D map discussed in **3.7.4**.



**Figure 39. Lattice line plots of amplitudes and phases along the  $l$  ( $Z^*$ ) dimension.**

The program LATLINEK was used to complete the phase and amplitude information along the  $l$  ( $Z^*$ ) dimension. The three-dimensional diffraction pattern of a 2D crystal shows spots in the  $hk$  plane and "rods" along the  $l$  dimension. During 3D data collection, the information of the intersection between the rods and the imaging plane was recorded. Therefore, the data along the  $l$  ( $Z^*$ ) dimension is never complete. LATLINEK drew a trend line for the observed reflections in order to reconstruct the continuous information along the  $l$  ( $Z^*$ ) dimension. Reflections (0, 6), (4, 9), (4, 12) and (8, 9) and their corresponding resolutions at  $(h, k, 0)$  are shown in the figure. A complete cycle of the phase contains  $360^\circ$ , which is displayed between  $\pm 180^\circ$  in the upper plot of each reflection. Amplitudes of the experimental reflections are shown in the lower plot. The symbol " $\oplus$ " is discussed in the main text before this figure.

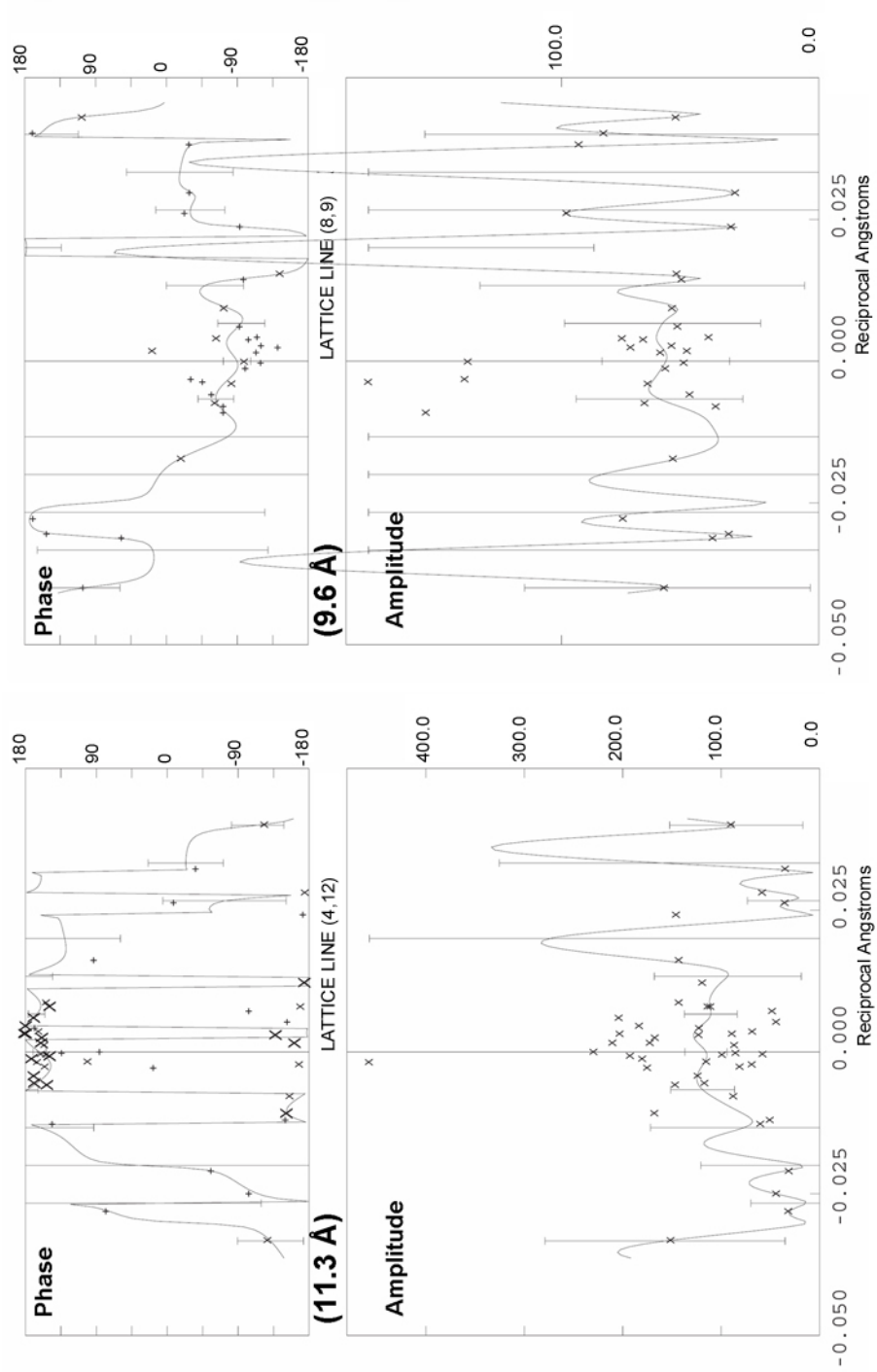


Figure 39. (Continued)

Plane group	p12 <sub>1</sub> _b (p2 <sub>1</sub> )
<b>Cell dimensions</b>	
a	92.1 Å
b	155.2 Å
c	150 Å
$\alpha = \beta = \gamma$	90°
Number of images <sup>a</sup>	79
Resolution limit for merging (Å)	8.0
Effective resolution of 3D set (Å) <sup>b</sup>	
In-plane	8.0
Perpendicular to the membrane	16.0
Total number of observations	15758
Number of structural factors	4174
<b>Completeness (%)</b>	
8 Å × 8 Å × 16 Å containing 0-50°	80
8 Å × 8 Å × 16 Å containing 0-90°	73
8 Å × 8 Å × 8 Å containing 0-50°	49
8 Å × 8 Å × 8 Å containing 0-90°	38
Overall weighted R-factor (%)	26.7
Overall weighted phase residual (°) <sup>d</sup>	20.4

**Table 14. Electron crystallographic table**

<sup>a</sup> Nineteen at 0°, four at 10°, twenty-two at 20°, seventeen at 30°, and seventeen at 50° (nominal tilts)

<sup>b</sup> As calculated from a point-spread function of the experimental data.

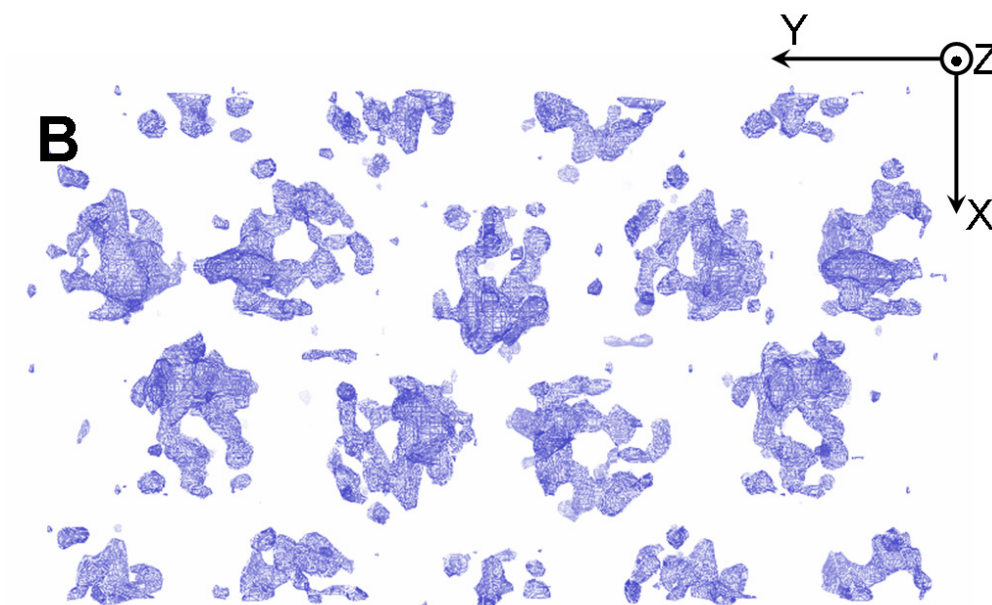
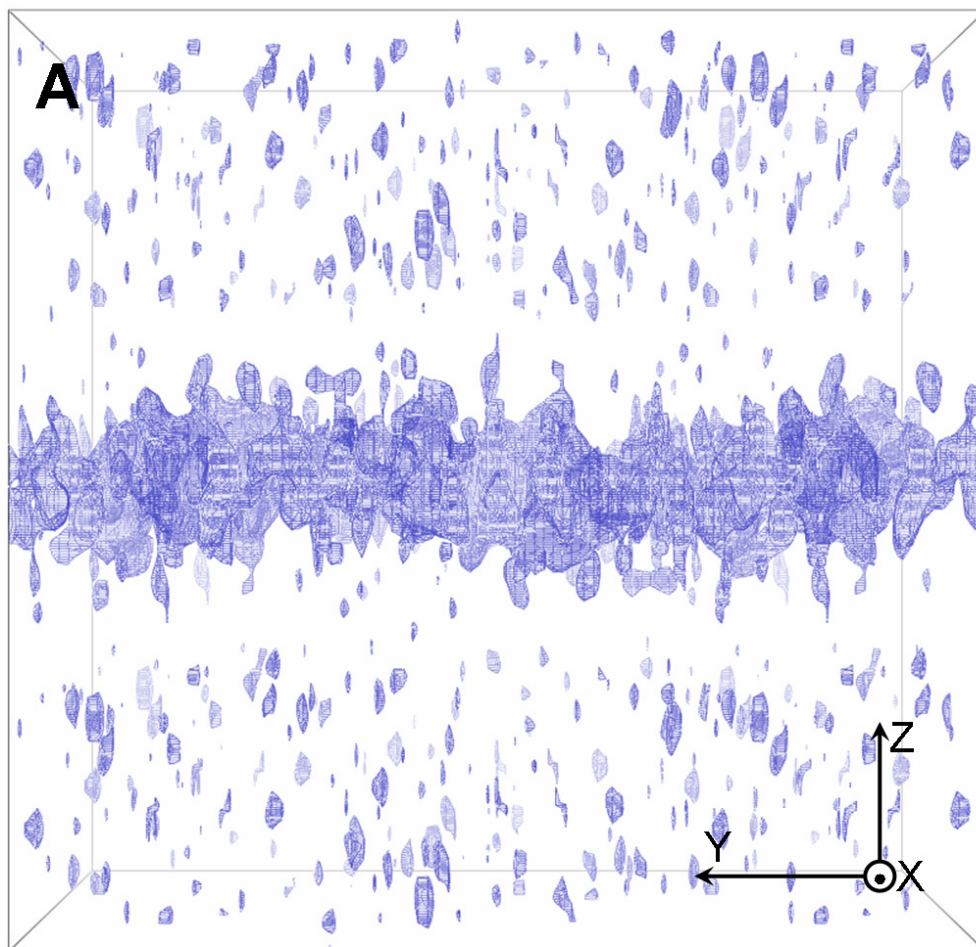
<sup>c</sup> From the program LATLINEK

### 3.7.4. 3D map

#### Description of the 3D map

After merging 79 processed images ( $19 \times 0^\circ$ ,  $4 \times 10^\circ$ ,  $22 \times 20^\circ$ ,  $17 \times 30^\circ$ ,  $17 \times 50^\circ$ ) with tilt geometry refined and amplitudes modified (see also 3.7.3.), the refined three-dimensional map showed a single-layered density in the side view (Figure 40A), which was packed with BetPΔC45 trimers (Figure 40B).

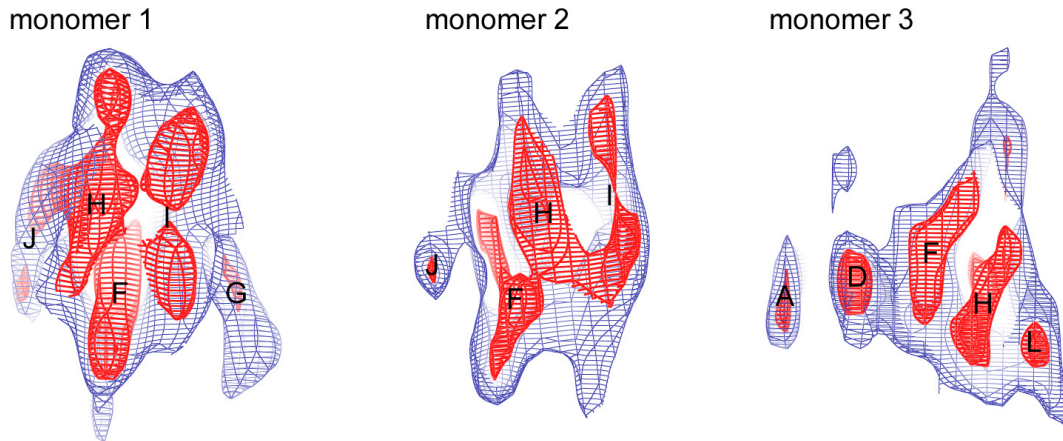
B factor and  $\sigma$  cut-off were changed for map calculation in order to see resolved densities. The map calculated with B factor  $-300 \text{ \AA}^2$  applied and displayed at 2.0  $\sigma$  cut-off did not show resolved densities near the trimer center (Figure 40 B, Figure 41). By lowering the B factor to  $-600 \text{ \AA}^2$  and increasing the  $\sigma$  cut-off up to 4.0, helices showed their individual densities. Four maps were calculated with different B factor applied:  $-300$ ,  $-400$ ,  $-500$ , and  $-600 \text{ \AA}^2$  (Appendix IV). These maps were displayed at different  $\sigma$  cut-off and used for protein modeling.



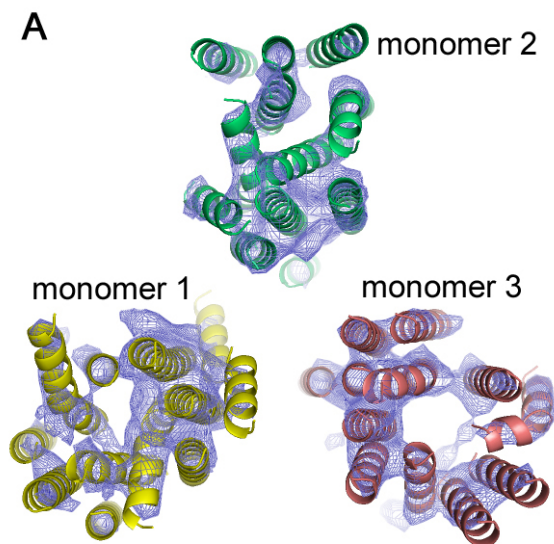
**Figure 40. Side view and top view of the 3D map.**

The 3D density map is displayed with a sigma ( $\sigma$ ) cut-off of 2.0 and a B factor of  $-300 \text{ \AA}^2$  applied. The figures of 3D map were created by using the program Pymol (DeLano 2002).

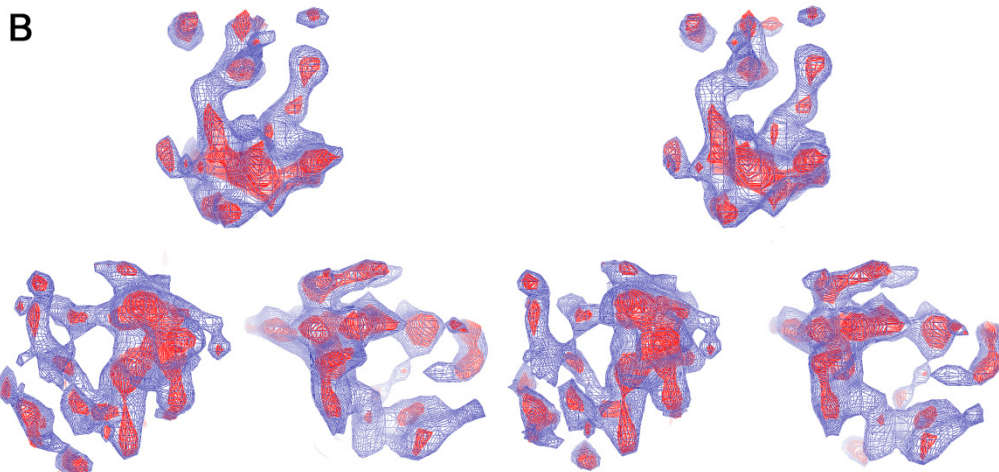




**Figure 41. Maps with different B factors were applied to see resolved density**  
 The blue map (B factor  $-300 \text{ \AA}^2$ ,  $2.0 \sigma$ ) showed unresolved density, while the red map (B factor  $-600 \text{ \AA}^2$ ,  $2.5 \sigma$ ) showed the densities to recognize helices. See Figures 42 and 43 for the nomenclature of monomers and helices.



**Figure 42. Trimer top view and stereo views of the BetPΔC45 3D map**  
 (A) Each monomer was named monomer 1 (yellow), monomer 2 (green), and monomer 3 (salmon red) respectively. (B) Stereo top view. The maps have different B factors and contour levels:  $2.0 \sigma$ , B factor  $-300 \text{ \AA}^2$  for the blue map in both subfigures, and  $2.5 \sigma$ , B factor  $-600 \text{ \AA}^2$  for the red map in the stereo view.



The three monomers were named monomer 1, monomer 2, and monomer 3 respectively for the convenience during discussion (Figure 42A). During protein model building, ideal polyalanine helices were initially used to fit into the density map displayed at a  $\sigma$  cut-off between 1.2 and 4. Twelve helices were finally fitted manually into the density of each monomer (Figure 42A). The top stereo view is shown in Figure 42B.

### Overall helical arrangement

The protein model of each monomer consisted of twelve transmembrane  $\alpha$ -helices (A-L). Since the number of helices is identical in three monomers, and each corresponding helix does not show more than 8 Å shift in the relative position, the position of helices can be compared unambiguously. The identical feature in all three monomers is the strongest density of the helix bundle F-H-I, which is used as a marker for monomer-monomer alignment (Appendix IV). Corresponding helices in each monomer did not show equivalent intensity or length in all three monomers, and were modeled independently with various numbers of amino acids (Table 15).

	A	B	C	D	E	F	G	H	I	J	K	L	Total
<b>Monomer 1</b>	20	25	20	20	25	25	20	25	25	20	15	15	255
<b>Monomer 2</b>	20	20	20	20	25	25	20	25	25	15	15	15	245
<b>Monomer 3</b>	20	20	20	20	15	25	15	25	20	20	25	15	240

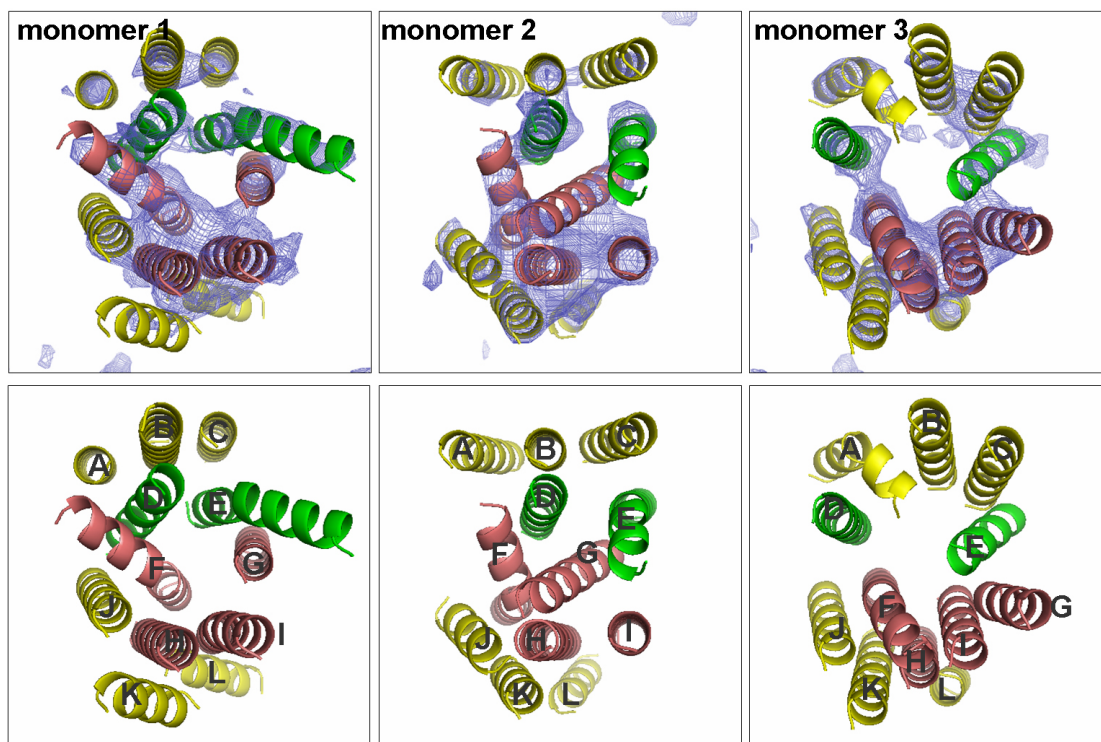
**Table 15. Numbers of amino acids in each modeled helix.**

Each helix was modeled individually. The sequence of the helices did not follow the amino acid sequence.

At the first glance, all monomers showed a cavity in the center with different shapes and sizes (Figure 43). Monomer 1 showed the strongest density while monomer 3 showed the weakest among the three monomers. The twelve helices in each monomer were classified into two peripheral regions (helices A-C, J-L) and the central region (helices D-I) surrounding a cavity in the center of each monomer (Figure 43). Helices A, B, and C were located at the rim of the trimer, forming crystal contacts with adjacent trimers. Helices J to L were located at the monomer-monomer interface near the pseudo-threefold axis inside a trimer, possibly forming monomer-monomer contacts. These helices appeared to be relatively short. Helices F, H, and I



showed the strongest density among all the helices (Appendix IV); this is the case in all three monomers. Helices D and E were located between the outer peripheral region (A-C) and helices F and G. The positions of helices D, E, and G seem to determine the size of the cavity.



**Figure 43. Top view of individual BetP $\Delta$ C45 monomers.**

Monomer 1 and monomer 3 were rotated  $\pm 120^\circ$  for comparison with monomer 2. Helices are labeled from A to L. Helices F, H, and I showed the strongest density in all three monomers. The helices are coded in three colors: peripheral region (helices A-C, J-L) in yellow; switch region (helices D, E) in green; cavity region (helices F, G, H, I) in deep-salmon. The density map is contoured at  $\sigma$  1.5.

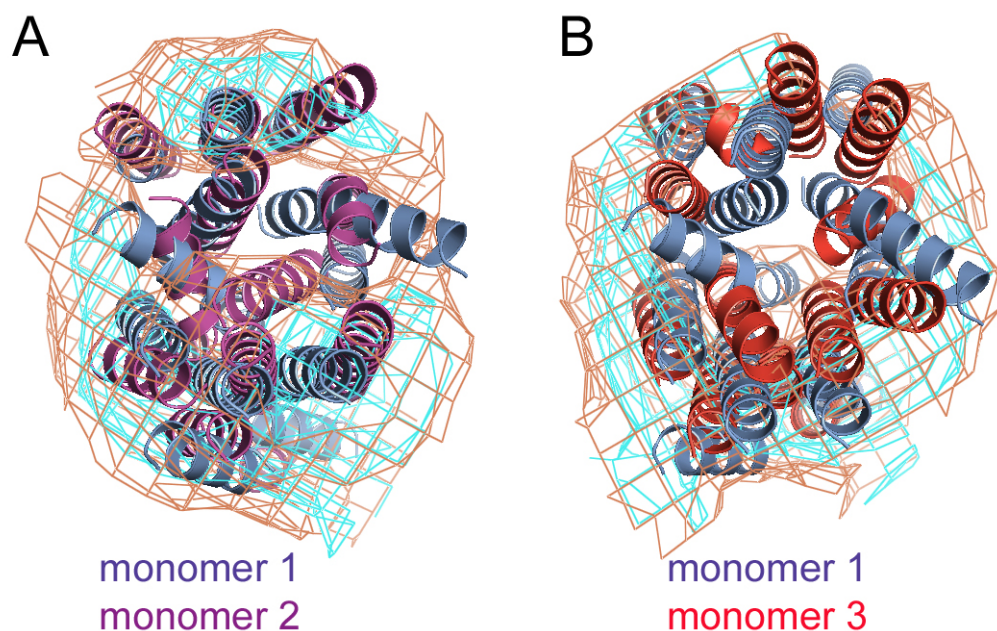
### **Non-crystallographic symmetry**

In all three monomers, each corresponding helix showed slight or obvious differences in terms of position and tilt relative to its neighbors. This suggested that the three monomers showed conformations that were different from each other. Besides, the three monomers of a trimer had different crystal contacts with the adjacent monomers. To clarify that the structural differences between the three monomers were not a result of sample preparation, data processing, and/or merging procedure, non-crystallographic threefold symmetry was applied.

---

The NCS was calculated in real space. A series of steps were designed to perform the NCS: (1) knowing relative positions of each monomer by calculating their mass centers based on the protein model; (2) mask out the density of each monomer; (3) rotate and translate the protein models of monomers 1 and 3 and align these two monomers to monomer 2; (3) calculate the correlation coefficient between protein models of monomer 2 and monomer 1/3; (4) calculate the correlation maps based on the correlation coefficient.

Monomer 1 and monomer 3 were boxed out and aligned to the density of monomer 2 by a rotation of  $\pm 120^\circ$ . The correlation map was calculated at correlation coefficient 0.619. From the correlation maps, the density disappeared around the cavity (Figure 44). It indicates a higher degree of similarity at the perimeter than in the cavity area, where the most significant structural differences are found. These structural differences between the three monomers most likely signify different states of BetP $\Delta$ C45 in the transport mechanism.



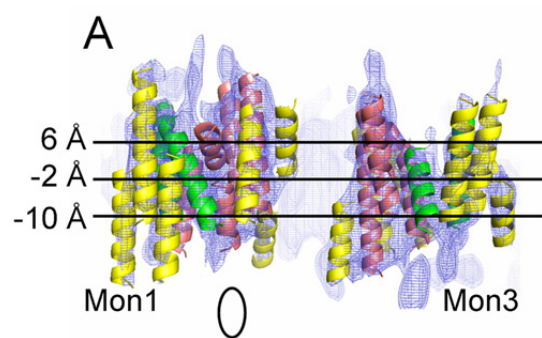
**Figure 44. Correlation map between monomers displayed at 1  $\sigma$  (cyan) and 0.5  $\sigma$  (orange) cut-offs.**

(A) Density maps correlated between monomer 1 (blue helices) and monomer 2 (purple helices); (B) density maps correlated between monomer 1 (blue helices) and monomer 3 (red helices).

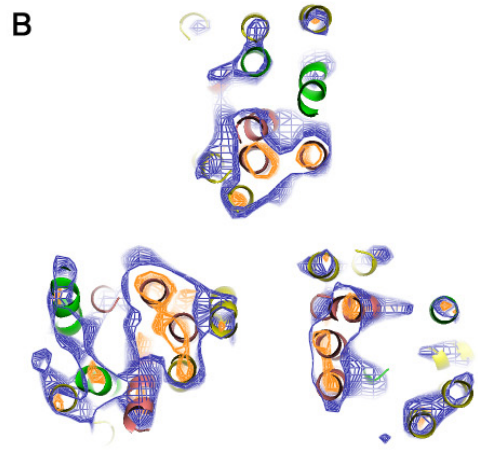
---

## Different monomer conformations

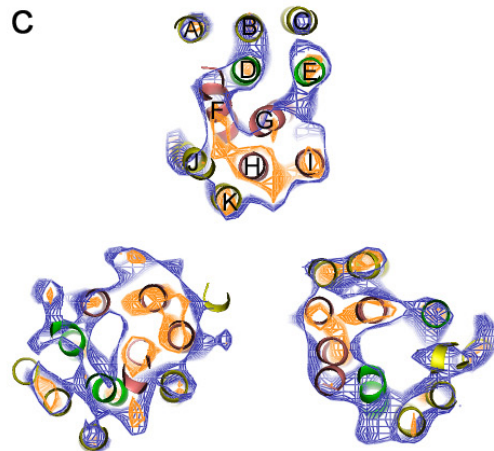
The most obvious difference between these three monomers was the size of the central cavity. Monomer 3 shows the widest cavity among the three monomers, while the helices around the cavity were more tightly packed in monomers 1 and 2 (Figure 45). The size of the cavity was mainly determined by the position of helices D, E, F, and G in monomers 1 and 2, while helices A, B, and C additionally contributed to the boundary of the central cavity in monomer 3. In monomer 1 and 2, helices E and F both show a conspicuous kink. These two helices were bent towards the outer perimeter in monomer 1, and their straight ends and helix D approach one another to constrict the central cavity. In contrast, helices E and F are straight in monomer 3 (Figure 43). The helix D in monomer 1 and 2 was located between helices B and F, also showing a linking density of B-D-F (Figure 45B-D). In monomer 3, helix D was shifted further away to the perimeter. A further displacement was possibly hindered by helix A, which showed a kink containing six amino acids at one terminus. Helices H and I were more or less parallel to each other in all three monomers, and had average tilts in the range of 7-15° perpendicular to the membrane plane. Helix G leaned towards helix H in monomer 2, twisting the shape of the central cavity. This leads to a closed appearance of monomer 2. On the contrary, helix G is shifted towards to helix I in monomer 3, leading to an increased size of the central cavity. The size of the central cavity was determined roughly by the distance between helices D and G. In monomer 3, D and G were shifted to the monomer perimeter, being ~21 Å apart, while in monomer 1 and 2, D and G stayed mainly in the central area within a distance ~7-14 Å. The D-E distances are ~7 Å for monomers 1 and 2, and 13 Å for monomer 3.



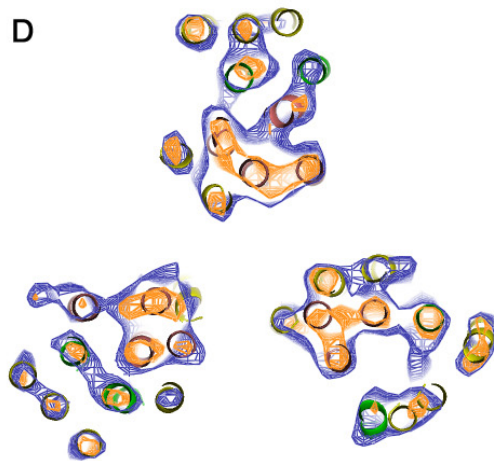
**Figure 45. Side view and horizontal slices through the density**  
 (A) Side view of monomer 1 and monomer 3. The oval shows the vertical resolution, calculated from the point-spread function derived from the experimental data.  
 (B)-(D) Horizontal section views (8 Å thick) through the density map perpendicular to the membrane plane. The blue map is applied with B factor  $-300 \text{ \AA}^2$ , displayed at  $1.3 \sigma$ , and the orange map is applied with B factor  $-600$  and displayed at  $2.5 \sigma$ .



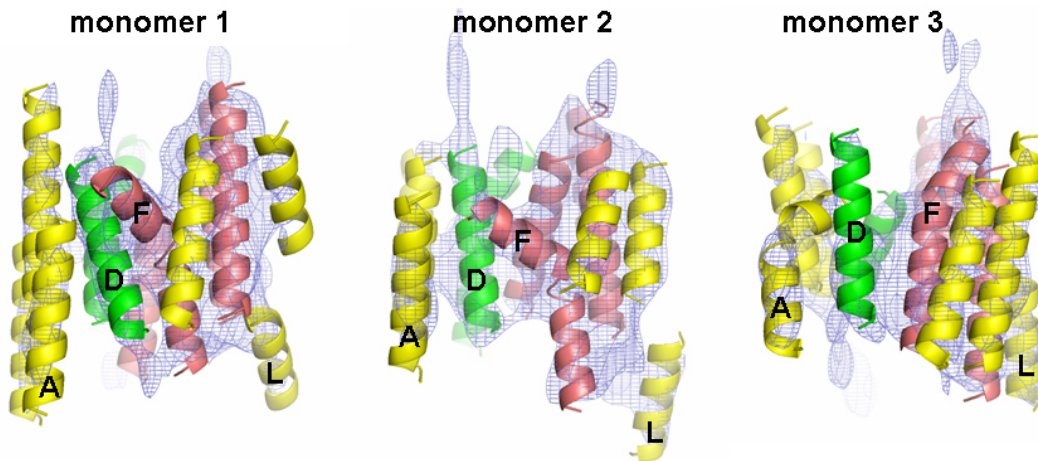
+2 to +10 angstrom



-6 to +2 angstrom



-14 to -6 angstrom



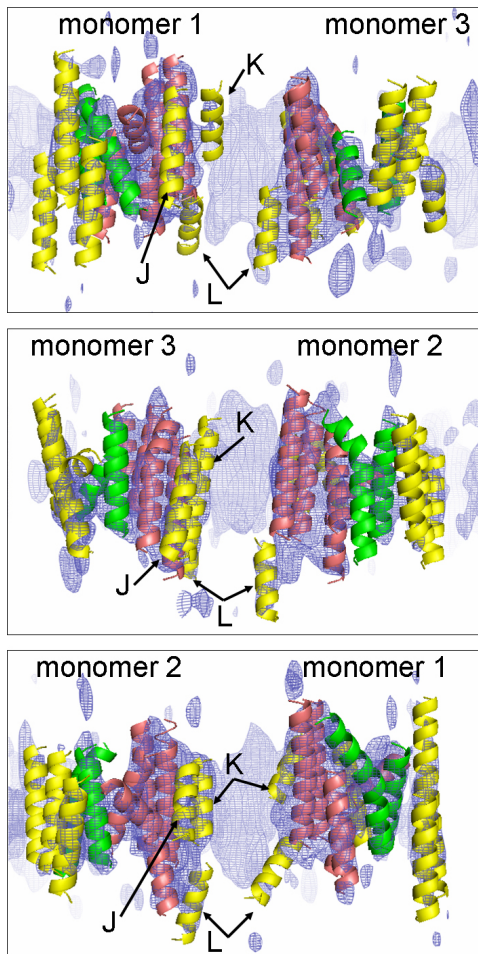
**Figure 46. Side views of the three monomers aligned in the same orientation.** Monomers 1-3 are aligned and view from the same direction. Helices A, D, F, and L are labeled.

From the side views of the three monomers (Figure 46), monomer 3 is reminiscent of a funnel open at the top, while monomer 1 and 2 are similar to one another with helix F bending to the left side. While monomer 1 shows the highest density among the three monomers, monomer 3 exhibits only 70% of the density of monomer 1. It indicates a flexible conformation of monomer 3. To define which side of the membrane faces the cytoplasm, a direct diagnosis would be the density of the long N-terminus. However, the density of the N-terminus was not observed in the 3D map. This is most likely due to the high flexibility of the hydrophilic domain and the absence of crystal contacts on the membrane surface as in 3D crystals.

### **Monomer-monomer interface**

The monomer interface is formed by the three relatively short helices J, K, and L near the pseudo-threefold axis. Helices K and L of monomer 1 showed weak densities which could only be visualized properly by displaying the density map at a low  $\sigma$  cut-off of 1.3. Helix K was more or less parallel to H in monomer 3, but tilted  $\sim 15^\circ$  in monomer 2, and  $\sim 30^\circ$  in monomer 1. Helix K was better resolved in monomer 3 (25 a.a.) than in monomer 1 and 2 (15 a.a.). This indicates that helix K is less mobile in monomer 3 than in monomers 1 and 2. The densities of K and L in monomer 1 were poorly defined, possibly due to a higher degree of flexibility.

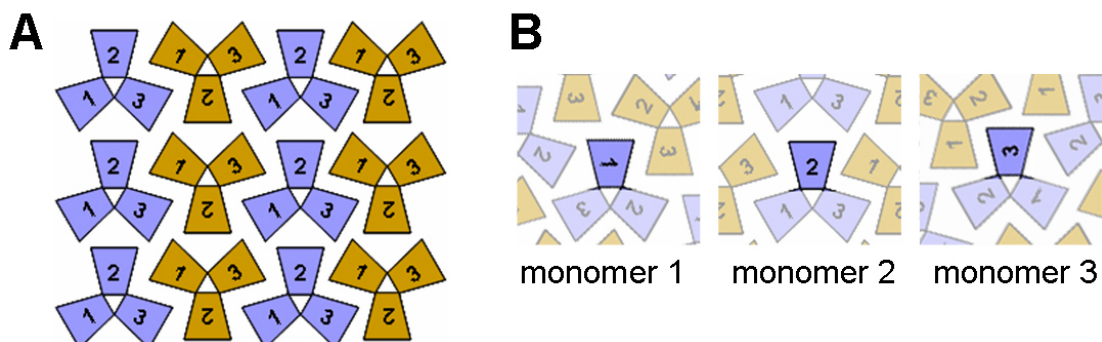




**Figure 47. Side views of the monomer interface**  
The density map is contoured at  $\sigma$  1.5.

Helices J, K, and L were located more or less at the same positions in all three monomers. The slight shift of the helices may be due to the movements of helices H and I in the central region. This shift in position might also result from different interactions at the monomer-monomer interface. The size of the interface in the center of the trimer was about 17-20 Å in diameter.

### Crystal contacts



**Figure 48. Crystal contact of monomers 1, 2, and 3.**  
(A) Overview of crystal contacts.  
(B) Individual crystal contacts of monomers 1, 2, and 3.

The crystal contacts were defined by helices A-C (Figure 38). Helices A,

---

B, and C were straight helices, except helix A in monomer 3 which showed a bend. The crystal contacts in each monomer appeared different (Figure 48).

In Figure 47B, monomer 1 had crystal contacts via helices A-C to two adjacent monomers (yellow) facing the opposite side of the membrane within  $\sim 10$  Å. In monomer 2, helices A-C had crystal contacts shared by monomers 1 and 3 which faced the same side of the membrane (blue) within a distance of 9-19 Å. In monomer 3, the crystal contacts were similar to those in monomer 1, but the adjacent monomers had different orientation.

An effective distance to influence the positions of atoms is less than 5.5 Å, based on Nuclear Overhauser Effect. Since the distance between trimers is more than 7 Å, different crystal contacts are probably not the cause of conformational changes of each monomer. Besides, lipids are most likely filling the space between trimers.

---

## 4. Discussion

### 4.1. Evaluation of protein sample quality

Protein expression of BetP $\Delta$ C45 is successfully performed in *E. coli* BL21 (DE3) and C43 strains by using a pASK-IBA5 vector. BetP $\Delta$ C45 expressed less efficiently than BetP WT when the protein yield after protein purification was compared. This is not due to inefficient binding of BetP $\Delta$ C45 to *Strep*-Tactin column since the *Strep*-tag is linked to the long hydrophilic N-terminus of BetP. Hence, it is likely that the C-terminal truncation results in lower expression of BetP.

#### Oligomeric state

It has been previously reported that BetP WT forms a trimer in 2D crystals (Ziegler, Morbach et al. 2004). Projection structure and 3D map of BetP $\Delta$ C45 also show a trimeric structure in 2D crystals. A BetP $\Delta$ C45 monomer has 558 amino acids including the *Strep*-tag, corresponding to 59.6 kDa. Therefore, a BetP $\Delta$ C45 trimer should have a molecular weight of 178.8 kDa. Blue native gel electrophoresis indicates a molecular weight of ~ 319 kDa for BetP $\Delta$ C45. This is most likely due to the tightly bound detergents and lipids after protein purification, accounting for the increase of mass. It is not unusual for membrane proteins in blue native gel electrophoresis to have roughly twice the calculated mass from amino acid sequence (Vinothkumar, Raunser et al. 2006).

#### Protein sample for 2D crystallization

It was critical to concentrate protein samples by using a high molecular weight cut-off of 100 kDa in order to avoid concentrating the detergent. Detergents in solution form micelles when the concentration is above the CMC. By using a Centricon concentrator with a molecular weight cut-off of 50 kDa, DDM micelles in the protein sample do not pass through the dialysis membrane, resulting in concentrating DDM as well. Thus, a protein sample containing > 0.1 % DDM tended to form aggregates during crystallization. It indicates that 2D crystals can only be formed with a certain detergent concentration at the starting point and that an optimal protein-lipid-detergent



---

mixture is required.

## 4.2. 2D crystallization

### 4.2.1. Optimization of crystallization conditions

**LPR:** The LPR has been reported to be one of the most important parameters in achieving successful crystallization (Schmidt-Krey, Lundqvist et al. 1998; Schmidt-Krey, Haase et al. 2007). An LPR of 0.15 (w/w) was found to be an optimal ratio to grow 2D crystals of BetP $\Delta$ C45 regardless of lipids from different sources used.

**Divalent ions:** BetP $\Delta$ C45 forms 2D crystals with better quality in the presence of Mg<sup>2+</sup> or Ca<sup>2+</sup>, while other divalent ions from transition metal elements only resulted in forming BetP $\Delta$ C45 aggregates. The role of divalent ions during dialysis is still not clear yet. Several divalent or trivalent ions have been reported to influence 2D crystallization of proteins, e.g. GdCl<sub>3</sub> for the Na<sup>+</sup>/H<sup>+</sup> antiporter NhaA, MgCl<sub>2</sub> for the glycerol facilitator GlpF and for the multidrug transporter EmrE (Williams, Geldmacher-Kaufer et al. 1999; Braun, Philippsen et al. 2000; Tate, Kunji et al. 2001). A possible explanation is that they change the stability of the hydrophilic region of the detergents and/or lipids, which leads to form detergent or lipid aggregates. Proteins may suffer from the lack of lipids and/or detergents and form protein aggregates.

**Substrate:** BetP $\Delta$ C45 appears to be more flexible in presence of glycine-betaine during detergent removal. Freeze fracture microscopy reveals that BetP $\Delta$ C45 still reconstitutes into lipid bilayers, but does not form well-ordered crystalline arrays. This suggests that glycine-betaine does not act as an inhibitor which might stabilize BetP $\Delta$ C45 conformation, but disturbs its lower energy state into a higher energy state.

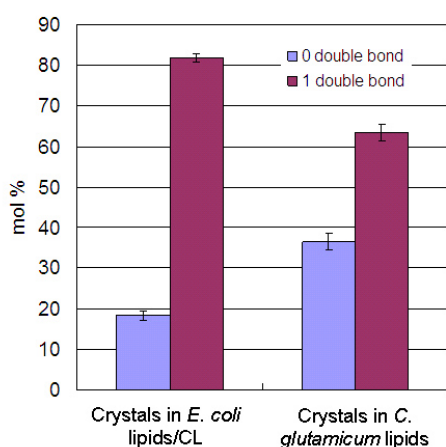
**Temperature and lipids:** Dialysis temperature is a critical parameter to achieve tightly-packed protein reconstitution into lipid bilayers. It is related to the lipids used for protein reconstitution. Each lipid species has its own transition temperature which determines the fluidity. The phase transition temperature is dependent on the saturated/unsaturated fatty acid chains of

---

lipids. It has been reported that the dialysis temperature for 2D crystallization should be close to the transition temperature of lipids (Mosser 2001; Schmidt-Krey, Haase et al. 2007; Signorell, Kaufmann et al. 2007). If a lower temperature is used, then it usually leads to protein/lipid aggregation. This phenomenon is also observed in BetP $\Delta$ C45 crystallization as dialysis below 30°C leads to protein aggregates when either *C. glutamicum* lipids or a mixture of *E. coli* lipids/bovine CL is used.

#### 4.2.2. Tubular 2D crystals

For 2D crystallization, morphology normally is not a parameter that can be predicted or controlled systematically for every membrane protein. Tubular crystal formation of BetP $\Delta$ C45 can be controlled by varying the concentration of LiCl or KCl in the dialysis buffer. It seems that the surface curvature of the lipid bilayer can be influenced by ionic strength using specific ions. When LiCl or KCl concentration is increased to greater than 400 mM, the surface curvature of the lipid bilayer is also increased to form tubular vesicles. A similar observation has also been published with OxIT, an oxalate transporter from *Oxalobacter formigenes* (Heymann, Hirai et al. 2003). The reason why it does not form smaller vesicles but tubular vesicles can be explained by 2D packing of protein molecules. The elongated shape of tubular vesicles has a fixed relative angle to the protein lattice. Therefore, protein lattices form a spiral in tubular crystals.



**Figure 49. Saturation of the fatty acid chains in 2D crystals**

In addition, the width of tubes was influenced by the added lipids. Crystals grown with *E. coli* lipids/bovine cardiolipin and with *C. glutamicum* lipids varied in their width. The lipids in these two crystals showed a different degree of saturation of fatty acid chains: 82 mol% for using *E. coli* lipids/bovine CL and 64% for using *C. glutamicum* lipids (Figure 49). Double bonds in

---

*cis*-configuration induce a kink that can alter lipid-protein interaction and bilayer curvature. It suggests that an increasing amount of saturated fatty acid chains facilitate a lower crystal curvature.

### 4.2.3. Morphology and resolution

Large specimens are favorable for data collection no matter what morphology they are. Tubular crystals grown with *C. glutamicum* lipids diffracted more poorly than sheets, although these two morphologies had the same unit cell dimensions and protein-protein contacts. The reduced resolution of the tubes could be due to the anisotropy of “bent” crystal lattices, while sheets are more uniform. Membranes of tubular crystals are more curved than those of sheet-like crystals. The high membrane curvature might also stress the interaction between protein molecules, leading to loss of resolution. A similar situation was observed with OxIT, where sheets diffracted to 3.4 Å while tubes only reached a resolution of 6 Å. The sheets have a tighter packing than the tubes, even though these two morphologies have the same symmetry  $p22_12_1$  (Heymann, Hirai et al. 2003).

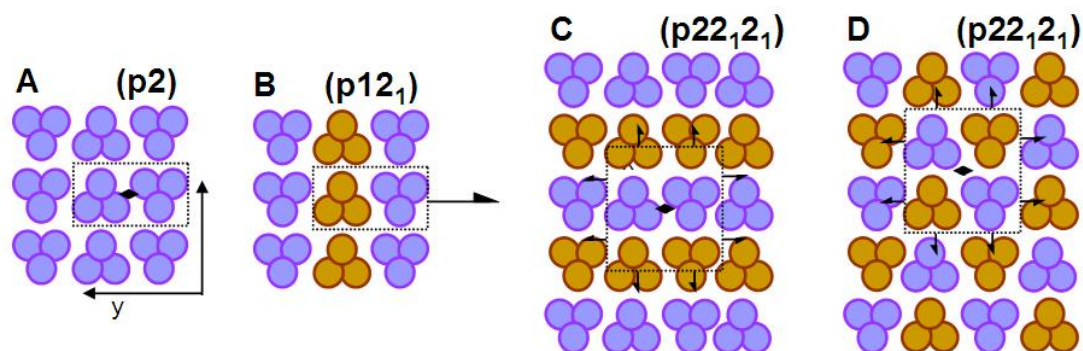
## 4.3. Role of different lipids in crystallization

BetP $\Delta$ C45 was crystallized in the presence of three different lipid systems: natural *C. glutamicum* lipids, synthetic PG 16:0-18:1 and a mixture of cardiolipin from bovine heart and *E. coli* lipids. At first glance, the choice of lipids does not seem to be critical for a successful 2D crystallization because all lipids resulted in diffracting crystals with a comparable resolution (10-7 Å). In spite of their differences, all three lipids show more or less the same molecular arrangement of BetP. On closer examination, the properties of lipids changed the quality of the 2D crystals significantly. Specific lipids seem to play an essential role in forming well-ordered 2D crystals of BetP $\Delta$ C45.

### 4.3.1. Pseudo crystals in *E. coli* lipids/bovine CL mixture

More than 99 % of the 2D crystals in *E. coli* lipids/bovine CL showed a mirror-symmetric shape of a monomer within a trimer. In a rectangular unit cell of 90.3 Å  $\times$  152.0 Å, the only possible space group would be either  $p2$  or

p12<sub>1</sub>\_b since only two BetPΔC45 trimers were allowed to fill the space of a unit cell (Figure 49A, B). A proposed space group p12<sub>1</sub>\_a however has a rotation axis along X direction, which would fit to the mirror-symmetric plane (the XZ plane) inside a trimer. Another proposed symmetry p22<sub>1</sub>\_a could only describe a unit cell containing 4 asymmetric units. So, two BetPΔC45 trimers in a unit cell representing 4 asymmetric units mean that a “half” trimer is an asymmetric unit in this case. This half trimer is generated by cutting a complete trimer through the mirror-symmetric plane (the blue dashed line in Figure 19). These contentions suggest that the mirror symmetry in a trimer may be due to averaging the density from BetPΔC45 trimers inserted randomly right side up or upside down into the crystal lattice. To deconvolute the mirror-symmetric density, a bigger unit cell (180.6 Å × 152.0 Å) was applied for 2 × 2 trimers in a unit cell, even though reflections of odd orders along the h axis ( $h = 2n+1$ ) were not observed in the optical diffraction as would be required for the larger unit cell. For the unit cell size which contained 2 × 2 trimers, the space group of p22<sub>1</sub>2<sub>1</sub> was the only possibility (Figure 50C, D). The space groups of p12<sub>1</sub>\_a and p22<sub>1</sub>\_a were possible only if the 2D crystals contained two stacked membranes, because of the rotation axis parallel to the membrane plane. In the projection map, the mirror symmetric plane could still be recognized in the trimer density.



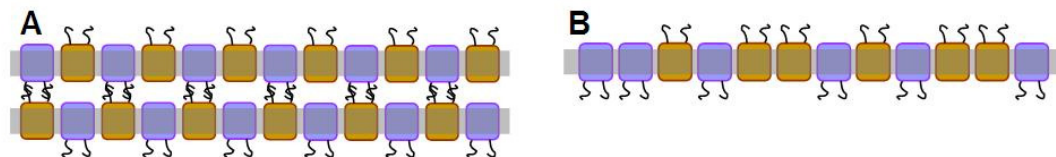
**Figure 50. Possible space groups of a single-layered BetPΔC45 crystal with a rectangular unit cell**

Different colors of the trimers represent facing to the different side of the crystal membrane, Several features are shown: a single unit cell (black dot lines), 2-fold axes perpendicular to the membrane (black oval), and screw axes in the plane of the membrane (half arrows).

It was found that the mirror symmetric trimer density could not be deconvoluted by expanding the unit cell by image processing. There are three possible reasons causing the mirror symmetry: (1) stacked lattices from

---

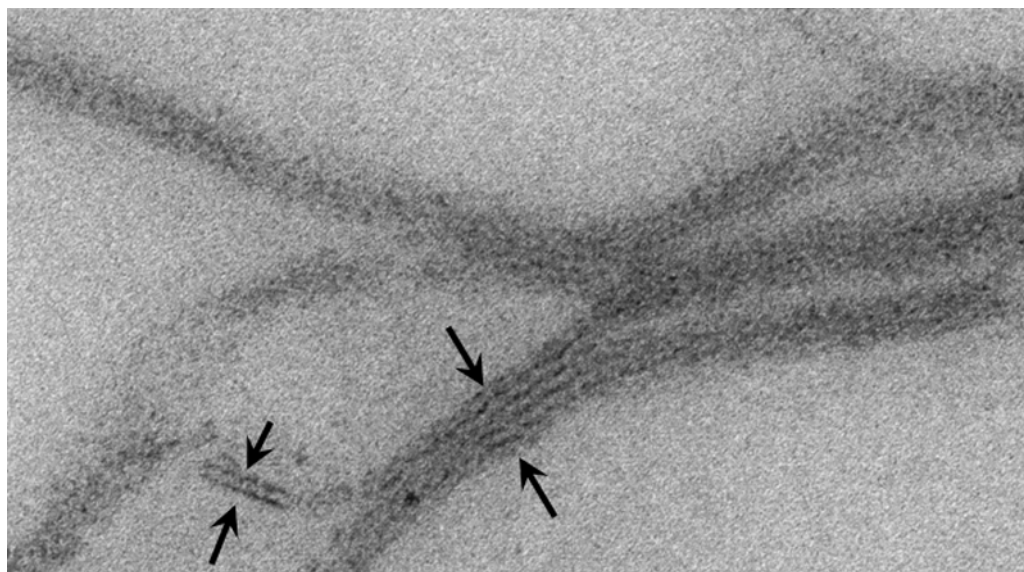
two or more crystal membranes (Figure 51A); (2) pseudo crystals with BetPΔC45 trimers inserted randomly into crystal lattices (Figure 51B); (3) small patches of well-ordered crystals. By freeze fracture electron microscopy, regularly stacked membranes were not found. Thin section through the membrane crystals showed that BetPΔC45 crystals tended to stack, but there is no regular long range order in the Z direction (Figure 52). To clarify if the mirror symmetry was caused by averaging many small crystalline patches, partitioned areas at different corners of a scanned raw image were processed individually. This procedure may enhance the signals from one single crystal patch. This method also showed that the mirror symmetry remained in every partitioned image. Therefore, it is very likely that BetPΔC45 forms pseudo crystals, where the protein is densely packed in the XY plane, but randomly oriented up and down with respect to the membrane plane (Figure 51B).



**Figure 51. Possible explanation for the averaged density of the 2D crystals**

(A) two membranes stacking

(B) Proteins lose the orientation along Z axis, even though they formed regular packing in the XY plane.



**Figure 52. Thin section through the membrane of 2-D crystals in *E. coli* lipids/bovine CL.**

It shows that 2D crystals tend to stack up to several layers, but these membranes did not show regular stacking in the Z direction.

---

Apart from pseudo crystals, BetPΔC45 did occasionally form well-ordered crystals in *E. coli* lipids/bovine CL. Four possible space groups were suggested, and p22<sub>1</sub>2<sub>1</sub> was chosen to apply the symmetry. It describes the spatial relations for 4 asymmetric units, while p2, p12<sub>1</sub>\_a, and p12<sub>1</sub>\_b only describe for two asymmetric units. These crystals also diffract better than the pseudo crystals up to 6.5 Å. Unfortunately, this crystal form was not reproducible and occurred together with the predominant pseudo crystal form. Varying the proportion of bovine CL for crystallization was also not helpful to facilitate p22<sub>1</sub>2<sub>1</sub> crystal formation. In the end, only two among 1000 crystals showed this well-ordered lattice. Because of its low probability, pursuing this crystal form for 3D map reconstruction was not an option, even though it was well-ordered.

#### **4.3.2. Well-ordered crystals in PG 16:0-18:1 and in *C. glutamicum* lipids**

From the results of ALLSPACE, crystals grown in *C. glutamicum* lipids and PG 16:0-18:1 showed a proper crystallinity compared to the crystals grown in *E. coli* lipids/bovine CL. The crystals in *C. glutamicum* had undoubtedly the best crystal quality among the three crystal forms, which diffracted to 7-8 Å. However, crystals grown in PG 16:0-18:1 showed a lower resolution (12 Å) even though the space group calculation (ALLSPACE) suggested that these were well-ordered crystals. The loss in resolution and intensity of spots is most lightly due to loose packing and/or small patches of crystalline areas, even though the specimen can grow up to 5 μm. In terms of crystallinity, PG 16:0-18:1 helped BetPΔC45 to form well-ordered crystals because higher phase residuals were obtained of for p2 and p222<sub>1</sub>\_a compared to crystals in *E. coli* lipids/bovine CL. This indicates that proteins were selective to the handedness of their neighbors. Although p2 and p222<sub>1</sub>\_a were proposed to be possible symmetries, this might be due to a lack of high resolution data, which were needed to tell the handedness. Therefore, PG 16:0-18:1 and *C. glutamicum* lipids are suggested to be the key to form well-ordered crystals of BetPΔC45.

---

## 4.4. BetP $\Delta$ C45 and lipids

Crystals grown in the presence of *C. glutamicum* lipids achieved a good quality for structure determination, while those grown in synthetic PG 16:0-18:1 formed small patches of well-ordered crystals, and those in *E. coli* lipids/bovine CL formed pseudo crystals. Because the arrangement of protein was identical in all three cases, a quantitative analysis on the crystallization behavior of BetP ascertained the influence of lipids in the 2D crystallization process. Understanding the role of lipids not only helped to improve the crystal quality, but also to learn more about the alchemy of crystallization. Especially, it is interesting in a more general way to note the role of functionally important lipids in crystal formation.

### 4.4.1. Role of lipids in BetP $\Delta$ C45 crystallization

The PE/PG ratio of *E. coli* lipids (75 % PE and 19 % PG) (Morein, Andersson et al. 1996) is nearly identical to that of the lipids co-purified with BetP $\Delta$ C45 (80 % PE and 17 % PG). This indicates that BetP $\Delta$ C45 does not select PG lipids to mimic the PG-rich environment of the *C. glutamicum* membrane, even though lipid exchange is facilitated in detergent-rich conditions.

Four dominant PE and PG species at  $\geq 5$  mol% were assessed before and after crystallization of BetP $\Delta$ C45 in the three crystal samples: PE 16:0-17:1, PE 16:0-19:1, PG 16:0-17:1, and PG 16:0-18:1. Compared to purified BetP protein, lipid extracts from all three crystals contained less PE and PG with the moieties 16:0-17:1 and 16:0-19:1, while PG 16:0-18:1 was enriched in all crystals (Figure 35). Since *C. glutamicum* does not synthesize PE lipids, the only source of PE is from the *E. coli* lipid extract and the expression system. In the crystals grown with *E. coli* lipids/bovine CL, PG 16:0-18:1, PE 16:0-18:1 as well as CL 16:0-18:1-16:0-18:1 were enriched compared to the purified protein. Thus, the 16:0-18:1 moieties appear most beneficial for BetP $\Delta$ C45 crystallization.

Compared to the crystals in *E. coli* lipids/CL, the well-ordered crystals grown with *C. glutamicum* lipids and with PG 16:0-18:1 contained a relatively

---

high amount of PG 16:0-18:1 (17 % and 33% respectively). The amount of PG 16:0-18:1 is critical for preventing pseudo crystal formation. Crystals grown with synthetic PG 16:0-18:1 were found to incorporate the highest amount of PG 16:0-18:1, but had the lowest resolution (12 Å). It is possible that the crystal order is influenced by the double-bond position in the 18:1 fatty acid chain and/or a lack of other lipid species from *C. glutamicum*. Double bonds in the *cis*-configuration exhibit a kink that can alter lipid-protein interactions and bilayer curvature. It is also possible that *C. glutamicum* lipids have different double bond positions in 16:0-18:1 from that of the *cis*- $\Delta$ 9-oleic acid of the synthetic PG 16:0-18:1. It is very likely that the natural PG 16:0-18:1 from *C. glutamicum* binds to BetP specifically because of the following reasons: (1) only the presence of PG 16:0-18:1 extracted from *C. glutamicum* form good crystals in terms of resolution and crystallinity; (2) PG 16:0-18:1 is the most dominant lipid species in *C. glutamicum*; in nature BetP is incorporated into a PG 16:0-18:1-rich environment; (3) synthetic PG 16:0-18:1 helped to form proper crystals, but the crystal quality was not as good as those grown with *C. glutamicum* lipids, which has 76 mol% of the 16:0-18:1 moieties.

In addition, more CL 16:0-18:1-16:1-18:1 was found in the crystals diffracting to 8 Å (grown with *C. glutamicum* lipids and with *E. coli* lipids/bovine CL) than in the crystals from PG 16:0-18:1. This implies that CL 16:0-18:1-16:0-18:1 improves crystal order, resulting in better resolution. Surprisingly, no CL 18:2-18:2-18:2-18:2 was detected in the 2D crystals grown with *E. coli* lipids/bovine CL, even though an excess of this bovine CL was added. From our experience, CL 18:2-18:2-18:2-18:2 is needed together with *E. coli* lipids to form large sheet-like BetP $\Delta$ C45 crystals (in low salt conditions). Since it is not incorporated into crystal membranes, it must form either protein-lipid aggregates which are not organically extractable, or empty membranes which were removed during washing steps. By monitoring lipid composition before and after crystallization of BetP $\Delta$ C45, our results show that the main criterion for lipid selection is the acyl chain but not the head group, while crystallization behavior depends on both elements.



---

#### 4.4.2. Role of cardiolipin in osmoadaptation

The total amount of negatively charged lipids (PI, PG and CL) found in *C. glutamicum* membranes was approximately 83 mol%, including a substantial fraction, 32 mol% of CL. In a previous report, the *C. glutamicum* membrane contained 87 mol% PG and only 5 mol% of CL (Hoischen and Krämer 1990). This discrepancy might be due to the different experimental methods involved or to our use of a mutant *C. glutamicum* strain (*CglΔotsAΔtreSΔtreY*) that lacks the cell wall peptidoglycan layer (Wolf, Krämer et al. 2003). This strain is more sensitive to growth stress, which could be a potential reason for enhanced CL synthesis (Özcan et al., 2007). A similar effect was observed in *Rhodobacter sphaeroides*, which responds to osmotic stress by increasing the amount of CL in the membranes (Catucci, Depalo et al. 2004).

#### 4.4.3. Chill activation in 2D crystallization

The influence of *C. glutamicum* lipids within the crystals can be deduced from the importance of temperature during 2D crystallization. When BetPΔC45 and *C. glutamicum* lipids were incubated below 15°C, only aggregates were obtained after detergent removal; the mixture required incubation at about 22°C to produce well-ordered 2D crystals. In contrast, incubation at temperatures between 4°C and 25°C with *E. coli* lipids/bovine CL did not affect 2D crystal formation. In our experience, the incubation of BetP and lipids before detergent removal is very important for generating an equilibrated ternary protein-lipid-detergent system in order to prevent immediate aggregation. Although the importance of the dialysis temperature has been reported for several other 2D crystallizations (Engel, Hoenger et al. 1992; Hasler, Heymann et al. 1998; Schmidt-Krey, Lundqvist et al. 1998; Zhuang, Prive et al. 1999; Heymann, Hirai et al. 2003; Schmidt-Krey, Haase et al. 2007), incubation temperature is rarely mentioned. Besides, the incubation temperature was only restricted when using the natural lipids of *C. glutamicum*, which likely reflects specific interaction between BetP and the lipids. In previous reports, BetP expressed in *C. glutamicum* is activated to transport glycine-betaine below 15°C even without any external osmotic stress. In contrast, chill activation does not occur when BetP is expressed in *E. coli* cells (Morbach and Krämer 2005; Özcan, Krämer et al. 2005) and no

---

effect of incubation temperature was observed in using the mixture of *E. coli* lipid extract/bovine CL or pure PG 16:0-18:1. We propose that these temperature requirements of incubation correspond to the chill activation observed in vivo.

#### **4.4.4. Functional lipids for crystallization**

Many membrane proteins have been successfully crystallized without using lipids from the native source. However, none of these proteins have been reported to display a functionally related lipid-protein interaction. The question arises: how important are the lipids from the native source for crystallization if the lipid-protein interaction is related to the function of the protein?

Most reported membrane protein crystals were grown in synthetic PC lipids (Schmidt-Krey, Lundqvist et al. 1998; Koning, Keegstra et al. 1999; Chami, Pehau-Arnaudet et al. 2001; Heymann, Hirai et al. 2003; Gonen, Cheng et al. 2004) or in *E. coli* polar lipids (Hasler, Heymann et al. 1998; Williams, Geldmacher-Kaufer et al. 1999; Collinson, Breyton et al. 2001; Hacksell, Rigaud et al. 2002) especially if they originated from *E. coli*. Crystallization with PG and CL is not reported or generalized for most of these membrane proteins. However, the choice of lipids must be taken into account if lipid-protein interaction affects protein function. If the protein function is lipid-dependent, the protein naturally adapts to the membrane in the original organism. For example, the light harvesting complex (LHCII) has 3 PG and 3 digalactosyl diacyl glycerol (DGDG) molecules bound to the protein trimer (Standfuss, Terwisscha van Scheltinga et al. 2005). Removal of PG lipids destabilizes the trimeric state (Nussberger, Dörr et al. 1993) because they bind at the interface of adjacent monomers. Specifically bound lipids were also observed in X-ray structures of the bacterial reaction center and cytochrome c oxidase (McAuley, Fyfe et al. 1999; Camara-Artigas, Brune et al. 2002; Shinzawa-Itoh, Aoyama et al. 2007). In contrast, 2D crystals of aquaporin-0 (AQP0) grown in *E. coli* lipids and in dimyristoyl phosphatidylcholine (DMPC) show the same packing; the EM structure of those grown in DMPC show nine DMPC molecules per monomer, which

---

occur on the tetramer-tetramer interface. AQP0 is not reported to have specific lipid-protein interactions or high-affinity lipid-binding sites (Gonen, Cheng et al. 2005). The nine lipids filling the interfacial space between AQP0 tetramers do not play any functional role. By contrast, the osmo- and chill-activation of BetP is lipid-dependent (Peter, Burkovski et al. 1996; Rübenhagen, Rönsch et al. 2000; Özcan, Krämer et al. 2005). In addition to the biochemical data, we also observed that only excess PG 16:0-18:1 leads to non-pseudo crystallinity of BetP $\Delta$ C45, and that incubation temperatures are related to the lipids used for crystallization. These two observations indicate that specific interactions exist between BetP and lipids. In 2D crystallization, *C. glutamicum* lipids facilitate well-ordered packing (compared to the *E. coli* lipids/bovine CL) and improve the resolution compared to PG 16:0-18:1. Our results show that the use of lipids from the original organism can be crucial to the crystallization of a protein which is functionally related to lipids.

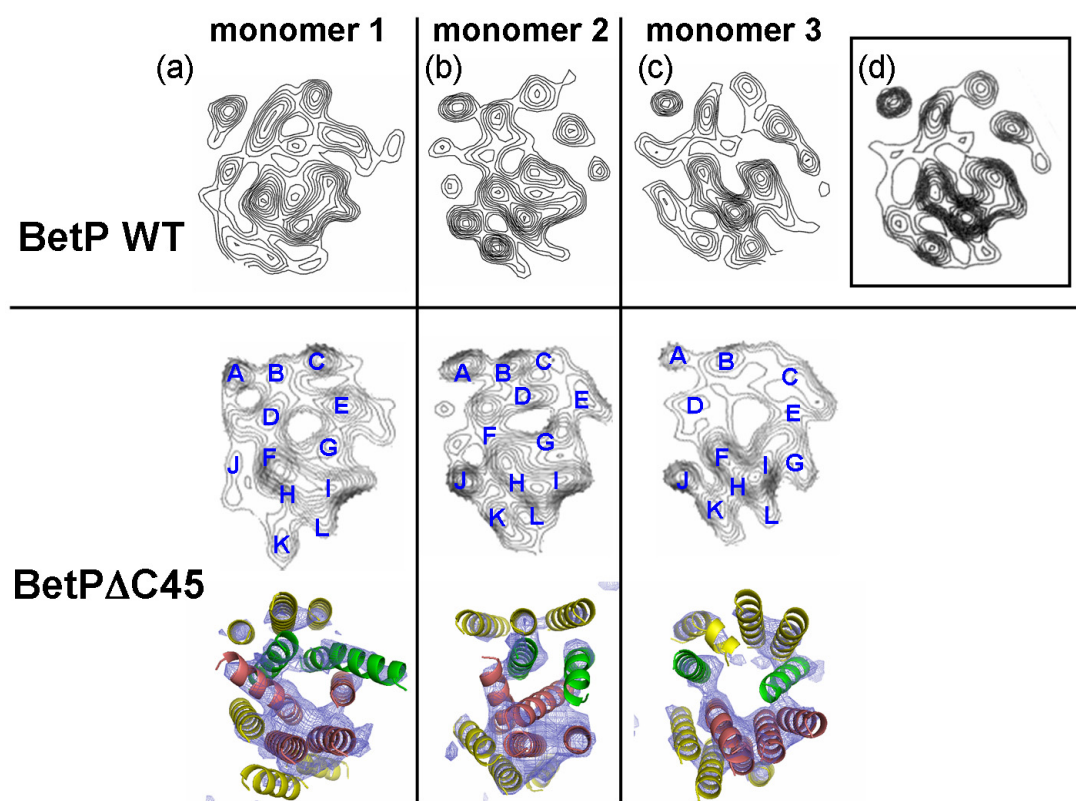
#### **4.5. 3D structure of BetP $\Delta$ C45**

The most interesting aspect of the 3D map of BetP $\Delta$ C45 is the observation of different conformations of three individual monomers simultaneously in the 2D crystals. The 3D map demonstrates that: (a) each monomer shows different densities, (b) each monomer has a different cavity size and shape, and (c) monomers 1 and 2 have similar helix arrangements, while monomer 3 shows significant shifts of helices near the central cavity. An indirect test, enforcing non-crystallographic threefold averaging, also proved that the three monomers are different near the central cavity area. Based on these evidences, it can be concluded with confidence that each monomer has different conformation from one another.

##### **4.5.1. Comparison of BetP $\Delta$ C45 and BetP wild type**

From the transport assays of purified proteins reconstituted into liposomes, BetP $\Delta$ C45 mutant loses osmoregulating ability, indicating that this mutant is constitutively active (Schiller, Rübenhagen et al. 2004). The crystals used for structure determination were obtained under similar conditions as those for proteoliposome preparation. Therefore, these three conformations

most likely reflect different functional states. To clarify the difference between BetP WT and BetP $\Delta$ C45, the BetP WT projection structure of and the BetP $\Delta$ C45 3D map were compared. From the reported projection structure of BetP wild type (Ziegler, Morbach et al. 2004) (Appendix V), the protein shows less significant differences in monomers than BetP $\Delta$ C45 (Figure 53, Appendix VI). The projection structures of the WT BetP monomers are similar enough to apply NCS averaging (Figure 53(d)). All the BetP WT monomer structures before and after enforcing 3-fold symmetry are more similar to the monomers 1 and 2 of BetP $\Delta$ C45 than monomer 3. This indicates that monomer 3 is very likely the conformation causing glycine-betaine leakage. It raises the question: why would the C-terminal truncation cause this leakage conformation?



**Figure 53. Comparison of 7.5 Å projection structure of BetP WT (Ziegler, Morbach et al. 2004) and the projection view (8 Å) of BetP $\Delta$ C45 3D map**

Monomer 1 (a) and monomer 3 (c) in the BetP WT projection map are rotated  $\pm 120^\circ$  to be aligned to monomer 2 (b). The subfigure (d) shows the averaged density from monomers 1, 2, and 3 with 3-fold symmetry enforced. The density map of BetP $\Delta$ C45 is displayed at 1.5  $\sigma$  cut-off.

As mentioned earlier, the C-terminus carries mainly positively charged

---

residues. At the neutral pH, the C-terminus is assumed to attach to the membrane, working as an osmosensor via the interaction with the cell membrane. Without this interaction, protein can be considered to be in the “transporting state”, which has the conformation other than BetP WT. Monomer 3 of BetP $\Delta$ C45 is most likely to be this “transporting state”.

#### 4.5.2. Asymmetric trimer of BetP $\Delta$ C45

Map intensity is related to conformational flexibility and stability of molecules (Phillips, Fillers et al. 1980). Since monomer 1 shows the strongest density and monomer 3 the weakest, it indicates that the conformation of monomer 1 is most stable, followed by monomers 2 and 3. If they had the same stability, the 3D map would have shown the same intensity for each monomer. Even if different conformations are randomly packed in crystals, the discrepancy between different conformations would be averaged out by merging; in total, about 1 million trimers were averaged from 79 images. In the BetP $\Delta$ C45 3D map, these three monomers are not identical to each other, so different conformations are most likely well-ordered in crystals. Since we observe different intensity for each monomer after merging, these monomers most likely show different stability and conformations. Therefore, this is a further indication that BetP $\Delta$ C45 is an asymmetric trimer.

How are different conformations preserved in the crystals? From the literature, trimeric proteins in 2D crystals usually have a crystal packing with a threefold symmetry (Table 16) and a unit cell of 120° between the *a* and *b* axes. In the crystal forms of threefold symmetry, each monomer has the same crystal contact with adjacent trimeric proteins and shows the same structure after applying the threefold symmetry. By contrast, BetP never packed into crystals with threefold symmetries; in this way, BetP appears to be unusual for a trimeric protein. Instead, BetP tends to form crystals with a rectangular unit cell in symmetry p12<sub>1</sub>\_b, p22<sub>1</sub>2<sub>1</sub> or the pseudo crystal form, where the monomers from a trimer do not have identical crystal contacts. Is it different crystal contact causes different conformation of these monomers, or different conformations cause the non-threefold symmetry in the crystals? From the 3D map of BetP $\Delta$ C45, a trimer is ~10 Å away from its adjacent

trimers. At this distance, it is unlikely to cause any conformational changes for neighboring molecules. The space between trimers is filled with lipids, which do not show up in the map due to limited resolution. It implies that different conformations of BetP $\Delta$ C45 cause non-p3 type crystal packing.

Protein	Crystal	Symmetry	Reference
Light harvesting complex II (LHCII)	2D	p32 <sub>1</sub>	(Kühlbrandt 1988)
Microsomal glutathione transferase	2D	p6	(Schmidt-Krey, Murata et al. 1999)
Membrane-bound annexin A5	2D	p32 <sub>1</sub>	(Oling, Santos et al. 2000)
Carnitine transporter (CaiT)	2D	p3	(Vinothkumar, Raunser et al. 2006)
Glutamate transporter from <i>Pyrococcus horikoshii</i> (Glt <sub>ph</sub> H7)	3D	p6 <sub>1</sub>	(Yernool, Boudker et al. 2004)
Ammonia channel (AmtB)	3D	p6 <sub>3</sub>	(Khademi, O'Connell et al. 2004)
Multidrug efflux pump (AcrB)	3D	R32	(Yu, McDermott et al. 2003)

**Table 16.** Trimeric membrane proteins and their crystal symmetry in 2D or 3D crystals

The multidrug efflux pump AcrB is an analogous example exhibiting different monomer conformations and the crystal symmetry. Two crystal forms of AcrB have been obtained: R32 and C2. The R32 crystal form has the crystallographic threefold symmetry, and each monomer has the same structure. By contrast, the AcrB monomers in the C2 crystal form show crucial differences in their conformations (Murakami, Nakashima et al. 2006; Seeger, Schiefner et al. 2006). It can be concluded that non-p3 type crystal forms are due to different conformations of monomers of a trimeric protein. Since BetP crystals have so far not obtained in a p3 type symmetry, it indicates that BetP is possibly not a symmetric trimer in nature, where all three monomers would be identical.

Besides, the presence of glycine-betaine in the crystallization buffer results in a decrease of crystal order. With the presence of 5 mM glycine-betaine during crystallization, proteins seem to become more flexible and do not form crystalline arrays as confirmed by freeze fracture studies of the crystals (Figure 16). Although 2D crystals do not encounter any osmotic stress due to accesses to both sides of the membrane, the constitutively active mutant BetP $\Delta$ C45 is transporting glycine-betaine. It implies that the

---

“transporting” state is at a higher energy state, and also not favorable for crystal packing.

### **4.5.3. Tentative identification of the cytoplasmic membrane surface**

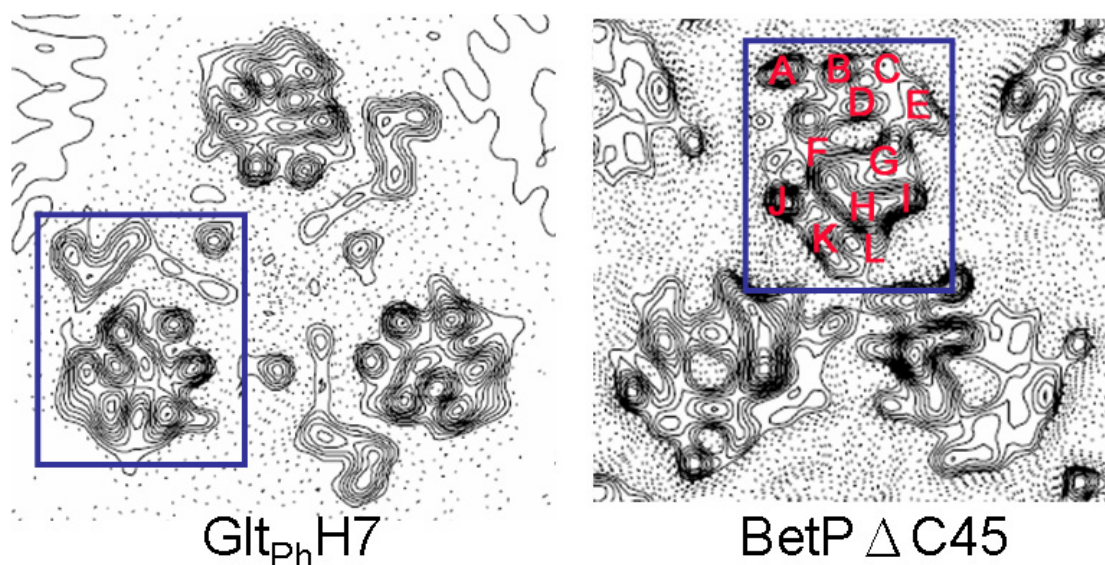
How do we know which is the cytoplasmic side of the membrane? In BetP $\Delta$ C45, there is still a long hydrophilic N-terminus facing the cytoplasm. Since the density of the N-terminus is not observed in the 3D map, the N-terminus is most likely to wobble on the crystal membrane surface without having a uniform structure in the three monomers. This is not surprising because the N-terminus consists of negatively charged residues which would result in its repulsion from the membrane. It is also possible that the N-terminus forms  $\beta$  strand, which would not be seen in the 3D map at this resolution. Therefore, there would not be any direct interaction between the membrane and the N-terminus. Although the N-terminus is not seen in the 3D map, and therefore the side of the protein could not be directly identified, we can still use indirect ways to identify it.

From the known structures of trimeric transporters, there are only two examples: the multidrug efflux pump AcrB and the glutamate transporter Glt<sub>Ph</sub>H7. AcrB can not be compared to BetP directly, because it docks to two other proteins, TolC and AcrA, forming a complex through two membranes to export drugs. The projection structures of BetP and Glt<sub>Ph</sub>H7 monomers show some resemblance in the substrate-binding cavity, even though these two proteins have different trimer contacts (Figure 54). Trimer contacts in the X-ray structure of Glt<sub>Ph</sub>H7 are mediated by three long, highly tilted proline-rich helices, which extend above the membrane toward the cytoplasm (Yernool, Boudker et al. 2004) (Table 1). The pointed tips of Glt<sub>Ph</sub>H7 monomers come together at the threefold axis in the center of the trimer at the cytoplasmic side, forming tight contacts. These proline-rich helices correspond to helix C of BetP monomers in terms of position. However, the helices involving in trimer formation of BetP are most likely helices J, K, and L, even though the density outside the membrane was not seen. The extra-membranous, protrudent parts above or below the membrane could not be seen in the 3D

---

map, due to contrast matching by glucose, which tends to cancel out the density of extra-membranous protein at this resolution (Kühlbrandt 1982; Chintalapati, Al Kurdi et al. 2008). Therefore, the density of helices J, K, or L may show only their membrane-embedded domain, while their extra-membranous segments might be involved in trimer formation.

BetP and Glt<sub>ph</sub>H7 monomers are very similar in the projection structures, e.g. BetP and Glt<sub>ph</sub>H7 show stronger density in the position of helices A-B-D bundle in BetP (the upper left corner in the boxes in Figure 54) than in the B-C-E bundle, as well as the strong density of helices F-L bundle. Based on these observations, it is assumed that the orientation of BetP with respect to the membrane plane can also be determined based on Glt<sub>ph</sub>H7 structure. Thus, it is suggested that in Figures 42 and 43 BetP is viewed from the periplasmic side but not from the cytoplasmic side. If this interpretation is correct, it also corresponds to the contact of trimer formation (helix L) is pointed to the cytoplasm (Figure 45). Other than comparing the projection structures of BetP $\Delta$ C45 and Glt<sub>ph</sub>H7, the interpretation of the cytoplasmic membrane surface can also use the stability of different conformations as an indicator (see 4.5.4.).



**Figure 54. Comparison of glutamate transporter and BetP $\Delta$ C45.**

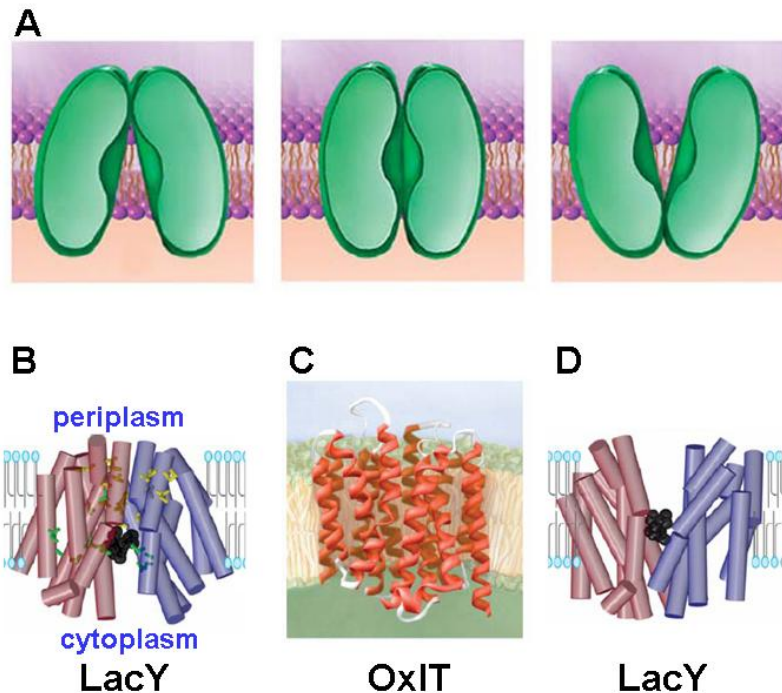
8 Å Projection density of Glt<sub>ph</sub>H7 membrane-embedded part is created from the pdb coordinate (pdb code 1XFH). The top of the Glt<sub>ph</sub>H7 projection map is the periplasmic side.



---

#### 4.5.4. Different monomer conformations

After determining the likely protein orientation, we would like to know the conformational state for each monomer. Secondary transporters utilize the free energy released from the energetically downhill movement of a cation (mainly  $H^+$  or  $Na^+$ ) in response to an electrochemical gradient to catalyze transport of substrate against concentration gradient (Guan and Kaback 2006). Two conformations of turnover are postulated: the cytoplasmically open state (C) and the periplasmically open state (P) (Jardetzky 1966) (Figure 55A). These two states describe an access of the substrate from either side of the membrane. One of the best-studied secondary transporters is lactose permease (LacY) from *E. coli*. LacY is an  $H^+$ /lactose symporter from MFS and physiologically functions as a monomer. In previous reports, the X-ray structure of LacY exhibits a single sugar-binding site at the apex of a hydrophilic cavity open to the cytoplasm (Abramson, Smirnova et al. 2003) (Figure 55B). Apart from LacY, three other secondary transporters also show a cytoplasmically open conformation: glycerol-3-phosphate transporter GlpT (Huang, Lemieux et al. 2003), mitochondrial ADP/ATP carrier (Pebay-Peyroula and Brandolin 2004), and  $Na^+/H^+$  antiporter NhaA (Hunte, Screpanti et al. 2005). These four X-ray structures of transporters show hydrophilic cavities containing the substrate-binding sites. The cavities provide access from the cytoplasm to the membrane center, but are blocked by a barrier at the periplasmic side. Up to now, none of the periplasmically open conformation with or without bound substrate or inhibitor has been observed in any crystal structure of secondary transporters. So far, only computer-based models are proposed according to biochemical data (Kaback 2005) (Figure 55D).



**Figure 55. Proposed and experimental conformations of secondary transporters** (A) three conformations of secondary transporters are proposed: cytoplasmically open, occluded, and periplasmically open (Hirai and Subramaniam 2004). (B) X-ray structure of LacY in the cytoplasmically open conformation (Abramson, Smirnova et al. 2003), (C) EM structure of OxIT in the occluded conformation (Hirai, Heymann et al. 2002; Hirai and Subramaniam 2004), and (D) simulated periplasmically open conformation of LacY (Guan and Kaback 2006)

Apart from the C and P conformations, an intermediate conformation is observed in several crystal structures. This intermediate conformation is the occluded state (O) during turnover of transporters, in which the substrate-binding cavity is not accessible from either side of membrane. This conformation is thought to be present in the 6 Å 3D map of the oxalate transporter OxIT in the presence of 100 mM potassium oxalate (Hirai, Heymann et al. 2002) (Figure 55C). OxIT is also a member of the MFS family. When compared to LacY, OxIT conspicuously shows a central cavity tapered to a narrowed opening at both the cytoplasmic and periplasmic membrane surface. This may be significant because the structure was also determined by cryo electron microscopy of 2D crystals (Hirai, Heymann et al. 2002; Hirai and Subramaniam 2004), in which a quasi-native lipid environment embeds the transporters, and this might stabilize the occluded conformation that is closed on both sides of the protein. The X-ray structures of Glt<sub>P<sub>H</sub></sub>H7 (Yernool, Boudker et al. 2004) and LeuT<sub>Aa</sub> (Yamashita, Singh et al. 2005) are both

---

funnel-shaped and open towards the periplasm, although some side chains apparently block the transport pathway towards the periplasm in the presence of bound ions, substrate, or inhibitors (Singh, Yamashita et al. 2007). For this reason, they have been interpreted to be in the occluded state.

In BetP $\Delta$ C45, monomer 1 in the section plots (Figure 45) shows an opening that can be accessed from the cytoplasmic membrane surface to the cavity. The side view (Figure 46) also shows a cytoplasmically open conformation of monomer 1. Thus, monomer 1 is attributed to the C state. Although monomers 1 and 2 are more similar to each other than to monomer 3, the differences between them are too distinct to believe that both show the same conformation. The entrances from both membrane surfaces toward the cavity in monomer 2 seem to be the same size (Figure 45). Besides, the shape of the membrane-embedded cavity seems to be identical to the cavity shape close to the membrane surfaces (Figure 45B-D). It is due to helices E and G moving inwards to the center and helices D, E, and F are nearly perpendicular to the membrane plane (Figure 43). Monomer 2 is therefore expected to be the O state of the transporter. Monomer 3 is the inverse example of monomer 1, exhibiting a gradually enlarged access from the central cavity to the periplasmic side (Figure 45). Compared to monomers 1 and 2, helix F of monomer 3 near the periplasmic side also moves aside, failing the blocking barrier at the periplasmic side of the transporter (Figure 43 and 46). Based on these observations, monomer 3 is concluded to be most likely to be the P conformation.

Like other transporters, BetP also shows a stable C conformation in monomer 1, followed by the O state in monomer 2. LacY, GlpT, and OxlT, three members of the major facilitator superfamily, also show the C and O conformations in crystals. The P conformation in monomer 3 is less stable, as suggested before in the case of LacY (Guan and Kaback 2006). It is most likely the reason why it has not been trapped in crystals even with the presence of the substrate or inhibitor.

---

#### 4.5.5. Oligomeric state and transport function of BetP

The three different monomer conformations are assigned with confidence based on the observations described above. However, there are still questions remaining: why does BetP need to form a trimer but not a monomer for substrate transport? How do monomers communicate via different conformations during the transport cycle?

Most of the known structures of secondary transporter are monomers (Hirai, Heymann et al. 2002; Abramson, Smirnova et al. 2003; Huang, Lemieux et al. 2003; Yamashita, Singh et al. 2005). In general, a simple transport mechanism can be accomplished in a monomeric transporter (Rimon, Tzuber et al. 2007), which is the case of the known structures from the major facilitator superfamily. Up to the date, only two examples showing asymmetric oligomers are reported: the multidrug efflux pumps EmrE and AcrB. EmrE needs to form a dimer in order to perform the transport function (Ubarretxena-Belandia, Baldwin et al. 2003), so it cannot be attributed to two distinct transporting states. The three different monomer conformations in AcrB show an alternating access mechanism with a substrate bound (Murakami, Nakashima et al. 2006) and without (Seeger, Schiefner et al. 2006). The substrate is taken up from the hydrophobic phase of the membrane and extruded into the aqueous medium. Such a mechanism cannot apply to BetP because glycine-betaine is a hydrophilic substrate which would be taken up from and released to the aqueous phase. Therefore, the transport mechanisms of EmrE and AcrB are most likely different from that of BetP. From blue native gel electrophoresis and ultra centrifugation, it is clear that BetP is a trimer in detergent solution. However, why does BetP form a trimer even if each monomer is capable of complete substrate transport? Since different conformations are observed in one trimer, the easiest explanation would be that the conformations are regulated by monomer-monomer interaction. Thus, this interaction implies that BetP may have a different alternating access mechanism for glycine-betaine transport from that AcrB has.

Secondary transporters are triggered by the electro-chemical gradient

---

across the membrane to transport the substrate. It is trivial that there are two translocation pathways: the one for the cation, mostly  $H^+$  or  $Na^+$ , and the other for the substrate. Based on the well-studied transport mechanism of LacY, protonation of the protein triggers the binding of substrate, followed by a conformational change from C state to P state for substrate release and deprotonation (Guan and Kaback 2006). BetP is a  $Na^+$ /glycine-betaine symporter and also equipped with two translocation pathways. The crystals for 3D map reconstruction is obtained from a dialysis buffer containing 200 mM NaCl, so it is not surprising that some resolved conformations are possibly at a sodium bound state. Since the sodium binding of the protein triggers the substrate binding, the monomer 2 in the O state is very likely sodium bound. Monomers 1 and 3 cannot be assigned because the situations with and without sodium bound are both possible for the C and P states. Even so, it would also not be surprising if all the three monomers are sodium bound in this BetP structure due of the NaCl-rich environment during crystallization and sample preparation.

This is the first time that the P state is observed in a structure of a secondary transporter. The main reason for it is the usage of BetP $\Delta$ C45. The property of being constitutively active suggests a possibility to trap this unstable conformation. On the other hand, the interaction between the C-terminus and the membrane surface seems to stabilize the conformation of the C state, which is seen in the BetP WT. According to the LacY structure, there is a proton binding site near the substrate binding site. Therefore, the residues responsible for  $H^+$  and substrate binding are located within the membrane. To apply the same binding strategy to BetP, the easiest way to interlock sodium and substrate binding would be the helix movements in the membrane-embedded region. An interaction between the C-terminus and the membrane surface would not interfere with sodium or substrate binding directly. Therefore, a possible way would be that the movement of the C-terminus influences some membrane-embedded helices, which thus facilitate sodium binding.

---

## 4.6. Prospects

The 3D structure of BetP $\Delta$ C45 shows each monomer in a different conformational state forming an asymmetric homotrimer. This not only presents the first look on a BCCT family transporter but also reveals the P state of secondary transporters for the first time.

The structure of BetP $\Delta$ C45 determined in this thesis reveals the overall structure and packing of BetP's transmembrane helices. To truly understand how BetP performs its osmosensing and osmoregulatory functions, we however need to know the structure of all its conformational states at atomic resolution. Substantial progress towards this goal has been recently achieved in our laboratory, and a higher resolution X-ray structure of an N-terminally truncated BetP mutant will soon be available. This structure will reveal many structural details like the helical arrangement, the substrate binding pocket, monomer-monomer contacts in the BetP trimer and the conformations of termini and loop regions. The lower resolution electron-crystallographic structure determined in this thesis will however be a valuable reference point for the structure of BetP in a native-like lipid environment. The comparison of both structures will also allow us to determine the orientation of BetP in a membrane context and will give valuable insights into the transport mechanism.

Even with both structures available, there will however be questions remaining to be answered. In particular I want to point out two questions I would address if I could continue the project.

### 4.6.1. Interaction between BetP and the substrate

In order to know the interaction between BetP and glycine-betaine, it is essential to know where substrates are bound to the C, O, and P states. As discussed earlier, the P state is concluded to be unstable because of the weak density observed in monomer 3. The first challenge will thus be to create a stable P state.

The original thought would be to introduce a substrate to stabilize the P

---

state. However, adding glycine-betaine to the crystallization buffers was not successful and no crystals could be formed. To trap the conformational state with substrate bound, we could take advantage of the preformed crystals by adding glycine-betaine to them shortly before freezing. If the expected relatively large conformational changes occur and do not destroy the crystal lattice, they could be followed by comparison of projection maps as has been successfully used to monitor conformational changes in the Na<sup>+</sup>/H<sup>+</sup> antiporter NhaA (Vinothkumar, Smits et al. 2005).

#### **4.6.2. Function of the N-terminus**

Transport measurements indicate that the N-terminus functions as an accelerator for osmoregulation and BetP with a truncated N-terminus can only be activated with a higher osmotic gradient. An important question to be answered would be how exactly the N-terminus performs this function. The amino acid sequence of the N-terminus contains several negative charges, and is unlikely to interact with the membrane. Due to its polarity, it is more likely to interact with the positively charged C-terminus which detaches from the membrane under high osmotic stress. The function of the N-terminus could thus be to bind and stabilize the detached conformation of the C-terminus during transition from the C state to the P state. The N-terminus is 60 a. a. and the C-terminus is 50 a. a. long, and both together are long enough to bridge the approximately 40-50 Å of a BetP Monomer. An interesting experiment would be to create a set of mutants truncating different lengths of the termini, replacing some of the charged amino acids or even reverse their polarity. A comparison of glycine-betaine uptake and response to osmotic stress in the mutants would help to clarify the regulating role of BetP's termini. If both termini in fact interact, an interesting approach could be to engineer a cross-linking disulfide bond between them to lock BetP in the P state. This would make this interesting but unstable conformational state accessible for structural investigation and could help to reveal the full transport cycle of this class of osmoregulated transporting proteins.

---

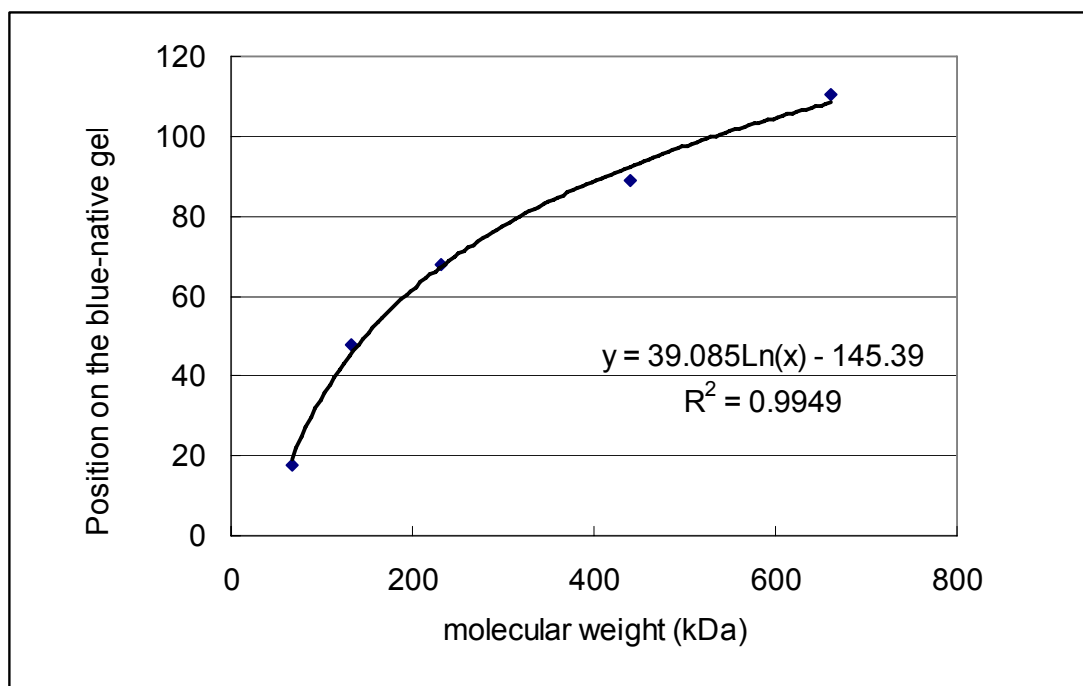
## 5. Appendix

### 5.1. Appendix I: Native gel and molecular weight

Marker (KDa)	Relative distance in the native gel (mm)
67	17.6
123	48
232	68
440	88.8
660	110.4
<b>319</b>	<b>80 (BetPΔC45)</b>

$$80 = 39.085 \ln(x) - 145.39$$

$$X = \text{EXP}[(80+145.39)/39.085] = 319.4697$$





## 5.2. Appendix II: Merging statistics

Image number	Refined tilt angle (°)	Resolution limit used for origin refinement(Å)	Phase residual (IQ 1 – 4)	EM	Magnification
2072	-4.711	12	reference image	JEOL	45 k
2081	1.128	12	25.965 (34)	JEOL	45 k
2082	2.462	12	20.048 (55)	JEOL	45 k
2073	-0.612	12	25.551 (47)	JEOL	45 k
2095	-1.327	12	18.386 (49)	JEOL	45 k
2112	5.662	12	17.060 (44)	JEOL	45 k
2093	-3.654	12	21.488 (45)	JEOL	45 k
2089	-3.109	12	21.409 (40)	JEOL	45 k
2085	3.394	12	17.820 (34)	JEOL	45 k
0426	-5.647	12	19.977 (57)	Polara	59 k
0424	-0.164	12	19.741 (55)	Polara	59 k
1194	0.788	12	18.711 (50)	JEOL	53 k
1185	3.800	12	17.259 (48)	JEOL	53 k
0631	5.807	12	24.010 (58)	JEOL	53 k
0617	-1.655	12	25.805 (61)	JEOL	53 k
2101	5.132	12	18.365 (47)	JEOL	45 k
2102	-3.719	12	20.679 (43)	JEOL	45 k
3636	-5.173	12	19.177 (48)	JEOL	53 k
2091	-1.414	12	20.550 (310)	JEOL	45 k
5611	16.392	12	29.761 (34)	JEOL	45 k
5613	-16.259	12	36.311 (32)	JEOL	23 k
5557	-17.693	12	21.721 (450)	JEOL	45 k
5587	14.178	12	23.075 (29)	JEOL	45 k
2397	16.508	12	23.898 (58)	JEOL	45 k
2389	-21.320	12	23.619 (47)	JEOL	45 k
2391	16.967	12	20.257 (49)	JEOL	45 k
2390	13.814	12	20.085 (47)	JEOL	45 k
2405	-23.847	12	23.414 (47)	JEOL	53 k
2398	-18.621	12	23.126 (47)	JEOL	53 k
2387	-19.499	12	18.316 (35)	JEOL	45 k
2370	-14.417	12	18.178 (40)	JEOL	45 k
2400	-18.239	12	25.888 (42)	JEOL	53 k
4607	-12.034	12	16.245 (46)	JEOL	45 k
2373	-18.020	12	33.184 (24)	JEOL	45 k
2392	-19.300	12	29.478 (24)	JEOL	45 k
2395	-17.243	12	25.517 (31)	JEOL	45 k
2994	-21.202	12	27.618 (23)	JEOL	45 k
3003	12.039	12	15.980 (27)	JEOL	45 k
4622	-32.989	12	13.041 (21)	JEOL	45 k
2369	-19.429	12	20.557 (40)	JEOL	45 k
2401	-18.447	12	24.800 (35)	JEOL	53 k
2995	-18.545	12	30.291 (26)	JEOL	45 k

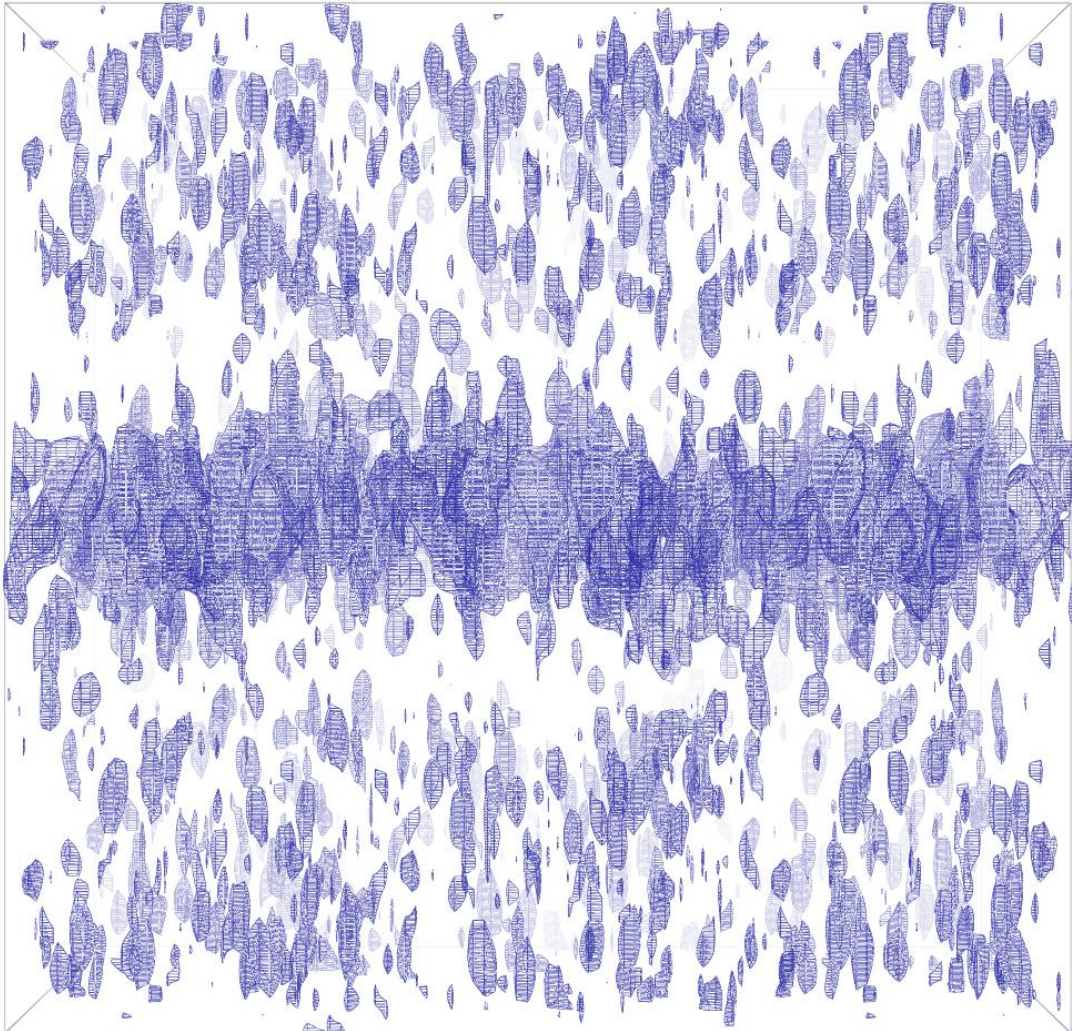
2990	-17.700	12	21.515 (26)	JEOL	45 k
2378	-22.336	12	20.081 (22)	JEOL	45 k
4635	-17.726	12	22.806 (50)	JEOL	45 k
3301	26.024	12	22.594 (52)	JEOL	45 k
3820	27.805	12	20.574 (36)	JEOL	45 k
3284	28.191	12	28.368 (30)	JEOL	45 k
3853	-29.439	12	22.906 (29)	JEOL	45 k
3300	28.148	12	28.323 (42)	JEOL	45 k
2669	-28.153	12	23.879 (35)	JEOL	53 k
3275	-26.960	12	17.599 (14)	JEOL	45 k
3852	28.400	12	23.139 (26)	JEOL	45 k
2221	25.032	12	20.031 (26)	JEOL	45 k
3296	29.634	12	27.155 (52)	JEOL	45 k
3293	28.458	12	22.416 (51)	JEOL	45 k
3285	22.047	12	20.918 (32)	JEOL	45 k
3294	29.574	12	23.969 (24)	JEOL	45 k
4356	-22.987	12	24.477 (30)	JEOL	45 k
2684	-32.103	12	16.337 (17)	JEOL	53 k
3851	29.567	12	22.789 (32)	JEOL	45 k
2239	36.188	12	10.296 (18)	JEOL	53 k
4065	49.344	15	25.623 (21)	JEOL	53 k
4066	52.029	15	16.101 (17)	JEOL	53 k
4067	52.277	15	19.739 (23)	JEOL	53 k
4077	54.360	15	27.522 (17)	JEOL	53 k
4086	65.291	15	9.739 (7)	JEOL	53 k
4097	58.600	15	30.785 (19)	JEOL	53 k
4103	49.371	15	25.238 (24)	JEOL	53 k
4105	-48.913	15	10.707 (10)	JEOL	53 k
4664	-52.429	15	27.093 (22)	JEOL	53 k
4675	-49.551	15	16.051 (16)	JEOL	53 k
4676	-51.088	15	21.905 (21)	JEOL	53 k
4677	-53.115	15	25.512 (17)	JEOL	53 k
4678	-46.275	15	22.856 (25)	JEOL	53 k
4679	-53.936	15	21.163 (20)	JEOL	53 k
4683	-48.242	15	23.465 (18)	JEOL	53 k
4689	-53.223	15	25.737 (23)	JEOL	53 k
4696	-52.353	15	27.338 (21)	JEOL	53 k

**Merging statistics of all the images used for 3D map reconstruction during origin refinement**

Phase residuals during origin refinement for all the images used for 3D map reconstruction. Different resolution cut-offs were applied to different tilt angles. Phase residuals were shown in the 4th column, and numbers in the parentheses were number of reflections used to refine the phase origin. Images were taken from a JEOL 3000 SFF or a FEI Tecnai G2 Polara microscope. The reference image 2072 showed no phase residual.

---

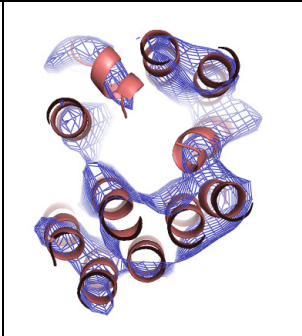
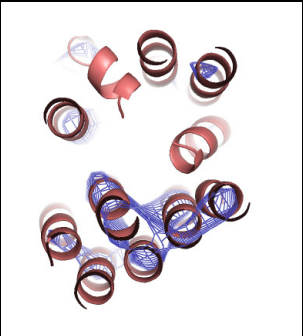
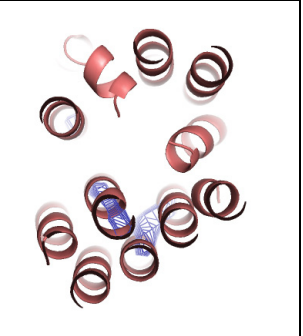
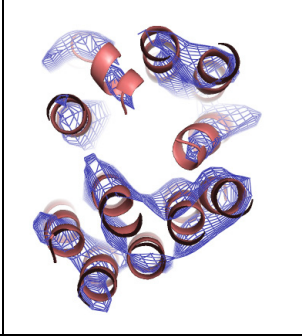
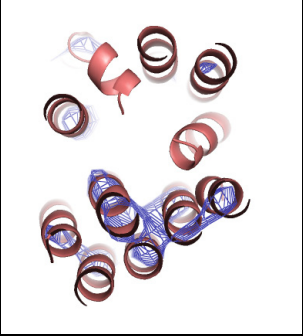

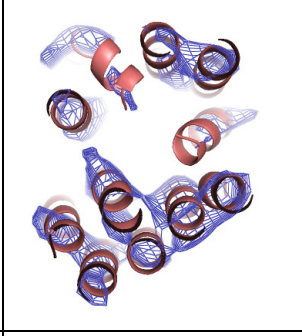
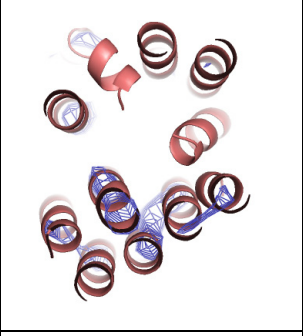

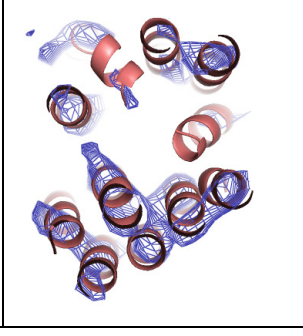


### 5.3. Appendix III: The 3D map without modifying the amplitude



**Side view of the 3D map before modifying amplitudes.**

The map is displayed with a sigma cut-off of 2.0 and a B factor of  $-300 \text{ \AA}^2$  applied.

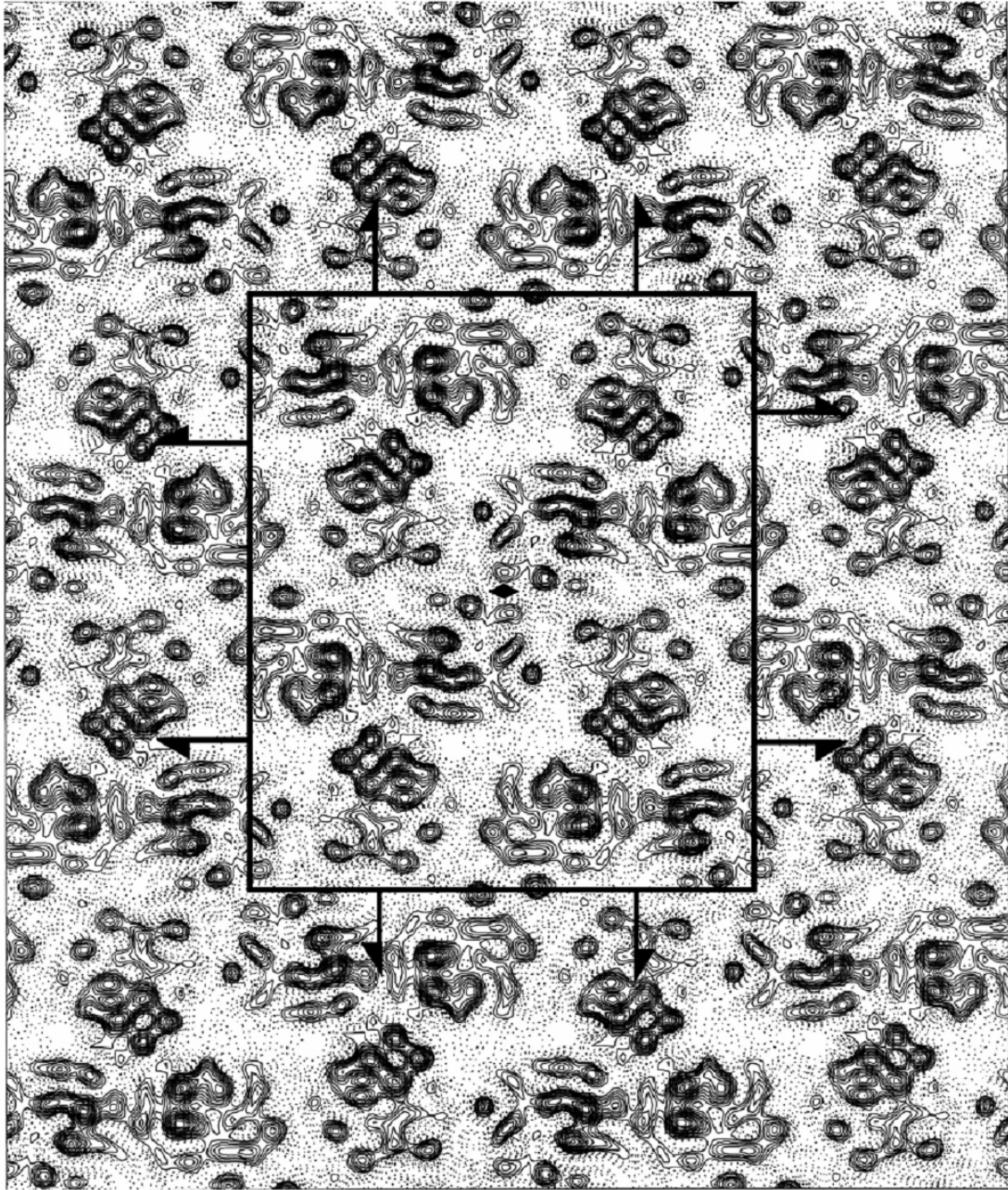
**5.4. Appendix IV: Density maps of monomer 3 with different B factors and  $\sigma$  cut-offs applied**

	2.0 $\sigma$	3.0 $\sigma$	4.0 $\sigma$
B = -300 $\text{\AA}^2$			
B = -400 $\text{\AA}^2$			
B = -500 $\text{\AA}^2$			
B = -600 $\text{\AA}^2$			



---

## 5.5. Appendix V: projection structure of BetP WT

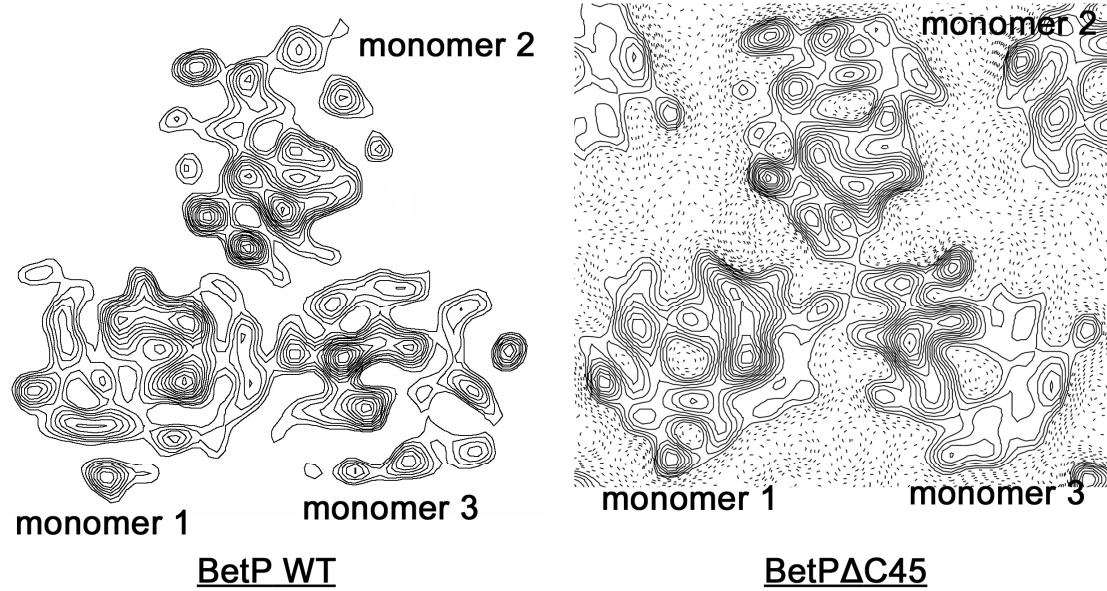


The reported 7.5 Å projection map of BetP WT grown in *E. coli* lipids and bovine cardiolipin (3:2, w/w) (Ziegler, Morbach et al. 2004).

The crystal has a packing of  $p22_12_1$  with a single unit cell of 183.0 Å × 156.2 Å. The projection map were merged from seven lattices with symmetry  $p22_12_1$  and a B factor of -200 applied.

---

**5.6. Appendix VI: Projection maps of BetP WT and BetP $\Delta$ C45**



---

## 6. References

- Abramson, J., I. Smirnova, et al. (2003). "Structure and mechanism of the lactose permease of *Escherichia coli*." *Science* **301**(5633): 610-5.
- Agard, D. A. (1983). "A least-squares method for determining structure factors in three-dimensional tilted-view reconstructions." *J Mol Biol* **167**(4): 849-52.
- Braun, T., A. Philippsen, et al. (2000). "The 3.7 Å projection map of the glycerol facilitator GlpF: a variant of the aquaporin tetramer." *EMBO Rep* **1**(2): 183-9.
- Camara-Artigas, A., D. Brune, et al. (2002). "Interactions between lipids and bacterial reaction centers determined by protein crystallography." *Proc Natl Acad Sci U S A* **99**(17): 11055-60.
- Catucci, L., N. Depalo, et al. (2004). "Neosynthesis of cardiolipin in *Rhodobacter sphaeroides* under osmotic stress." *Biochemistry* **43**(47): 15066-72.
- Chami, M., G. Pehau-Arnaudet, et al. (2001). "Use of octyl beta-thioglucopyranoside in two-dimensional crystallization of membrane proteins." *J Struct Biol* **133**(1): 64-74.
- Chintalapati, S., R. Al Kurdi, et al. (2008). "Membrane structure of CtrA3, a copper-transporting P-type-ATPase from *Aquifex aeolicus*." *J Mol Biol* **378**(3): 581-95.
- Collinson, I., C. Breyton, et al. (2001). "Projection structure and oligomeric properties of a bacterial core protein translocase." *EMBO J* **20**(10): 2462-71.
- Crowther, R. A., R. Henderson, et al. (1996). "MRC image processing programs." *J Struct Biol* **116**(1): 9-16.
- DeLano, W. L. (2002). "The PyMOL Molecular Graphics System (<http://pymol.sourceforge.net/>)."
- Dolder, M., A. Engel, et al. (1996). "The micelle to vesicle transition of lipids and detergents in the presence of a membrane protein: towards a rationale for 2D crystallization." *FEBS Lett* **382**(1-2): 203-8.
- Ejsing, C. S., E. Duchoslav, et al. (2006). "Automated identification and quantification of glycerophospholipid molecular species by multiple precursor ion scanning." *Anal Chem* **78**(17): 6202-14.
- Ekroos, K., I. V. Chernushevich, et al. (2002). "Quantitative profiling of phospholipids by multiple precursor ion scanning on a hybrid quadrupole time-of-flight mass spectrometer." *Anal Chem* **74**(5): 941-9.
- Ekroos, K., C. S. Ejsing, et al. (2003). "Charting molecular composition of phosphatidylcholines by fatty acid scanning and ion trap MS3 fragmentation." *J Lipid Res* **44**(11): 2181-92.
- Engel, A., A. Hoenger, et al. (1992). "Assembly of 2-D membrane protein crystals: dynamics, crystal order, and fidelity of structure analysis by electron microscopy." *J Struct Biol* **109**(3): 219-34.
- Farwick, M., R. M. Siewe, et al. (1995). "Glycine betaine uptake after hyperosmotic shift in *Corynebacterium glutamicum*." *J Bacteriol* **177**(16): 4690-5.
- Folch, J., M. Lees, et al. (1957). "A simple method for the isolation and purification of total lipides from animal tissues." *J Biol Chem* **226**(1): 497-509.
- Fujiyoshi, Y. (1998). "The structural study of membrane proteins by electron crystallography." *Adv Biophys* **35**: 25-80.
- Gonen, T., Y. Cheng, et al. (2004). "Aquaporin-0 membrane junctions form upon proteolytic cleavage." *J Mol Biol* **342**(4): 1337-45.
- Gonen, T., Y. Cheng, et al. (2005). "Lipid-protein interactions in double-layered two-dimensional AQP0 crystals." *Nature* **438**(7068): 633-8.
- Gruska, M., O. Medalia, et al. (2007). "Electron tomography of vitreous sections from cultured mammalian cells." *J Struct Biol*.
- Guan, L. and H. R. Kaback (2006). "Lessons from lactose permease." *Annu Rev Biophys Biomol Struct* **35**: 67-91.
- Hacksell, I., J. L. Rigaud, et al. (2002). "Projection structure at 8 Å resolution of the melibiose permease, an Na-sugar co-transporter from *Escherichia coli*." *EMBO J* **21**(14): 3569-74.
- Hasler, L., J. B. Heymann, et al. (1998). "2D crystallization of membrane proteins: rationales and examples." *J Struct Biol* **121**(2): 162-71.
- Henderson, R., J. M. Baldwin, et al. (1990). "Model for the structure of bacteriorhodopsin based on high-resolution electron cryo-microscopy." *J Mol Biol* **213**(4): 899-929.

- 
- Heymann, J. A., T. Hirai, et al. (2003). "Projection structure of the bacterial oxalate transporter OxIT at 3.4Å resolution." *J Struct Biol* **144**(3): 320-6.
- Higgins, D. G., A. J. Bleasby, et al. (1992). "CLUSTAL V: improved software for multiple sequence alignment." *Comput Appl Biosci* **8**(2): 189-91.
- Hirai, T., J. A. Heymann, et al. (2002). "Three-dimensional structure of a bacterial oxalate transporter." *Nat Struct Biol* **9**(8): 597-600.
- Hirai, T. and S. Subramaniam (2004). "Structure and transport mechanism of the bacterial oxalate transporter OxIT." *Biophys J* **87**(5): 3600-7.
- Hoischen, C. and R. Krämer (1990). "Membrane alteration is necessary but not sufficient for effective glutamate secretion in *Corynebacterium glutamicum*." *J Bacteriol* **172**(6): 3409-16.
- Huang, Y., M. J. Lemieux, et al. (2003). "Structure and mechanism of the glycerol-3-phosphate transporter from *Escherichia coli*." *Science* **301**(5633): 616-20.
- Hunte, C., E. Screpanti, et al. (2005). "Structure of a Na<sup>+</sup>/H<sup>+</sup> antiporter and insights into mechanism of action and regulation by pH." *Nature* **435**(7046): 1197-202.
- Jardetzky, O. (1966). "Simple allosteric model for membrane pumps." *Nature* **211**(5052): 969-70.
- Jones, T. A., J. Y. Zou, et al. (1991). "Improved methods for building protein models in electron density maps and the location of errors in these models." *Acta Crystallogr A* **47 ( Pt 2)**: 110-9.
- Kaback, H. R. (2005). "Structure and mechanism of the lactose permease." *C R Biol* **328**(6): 557-67.
- Khademi, S., J. O'Connell, 3rd, et al. (2004). "Mechanism of ammonia transport by Amt/MEP/Rh: structure of AmtB at 1.35 Å." *Science* **305**(5690): 1587-94.
- Kleywegt, G. J. and T. A. Jones (1999). "Software for handling macromolecular envelopes." *Acta Crystallogr D Biol Crystallogr* **55**(Pt 4): 941-4.
- Kleywegt, G. J. and R. J. Read (1997). "Not your average density." *Structure* **5**(12): 1557-69.
- Koning, R. I., W. Keegstra, et al. (1999). "The 5 Å projection structure of the transmembrane domain of the mannitol transporter enzyme II." *J Mol Biol* **287**(5): 845-51.
- Krämer, R. and S. Morbach (2004). "BetP of *Corynebacterium glutamicum*, a transporter with three different functions: betaine transport, osmosensing, and osmoregulation." *Biochim Biophys Acta* **1658**(1-2): 31-6.
- Kühlbrandt, W. (1982). "Discrimination of protein and nucleic acids by electron microscopy using contrast variation." *Ultramicroscopy* **7**(3): 221-32.
- Kühlbrandt, W. (1988). "Structure of light-harvesting chlorophyll a/b protein complex from plant photosynthetic membranes at 7 Å resolution in projection." *J Mol Biol* **202**(4): 849-64.
- Kühlbrandt, W., D. N. Wang, et al. (1994). "Atomic model of plant light-harvesting complex by electron crystallography." *Nature* **367**(6464): 614-21.
- Lucic, V., F. Forster, et al. (2005). "Structural studies by electron tomography: From cells to molecules." *Annual Review of Biochemistry* **74**: 833-865.
- Ludtke, S. J., D. H. Chen, et al. (2004). "Seeing GroEL at 6 Å resolution by single particle electron cryomicroscopy." *Structure* **12**(7): 1129-36.
- McAuley, K. E., P. K. Fyfe, et al. (1999). "Structural details of an interaction between cardiolipin and an integral membrane protein." *Proc Natl Acad Sci U S A* **96**(26): 14706-11.
- Miyazawa, A., Y. Fujiyoshi, et al. (2003). "Structure and gating mechanism of the acetylcholine receptor pore." *Nature* **423**(6943): 949-55.
- Morbach, S. and R. Krämer (2003). "Impact of transport processes in the osmotic response of *Corynebacterium glutamicum*." *J Biotechnol* **104**(1-3): 69-75.
- Morbach, S. and R. Krämer (2005). "Structure and function of the betaine uptake system BetP of *Corynebacterium glutamicum*: strategies to sense osmotic and chill stress." *J Mol Microbiol Biotechnol* **10**(2-4): 143-53.
- Morein, S., A. Andersson, et al. (1996). "Wild-type *Escherichia coli* cells regulate the membrane lipid composition in a "window" between gel and non-lamellar structures." *J Biol Chem* **271**(12): 6801-9.
- Mosser, G. (2001). "Two-dimensional crystallography of transmembrane proteins." *Micron* **32**(5): 517-40.
- Murakami, S., R. Nakashima, et al. (2006). "Crystal structures of a multidrug transporter reveal a functionally rotating mechanism." *Nature* **443**(7108): 173-9.



- 
- Nussberger, S., K. Dörr, et al. (1993). "Lipid-protein interactions in crystals of plant light-harvesting complex." *J Mol Biol* **234**(2): 347-56.
- Oling, F., J. S. Santos, et al. (2000). "Structure of membrane-bound annexin A5 trimers: a hybrid cryo-EM - X-ray crystallography study." *J Mol Biol* **304**(4): 561-73.
- Özcan, N., R. Krämer, et al. (2005). "Chill activation of compatible solute transporters in *Corynebacterium glutamicum* at the level of transport activity." *J Bacteriol* **187**(14): 4752-9.
- Pebay-Peyroula, E. and G. Brandolin (2004). "Nucleotide exchange in mitochondria: insight at a molecular level." *Curr Opin Struct Biol* **14**(4): 420-5.
- Peter, H., A. Burkovski, et al. (1996). "Isolation, characterization, and expression of the *Corynebacterium glutamicum* betP gene, encoding the transport system for the compatible solute glycine betaine." *J Bacteriol* **178**(17): 5229-34.
- Peter, H., A. Burkovski, et al. (1998). "Osmo-sensing by N- and C-terminal extensions of the glycine betaine uptake system BetP of *Corynebacterium glutamicum*." *J Biol Chem* **273**(5): 2567-74.
- Peter, H., B. Weil, et al. (1998). "*Corynebacterium glutamicum* is equipped with four secondary carriers for compatible solutes: identification, sequencing, and characterization of the proline/ectoine uptake system, ProP, and the ectoine/proline/glycine betaine carrier, EctP." *J Bacteriol* **180**(22): 6005-12.
- Phillips, G. N., Jr., J. P. Fillers, et al. (1980). "Motions of tropomyosin. Crystal as metaphor." *Biophys J* **32**(1): 485-502.
- Poolman, B., J. J. Spitzer, et al. (2004). "Bacterial osmosensing: roles of membrane structure and electrostatics in lipid-protein and protein-protein interactions." *Biochimica Et Biophysica Acta-Biomembranes* **1666**(1-2): 88-104.
- Ranson, N. A., D. K. Clare, et al. (2006). "Allosteric signaling of ATP hydrolysis in GroEL-GroES complexes." *Nat Struct Mol Biol* **13**(2): 147-52.
- Ren, G., A. Cheng, et al. (2000). "Three-dimensional fold of the human AQP1 water channel determined at 4 Å resolution by electron crystallography of two-dimensional crystals embedded in ice." *J Mol Biol* **301**(2): 369-87.
- Rimon, A., T. Tzuberly, et al. (2007). "Monomers of nhaa NA<sup>+</sup>/H<sup>+</sup> antiporter of *Escherichia coli* are fully functional yet dimers are beneficial under extreme stress conditions at alkaline pH in the presence of NA<sup>+</sup> or Li<sup>+</sup>." *J Biol Chem*.
- Rübenhagen, R., S. Morbach, et al. (2001). "The osmoreactive betaine carrier BetP from *Corynebacterium glutamicum* is a sensor for cytoplasmic K<sup>+</sup>." *EMBO J* **20**(19): 5412-20.
- Rübenhagen, R., H. Rönsch, et al. (2000). "Osmosensor and osmoregulator properties of the betaine carrier BetP from *Corynebacterium glutamicum* in proteoliposomes." *J Biol Chem* **275**(2): 735-41.
- Ruprecht, J. J., T. Mielke, et al. (2004). "Electron crystallography reveals the structure of metarhodopsin I." *EMBO J* **23**(18): 3609-20.
- Schiefner, A., J. Breed, et al. (2004). "Cation- $\pi$  interactions as determinants for binding of the compatible solutes glycine betaine and proline betaine by the periplasmic ligand-binding protein ProX from *Escherichia coli*." *J Biol Chem* **279**(7): 5588-96.
- Schiller, D., R. Rübenhagen, et al. (2004). "The C-terminal domain of the betaine carrier BetP of *Corynebacterium glutamicum* is directly involved in sensing K<sup>+</sup> as an osmotic stimulus." *Biochemistry* **43**(19): 5583-91.
- Schmidt-Krey, I., W. Haase, et al. (2007). "Two-dimensional crystallization of human vitamin K-dependent gamma-glutamyl carboxylase." *J Struct Biol* **157**(2): 437-42.
- Schmidt-Krey, I., G. Lundqvist, et al. (1998). "Parameters for the two-dimensional crystallization of the membrane protein microsomal glutathione transferase." *J Struct Biol* **123**(2): 87-96.
- Schmidt-Krey, I., K. Murata, et al. (1999). "The projection structure of the membrane protein microsomal glutathione transferase at 3 Å resolution as determined from two-dimensional hexagonal crystals." *J Mol Biol* **288**(2): 243-53.
- Seeger, M. A., A. Schiefner, et al. (2006). "Structural asymmetry of AcrB trimer suggests a peristaltic pump mechanism." *Science* **313**(5791): 1295-8.
- Shimoni, E., O. Rav-Hon, et al. (2005). "Three-dimensional organization of higher-plant chloroplast thylakoid membranes revealed by electron tomography." *Plant Cell* **17**(9): 2580-6.
- Shinzawa-Itoh, K., H. Aoyama, et al. (2007). "Structures and physiological roles of 13 integral

- 
- lipids of bovine heart cytochrome c oxidase." *EMBO J* **26**(6): 1713-25.
- Signorell, G. A., T. C. Kaufmann, et al. (2007). "Controlled 2D crystallization of membrane proteins using methyl-beta-cyclodextrin." *J Struct Biol* **157**(2): 321-8.
- Singh, S. K., A. Yamashita, et al. (2007). "Antidepressant binding site in a bacterial homologue of neurotransmitter transporters." *Nature* **448**(7156): 952-6.
- Smith, J. M. (1999). "Ximdisp--A visualization tool to aid structure determination from electron microscope images." *J Struct Biol* **125**(2-3): 223-8.
- Stahlberg, H., D. Fotiadis, et al. (2001). "Two-dimensional crystals: a powerful approach to assess structure, function and dynamics of membrane proteins." *FEBS Lett* **504**(3): 166-72.
- Standfuss, J., A. C. Terwisscha van Scheltinga, et al. (2005). "Mechanisms of photoprotection and nonphotochemical quenching in pea light-harvesting complex at 2.5 Å resolution." *EMBO J* **24**(5): 919-28.
- Steger, R., M. Weinand, et al. (2004). "LcoP, an osmoregulated betaine/ectoine uptake system from *Corynebacterium glutamicum*." *FEBS Lett* **573**(1-3): 155-60.
- Subramaniam, S. and R. Henderson (2000). "Molecular mechanism of vectorial proton translocation by bacteriorhodopsin." *Nature* **406**(6796): 653-7.
- Sukharev, S., M. Betanzos, et al. (2001). "The gating mechanism of the large mechanosensitive channel MscL." *Nature* **409**(6821): 720-4.
- Sun, M. G., J. Williams, et al. (2007). "Correlated three-dimensional light and electron microscopy reveals transformation of mitochondria during apoptosis." *Nat Cell Biol* **9**(9): 1057-65.
- Tate, C. G., E. R. Kunji, et al. (2001). "The projection structure of EmrE, a proton-linked multidrug transporter from *Escherichia coli*, at 7 Å resolution." *EMBO J* **20**(1-2): 77-81.
- Ubarretxena-Belandia, I., J. M. Baldwin, et al. (2003). "Three-dimensional structure of the bacterial multidrug transporter EmrE shows it is an asymmetric homodimer." *EMBO J* **22**(23): 6175-81.
- Unwin, N. (2005). "Refined structure of the nicotinic acetylcholine receptor at 4Å resolution." *J Mol Biol* **346**(4): 967-89.
- Unwin, N., A. Miyazawa, et al. (2002). "Activation of the nicotinic acetylcholine receptor involves a switch in conformation of the alpha subunits." *J Mol Biol* **319**(5): 1165-76.
- Valpuesta, J. M., J. L. Carrascosa, et al. (1994). "Analysis of electron microscope images and electron diffraction patterns of thin crystals of phi 29 connectors in ice." *J Mol Biol* **240**(4): 281-7.
- Vinothkumar, K. R., S. Raunser, et al. (2006). "Oligomeric structure of the carnitine transporter CaiT from *Escherichia coli*." *J Biol Chem* **281**(8): 4795-801.
- Vinothkumar, K. R., S. H. Smits, et al. (2005). "pH-induced structural change in a sodium/proton antiporter from *Methanococcus jannaschii*." *EMBO J* **24**(15): 2720-9.
- Vonck, J., T. K. von Nidda, et al. (2002). "Molecular architecture of the undecameric rotor of a bacterial Na<sup>+</sup>-ATP synthase." *J Mol Biol* **321**(2): 307-16.
- Wang, D. N. and W. Kühlbrandt (1991). "High-resolution electron crystallography of light-harvesting chlorophyll a/b-protein complex in three different media." *J Mol Biol* **217**(4): 691-9.
- Williams, K. A., U. Geldmacher-Kaufer, et al. (1999). "Projection structure of NhaA, a secondary transporter from *Escherichia coli*, at 4.0 Å resolution." *EMBO J* **18**(13): 3558-63.
- Wolf, A., R. Krämer, et al. (2003). "Three pathways for trehalose metabolism in *Corynebacterium glutamicum* ATCC13032 and their significance in response to osmotic stress." *Mol Microbiol* **49**(4): 1119-34.
- Yamashita, A., S. K. Singh, et al. (2005). "Crystal structure of a bacterial homologue of Na<sup>+</sup>/Cl<sup>-</sup>-dependent neurotransmitter transporters." *Nature* **437**(7056): 215-23.
- Yernool, D., O. Boudker, et al. (2004). "Structure of a glutamate transporter homologue from *Pyrococcus horikoshii*." *Nature* **431**(7010): 811-8.
- Yu, E. W., G. McDermott, et al. (2003). "Structural basis of multiple drug-binding capacity of the AcrB multidrug efflux pump." *Science* **300**(5621): 976-80.
- Zhuang, J., G. G. Prive, et al. (1999). "Two-dimensional crystallization of *Escherichia coli* lactose permease." *J Struct Biol* **125**(1): 63-75.
- Ziegler, C., S. Morbach, et al. (2004). "Projection structure and oligomeric state of the osmoregulated sodium/glycine betaine symporter BetP of *Corynebacterium glutamicum*." *J Mol Biol* **337**(5): 1137-47.
-



---

## 7. Acknowledgement

What a great time I've spent in Frankfurt! I would like to thank those whom I have shared these amazing four years with. Without them, I wonder if I could have fulfilled my dream of a PhD in Germany with such a great joy.

I would like to thank Dr. Christine Ziegler for the opportunity of joining her laboratory. I am especially proud of being her first PhD student, and appreciate the freedom for exploring research, as well as her warmth and concern in both scientific career and private life.

Many thanks to Prof. Werner Kühlbrandt for giving me this great opportunity of doing my PhD in his department. He has created a harmonic and stimulating research environment, which leads to many vivid discussions about many different aspects, and I have learned a lot from this. His personal enthusiasm and passion in science also inspired me a great deal.

Frau Ulrike Geldmacher-Kaufer for her management of the Ziegler laboratory. I especially want to thank her for her kind guidance which allowed me to smoothly adapt to my new life in Frankfurt.

I felt very lucky to have a chance to work with Dr. Janet Vonck and Prof. Ingeborg Schmidt-Krey. Janet and Inga are excellent electron microscopists and I appreciated their help and detailed instruction in 2D crystallization, EM sample preparation, data collection and processing. To me, they also represent an outstanding example of successful female scientist. Apart from their scientific excellence, I also appreciate their sharing of many other aspects in life.

Mr. Deryck Mills for his wonderful organization of the electron microscopes and the accessory facilities. His excellent maintenance and help have accelerated my work, and helped forming my view of an ideal EM lab. Beside his scientific help, I want to thank him for the great time we have had in the EM dungeon.

---

Many thanks to Dr. Anke Terwisscha van Scheltinga. She is a very experienced X-ray crystallographer and helped me a great deal in 3D map reconstruction, data processing, and protein model building. I have enjoyed working together with her very much. Like Janet and Inga, Anke also inspires me very much with her constant motivation in science and life.

Mr. Remco Wouts and Dr. Özkan Yildiz for their professional support and instruction in software and computer processing.

Dr. Winfried Haase and Frau Friederike Joos for the help in freeze-fracture and thin-section microscopy.

Prof. Reinhard Krämer, Dr. Susanne Morbach and Dr. Nuran Özcan from Universität zu Köln for the discussion about the project from the viewpoint of a biochemist and a microbiologist.

Dr. Christer S. Ejsing and Dr. Andrej Shevchenko from Max-Planck Institute of Cell Biology and Genetics in Dresden for their collaboration and the lipid analysis.

Prof. Bernd Ludwig for his roll of being my official tutor in the Frankfurt Universität.

Deutsche Forschungsgesellschaft (DFG) and International Max-Planck Research School for the financial support.

Special thanks to Dr. Jörg Standfuss for his unconditioned support in both the scientific field and private life.

Many many thanks and hugs to all former and current colleagues in the Ziegler lab: Ulrike Geldmacher-Kaufer, Sonja Kuhlmann, Susanna Ressler, Jonna Hakulinen, Sabrina Schulz, Bertram Daum, Nico Riffel, and of course the Chefin Christine Ziegler. Their help, support and warmth have lightened my PhD life from the beginning on.

---

In the end, I would like to thank to all the members from MPIBP. I am happy and lucky to know these amazing people and share part of my life with.



---

## 8. Curriculum Vitae

蔡馨如 Ching-Ju Tsai

Born January 26<sup>th</sup> 1978 in Taipei, Taiwan



### EDUCATION

- |             |  |
|-------------|--|
| 2002 – 2007 | Ph. D. Biochemistry<br>Department of Structural Biology<br>Max-Planck Institute of Biophysics (Frankfurt, Germany)<br>International Max-Planck Research School |
| 2000 – 2002 | MS Science<br>Department of Life Science<br>National Tsing Hua University, Hsinchu, Taiwan   |
| 1996 – 2000 | BA Science<br>Department of Chemistry<br>National Tsing Hua University, Hsinchu, Taiwan  |
| 1993 – 1996 | Taipei First Girls' Senior High School, Taipei   |
| 1989 – 1993 | Ger-Jyh High School, Taipei  |
| 1983 – 1989 | Yan-Ping Elementary School, Taipei, Taiwan   |

### THESES

- |              |  |
|--------------|--|
| Dissertation | Three-dimensional structure of the glycine-betaine transporter BetP by cryo electron crystallography |
| Master       | Crystal structure of cytotoxic RC-RNase and d(ApCpGpA) complex: discovery of a new binding site      |



---

## PUBLICATIONS

### **C.-J. Tsai, C. S. Ejsing, A. Shevchenko & C. Ziegler**

The role of lipids and salts in two-dimensional crystallization of the glycine-betaine transporter BetP from *Corynebacterium glutamicum*.

Journal of Structural Biology 2007; 160: 275-286

### **C.-J. Tsai, W. Kühlbrandt, R. Krämer & C. Ziegler**

Three-dimensional structure of the glycine-betaine transporter BetP from *Corynebacterium glutamicum*. (In preparation)

### **N. P. Mazurova, C.-J. Tsai, C. Ziegler, A. Kedrov & D. J. Müller**

Mapping molecular interactions driving functional states of the osmosensing and osmoregulating betaine transporter BetP of *Corynebacterium glutamicum*. (in preparation)

### **C.-J. Tsai & C. Ziegler**

Structure determination of secondary transport proteins by electron crystallography: two-dimensional crystallization of the betaine uptake system BetP.

J Mol Microbiol Biotechnol 2005; 10: 197-207

### **C.-J. Tsai, J.-H. Liu, Y.-D. Liao, L.-Y. Chen, P.-T. Cheng & Y.-J. Sun**

Novel and retro binding modes in cytotoxic ribonucleases from *Rana catesbeiana* of two crystal structures complexed with d(ApCpGpA) and (2', 5' CpG).

Protein data bank: 1oj1 & 1oj8 (2004)

## Attended Conferences and Courses

- 2006 Gordon Research Conference: Three Dimensional Electron Microscopy, Il Ciocco, Italy; poster presentation
- 2006 Max-Planck Research School: EM course, Frankfurt, Germany; lecturer
- 2004 EMBO practical Course: Cryo-EM and digital image analysis, Heidelberg, Germany; selected student
- 2003 Deutsche Forschungsgesellschaft: internal meeting, Freiburg, Germany; invited speaker